

POLITECNICO DI MILANO

FACOLTÀ DI INGEGNERIA DELL'INFORMAZIONE

Corso di Laurea Specialistica in Ingegneria Elettronica

**A MODULAR INSTRUMENT BASED ON
CROSS-CORRELATION TECHNIQUE FOR NOISE
MEASUREMENTS**



Relatore: Giorgio Ferrari

Correlatore: Marco Sampietro

Tesi di Laurea di:

Paolo Manicardi

Matr. 748720

Anno Accademico 2012-2013

*Can a
man-made
Universe
be achieved by
quantum tunneling
without an initial
singularity?*

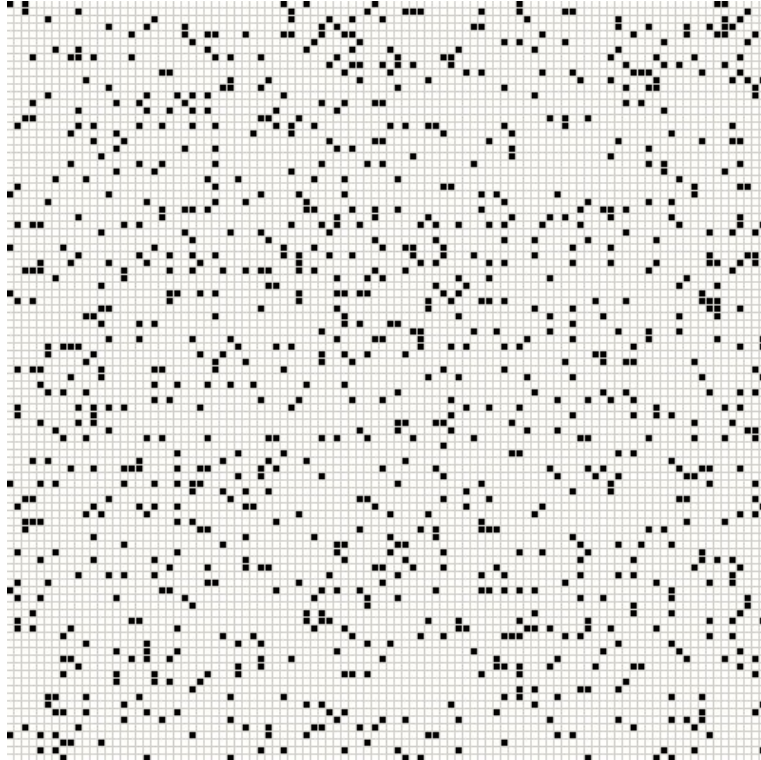


Figure 1: TO BE DEFINED

Contents

Introduzione	II
Introduction	IV
List of figures	VI
List of tables	X
1 Principles of operation	3
1.1 Cross-correlation technique	4
1.2 Limits in noise measurements	6
1.2.1 Measurement time	6
1.2.2 Instrument's sensitivity	7
1.3 Not-identical channels	8
1.4 Current mode front-end	9
1.5 Voltage-mode front-end	12
1.6 Current versus voltage measurement	14
2 Instrument overview	15
2.1 Physical design and layout	17
2.2 Graphical User Interface	18
3 Design of the mainboard	21
3.1 Mainboard function and capabilities	21
3.2 Channel Amplifier	22
3.2.1 High pass filter and first gain stage	23
3.2.2 Programmable Gain Amplifier, Output Stage	24
3.2.3 Integrator feedback loop	25
3.2.4 Anti aliasing filter	26
3.3 Noise generator	28
3.4 Power Supply	31
3.5 Physical design and layout	32
4 Current sensitive front-end	33
4.0.1 Design of the front-end stage	34
4.0.2 Drain and source bias network	37
4.0.3 Gate bias network	39
4.1 Physical design and layout	46

5	Front-end for Magnetic Tunnel Junction devices	47
5.1	Tunneling magnetoresistance theory	47
5.1.1	Tunnelling through a barrier	47
5.1.2	Sensor layout and characteristics	51
5.2	MTJ noise sources	52
5.3	Design of the voltage-mode front-end	53
5.4	Physical design and layout	54
5.5	Front-end validation	56
5.6	MTJ characterization and noise measurement	57
5.6.1	Measures on $1\text{k}\Omega$ MTJ devices	58
5.6.2	Measures on $10\text{k}\Omega$ MTJ devices	64
5.6.3	Measures on 100Ω MTJ devices	65
6	Low-frequency noise in P3HT fibers O-Fet	67
6.1	Structure of Ofet based on P3HT nanofibers	68
6.2	Integrator-Differentiator cascade amplifier	70
6.3	Design of the front-end for Ofet devices	72
6.4	Ofet with P3HT active fibers above contact pads	75
6.5	Ofet with P3HT active fibers and free contact pads	84
	Conclusioni	89
	Conclusion	90
	Bibliography	92
	Ringraziamenti	95

Introduzione

La sensibilità dei tradizionali analizzatori di spettro a singolo canale è tipicamente limitata dal rumore elettronico dello stadio di ingresso. Per superare questo limite è possibile utilizzare strumenti multicanale basati sulla tecnica della cross correlazione, già realizzati e disponibili nel laboratorio del professor Marco Sampietro, in grado di attenuare il rumore incorrelato dei singoli canali ed aumentare quindi la sensibilità dello strumento.

Durante questo lavoro di tesi è stata realizzata una nuova versione modulare dell'analizzatore di spettro a cross-correlazione, in grado di potersi adattare con facilità ai differenti dispositivi per i quali vi è interesse ad avere la misura del rumore elettronico. A differenza dei precedenti esemplari il controllo dello strumento, la generazione delle tensioni di polarizzazione e l'elaborazione dei segnali sono ora interamente effettuati mediante un unico software installabile su pc: questo aumenta la velocità di realizzazione delle misure e la loro ripetibilità, rendendo quindi in generale più semplice ed intuitivo l'uso.

Contemporaneamente alla progettazione e realizzazione si sono manifestate varie opportunità di uso per lo strumento; sono stati sviluppati quindi degli stadi di ingresso dedicati alla caratterizzazione di dispositivi elettronici avanzati in fase di sviluppo presso altri laboratori universitari in contatto con il laboratorio del professor Sampietro.

Nel **Capitolo 1** è illustrata teoricamente la tecnica della cross-correlazione che sta alla base del funzionamento dello strumento, come è stata implementata e le prestazioni che permette di ottenere in funzione della topologia dello stadio di ingresso.

Il **Capitolo 2** fornisce una visione di insieme dello strumento, evidenziando i vantaggi della struttura modulare. Viene inoltre descritto il software di controllo ed elaborazione.

La scheda principale dello strumento, responsabile del suo controllo ed interfacciamento agli stadi di ingresso, è descritta in dettaglio nel **Capitolo 3**.

Nel **Capitolo 4** è descritta la riprogettazione di uno stadio di ingresso per misure a larga banda del rumore di corrente di dispositivi mosfet sia integrati che discreti. Questa topologia circuitale, già presente in precedenti versioni dello strumento, è stata migliorata integrando nuove funzionalità che hanno permesso di aumentarne le prestazioni e flessibilità d'uso.

I **capitoli 5 e 6** sono rispettivamente dedicati a due tipologie di dispositivi: mosfet basati su materiali organici (Ofet) e sensori magnetici ad effetto tunnel (MTJ) caratterizzati alla fine del lavoro di tesi. Per entrambi è presente una breve descrizione della fisica del dispositivo che ha influenzato la progettazione degli specifici stadi di ingresso, seguita dalla presentazione e interpretazione delle misure sperimentali ottenute.

Introduction

The sensibility of a traditional single channel spectrum analyser is limited by electronic noise of the first stage. To overcome this limitation is possible to use a multichannel instrument based on the cross-correlation technique: these types of instruments, already made and available in the laboratory of DEI professor Marco Sampietro, are able to attenuate the uncorrelated noise of the channels and consequently improve the overall sensibility.

This thesis work is focused on the design and realization of a new modular version of the cross-correlation spectrum analyser, easily adaptable to many different devices for which is useful a noise characterization. Unlike previous instrument with manual control, the command to the instrument, generation of bias voltages and signal elaboration are now all managed by single pc software with graphical interface: this feature speed up the work and improve the measurements repeatability, making the spectrum analyser more intuitive and easy to use.

Simultaneously with the design and implementation, have arisen opportunities to use the instrument on advanced electronic devices in development at others various university laboratories in collaboration whit the lab of Marco Sampietro.

Chapter 1 describe the cross-correlation technique: how it has been implemented in the instrument and its performance, depending on the front-end topology.

The **Chapter 2** is an overview of the entire instrument, highlighting the advantages of a modular structure. It also describes the control and processing software.

The instrument's mainboard, which constitutes the core of the instrument, is described in detail in **Chapter 3**

Chapter 4 describe the re-design of a front-end stage suitable for wide bandwidth measure of noise current generated by integrated or discrete mosfet devices. This type of front-end, already present in a number of past implementations, has been improved with new features and bug corrections, in order to increase its performance and versatility.

Chapters 5 and 6 are respectively dedicated to two different electronic devices: mosfet made with organic polymers (Ofet) and sensors based on magnetic tunnel junction effect (MTJ) which have been characterized at the end of the thesis work. There is a brief introduction to the device physics that motivates the front-end design, followed by the presentation and interpretation of experimental results.

List of Figures

1	TO BE DEFINED	2
1.1	Working principle of a cross-correlation spectrum analyser	4
1.2	Output due to the instrumental noise: left with correlated noise, right with uncorrelated noise	7
1.3	Generic transimpedance front-end	9
1.4	Voltage mode front-end: all possible noise sources are indicated	12
2.1	Overview of the instrument components and connections	16
2.2	The instrument viewed from top side without cover lid. The mainboard is the board on the right	18
2.3	Main window of the instrument's control software	19
2.4	Signals acquisition control box: RBW[Hz] and Time[S] are read only fields, their value are calculated from nrecord, block and sampling rate entered values.	20
2.5	Visualization window for the acquired file. Axis limits are automatically sets by an autoscale algorithm, but can be manual entered by the end user	20
3.1	Block scheme of the mainboard subsections and their interconnections	21
3.2	Diagram of operation of the acquisition channel amplifier on the mainboard	22
3.3	AC Coupling and first amplifier stage	23
3.4	Simulation of first amplifier stage and ac coupling transfer functions, for each selectable R_{in}	24
3.5	Programmable Gain Amplifier, output stage and integrator feedback loop	25
3.6	Low Pass filter stage: the two operational amplifiers and biquadratic cells low pass filters are integrated on the same device	27
3.7	Noise generator circuits overview	28
3.8	White Noise Generator block diagram.	29
3.9	White Noise Generator complete circuit	29
3.10	1/f noise generator: the nnmos device is not soldered on the board, but there is a socket where a discrete device can be inserted. The trimmer that select the V_{gain} is digitally controlled by the control software	30
3.11	Independently gain stages for white noise and 1/f noise	30
3.12	Programmable gain amplifier, high pass filter and output stage of the noise generator. The relay give the opportunity to connect an external generator	31
3.13	Image of the populated mainboard with highlighted main function blocks and connections	32
4.1	Basic transimpedance gain stage	34
4.2	Designed transimpedance stage with complete feedback network	35
4.3	Feedback network at high(sx) and low(dx) frequencies	36

4.4	Transimpedance amplifier with bias circuitry	37
4.5	Complete current-sensitive front-end circuit	39
4.6	Current-sensitive front-end: cross-correlation configuration	40
4.7	Current-sensitive front-end: wrong Vgs bias circuit	41
4.8	Current-sensitive front-end: correct Vgs bias circuit	42
4.9	Current-sensitive front-end configured for DUT's g_m measure by injecting input signal at the gate terminal	43
4.10	Current-sensitive front-end configured for DUT's g_m measure by injecting input signal at the source terminal	44
4.11	Current-sensitive front-end: configured for DUT's R_0 measure	45
4.12	Current-sensitive front-end: realized front-end board viewed from the top side	46
5.1	Tunneling through a barrier: reflected and transmitted wavefunctions	48
5.2	Bias dependence of the TMR ratio (a) and of the conductance for parallel (b) and anti-parallel (c) configurations in a CoFeB/AlO _x /CoFeB junction at $T = 5^\circ K$ and $T = 300^\circ K$	50
5.3	(a) The quantity ΔG and TMR as a function of temperature. (b) Temperature dependence of the P and AP conductance at a bias of 2mV. Same CoFeB/AlO _x /CoFeB junction as in figure 5.2	51
5.4	Transversal structure of a MTJ device	51
5.5	Complete front-end circuit for MTJ noise measure	53
5.6	Close up of MTJ chip carrier inserted in to the front-end board	55
5.7	Front-end board for MTJ noise measurement viewed from the top side	55
5.8	Noise of 160 Ω resistor at three different bias voltage; high frequency measure without low pass filter	56
5.9	Noise of 390 Ω resistor with no bias and low pass filter activated; effect of external electromagnetic noise sources	56
5.10	Magnetic Tunnel Junctions, array of devices on single die	57
5.11	Magnetic Tunnel Junctions, array of devices on single die, photograph by optical microscope	57
5.12	1k Ω MTJ, I-V characteristics, 2mA current limit	58
5.13	1k Ω MTJ: constant voltage resistance	58
5.14	Voltage Noise Density of MTJ γ ; dotted black line is the white thermal noise expected at $0\mu A$	59
5.15	MTJ γ , noise sampled at 10kHz at different bias currents	60
5.16	Measured noise of a 1k Ω resistor with and without 100pF parallel capacitor; dotted blue line is the expected white thermal noise	61
5.17	Measured noise of the artificial DUT made by 1k Ω resistor and 100pF parallel capacitor, at same bias currents of figure 5.14; dotted line is the expected white thermal noise	61
5.18	MTJ γ , measured voltage noise density. Each curve is an union of a measure at low frequency and another one at high frequency	62
5.19	MTJ γ , voltage noise density sampled at various frequencies, against bias current	62
5.20	MTJ α , measured voltage noise density. Each curve is an union of a measure at low frequency and another one at high frequency	63
5.21	MTJ α , voltage noise density sampled at various frequencies, against bias current	63
5.22	10k Ω MTJ device; measure noise spectral density	64
5.23	10k Ω MTJ device noise against bias current	64

5.24	R-H plot for a typical MTJ device: maximum sensibility (red line) correspond to a non-zero applied magnetic field	65
5.25	100 Ω MTJ device C2-1, measured noise whit and without applied magnetic field	65
5.26	100 Ω MTJ device C2-2, measured noise whit and without applied magnetic field	66
5.27	100 Ω MTJ device C2-5, measured noise whit and without applied magnetic field	66
6.1	Ofet based on P3HT nanofibers imaged by an optical microscope: buried electrode contacts are clearly visible under the active nanofibers layer with scratches caused by contact probe tips.	69
6.2	Output characteristics of OFETs based on polymer nanofibers (a) and thin films (b). Channel length $L = 12 \mu\text{m}$ for both structures. (c, d) Are the corresponding transfer characteristics $I_{DS}(V_{GS})$ (left vertical scale) and $ I_{DS} ^{1/2}(V_{GS})$ (right vertical scale) for a fixed $V_{DS} = -50V$ Continuous lines are linear fits of data.	69
6.3	Single stage transimpedance amplifier	70
6.4	Ideal integrator - differentiator cascade transimpedance amplifier	71
6.5	Complete structure of integrator-differentiator amplifier used in each channel of the realized front-end	71
6.6	Complete circuit of the front-end for OFet devices noise measure	74
6.7	Optical microscope photograph of the Ofet with P3HT active fibers above contact pads	75
6.8	Ofet device contacted with the probe station at $V_G = 0V$: measured channel noise current	76
6.9	Ofet device contacted with the probe station at $V_G = 0V$: measured source current against source-drain bias voltage	77
6.10	Ofet device contacted with the probe station at $V_G = 0V$: noise evaluated at 90Hz (black dots) and the interpolation line (red dots)	77
6.11	Ofet device contacted with the probe station at $V_G = -25V$: measured channel noise current for increasing bias voltage from 0V to -50V	78
6.12	Ofet device contacted with the probe station at $V_G = -25V$: measured channel noise current for decreasing bias voltage from -50V to 0V	79
6.13	Ofet device contacted with the probe station at $V_G = -25V$: measured source current against source-drain bias voltage	79
6.14	Ofet device contacted with the probe station at $V_G = -25V$: noise evaluated at 90Hz (black dots) and the interpolation line (red dots)	80
6.15	Ofet device contacted with bonding wires at $V_G = 0V$: measured channel noise current for increasing bias voltage from 0V to -50V	81
6.16	Ofet device contacted with bonding wires at $V_G = 0V$: measured channel noise current for decreasing bias voltage from -50V to 0V	82
6.17	Current Noise density of a 100M Ω resistor: measured and theoretical value . .	82
6.18	Ofet device contacted with the bonding wires: measured bias current is plotted against the applied bias voltage	83
6.19	Ofet device contacted with the bonding wires at $V_G = 0V$: measured source current against source-drain bias voltage	83
6.20	Current noise spectral density measured in a fiber FET with a channel length of 6 μm . Gate-source voltage is fixed at 0V and the drain-source voltage is ranged from 0V to -15V.	84

6.21	Current noise spectral density measured in a fiber FET with a channel length of $6\mu\text{m}$. Gate-source voltage is fixed at 40V and the drain-source voltage is ranged from 0V to -15V.	85
6.22	Current noise sampled at 1kHz plotted against bias current. Solid red line is the interpolating function	85
6.23	Device output characteristic obtained by a Keithley Semiconductor parameter Analyzer in comparison to the same measure obtained by the spectrum analyser during current noise measures	86
6.24	Noise measure of thin-film Ofet: graph in the lower right corner is the normalized noise level at 1kHz.	87
6.25	Normalized noise level at 1kHz for a set of nanofibers Ofet devices with different channel lengths. The dashed line indicates the slope of $V_{sd} \cdot I_d$ predicted by the Hooge formula	88
6.26	Calculated Hooge constant α_H for Ofet devices based on nanometric fibers and thin-film active layer	88

List of Tables

3.1	Correspondences between PGA selected gain and integrator feedback loop resistor	26
4.1	Most significant parameters of THS4021 operational amplifier.	35
4.2	Loop gain poles and zeros.	36
5.1	MTJ γ , resistance at different measured bias current	59
6.1	Integrator G_{LOOP} poles and zeros	72
6.2	Differentiator G_{LOOP} poles and zeros	73

Chapter 1

Principles of operation

In a traditional single channel measuring set-up the noise of the first amplification stage is the lower absolute limit of sensitivity: as the input signal decreases in value it is gradually less distinguishable from the noise. Conventionally the threshold value is when the useful signal and the noise have the same value, typically indicated by the expression $SNR = 1$. It is obvious that it is always preferable to have lowest possible noise to increase the SNR ratio, and therefore obtain more precise measures of the input signal. Some measurement set-up can reduce the unwanted instrumental noise, but they are not always possible or feasible to implement, for example active cooling of the amplifiers at cryogenic temperatures. When the noise to be measured is stationary, the cross-correlation technique has proven to be effective to overcome the limitations imposed by the electronic noise of the instrument amplifier and to extend the sensitivity of noise measurements even below the threshold value of $SNR=1$. An instrument using this technique, which we call a correlation spectrum analyser, is based on the processing of signals from two independent channels operated in parallel and takes advantage of the uncorrelated properties of the noises of the two input stages.

1.1 Cross-correlation technique

The cross-correlation technique consists of performing at the same time two different measure of the same signal by two identical and independent acquisition channels; on both of them will be present the useful signal and the unwanted noise inevitably introduced by the channel itself. Because the noise in one channel is uncorrelated whit the noise in the other one, performing the mathematical cross-correlation operation on the two channels returns only the useful signal and reduces (ideally eliminates with an infinite measurement time) the uncorrelated noise. [1][4][5][6]

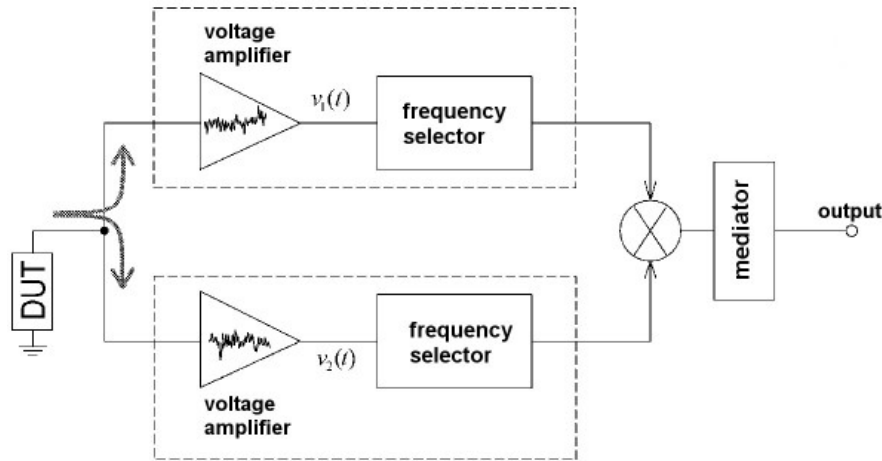


Figure 1.1: Working principle of a cross-correlation spectrum analyser

In the basic scheme of figure 1.1 each channel consists of a low-noise pre-amplifier and a band-pass filter that selects the frequency of interest for measure. In a digital spectrum analyser the frequency selector is made by an ADC converter followed by a Discrete Fourier Transform (DFT) operation which work as a bank of narrowband filters and allows to measure over N frequencies in parallel (where N is the number of acquired samples). Referring to figure 1.1 is possible to express the signals on two channels in this form:

$$\begin{aligned} v_1(n) &= s(n) + w_1(n) \\ v_2(n) &= s(n) + w_2(n) \end{aligned} \quad (1.1)$$

where

- $s(n)$ is the signal from the DUT (common to both channels)
- $w_1(n)$ and $w_2(n)$ are the noise of first and second channels

The power spectral density of $s(n)$, S_s , is (by definition) the Fourier transform of the auto-correlation function, $r_s(\tau)$:

$$S_s(f) = \mathcal{F} \{r_s(\tau)\} = \sum_{\tau=-\infty}^{+\infty} r_s(\tau) e^{-j2\pi f\tau} \quad (1.2)$$

Since the two noises is uncorrelated between them and between the signal, is possible to express the cross-correlation of two channels $v_1(n)$ and $v_2(n)$ as:

$$\begin{aligned}
r_{v_1v_2}(\tau) &= \mathbf{E}[v_2(n)v_1(n+\tau)] \\
&= \mathbf{E}[(s(n) + w_2(n))(s(n+\tau) + w_1(n+\tau))] \\
&= r_s(\tau) + m_s(m_{w_1} + m_{w_2}) + m_{w_1}m_{w_2}
\end{aligned} \tag{1.3}$$

where m_s , m_{w_1} e m_{w_2} are the mean value of, respectively, $s(n)$, $w_1(n)$ e $w_2(n)$. Calculating the Fourier transform of the cross-correlation is obtained:

$$\mathcal{F}\{r_{v_1v_2}(\tau)\} = \mathcal{F}\{r_s(\tau)\} + [m_s(m_{w_1} + m_{w_2}) + m_{w_1}m_{w_2}] \cdot \delta(f) \tag{1.4}$$

that shows how to derive the spectrum of useful signal only (at non-zero frequency) ideally eliminating the contribution of the noise introduced by the two channels of the instrument. However the cross-correlation operation can reach this result only by acting on an infinite number of samples. In the real case with only N samples we can have an estimate of the cross-correlation function given by:

$$\tilde{r}_{v_1v_2}(\tau) = \frac{1}{N} \sum_{n=0}^{N-1} v_2(n)v_1(n+\tau) \tag{1.5}$$

correspondingly, an estimation of the power spectral density is

$$\begin{aligned}
\tilde{S}_s(f) &= F\{\tilde{r}_{v_1v_2}(\tau)\} = \sum_{\tau=-N+1}^{N-1} \tilde{r}_{v_1v_2}(\tau)e^{-j2\pi f\tau} \\
&= \frac{1}{N} \sum_{\tau=-N+1}^{N-1} \sum_{n=0}^{N-1} v_2(n)v_1(n+\tau)e^{-j2\pi f\tau} \\
&= \frac{1}{N} \sum_{n=0}^{N-1} v_2(n)V_1(f)e^{j2\pi fn} = \frac{1}{N} V_1(f)V_2^*(f)
\end{aligned} \tag{1.6}$$

The Fourier transform $V_1(f)$ e $V_2(f)$ are calculated from a finite number of samples, so they can be replaced by the corresponding DFT. The result is the estimate of the spectrum of useful signal in a implementable form:

$$\tilde{S}_s(f_k) = \frac{1}{N} V_1(f_k)V_2^*(f_k) \tag{1.7}$$

where $f_k = k/N$ is the discrete frequency of the DFT. The estimate provided by the equation 1.7 uses the N available samples to obtain the best frequency resolution. To reduce the contributions given by the uncorrelated noise it's necessary to repeat this procedure on N_b different block of samples. Then an average frequency by frequency is performed to reduce the effect of the zero mean value fluctuations given by the uncorrelated terms. In the equation 1.6 we see that the estimate \tilde{S}_s is generally a complex value while S_s is a real one. An improved estimation of the power spectral density is therefore given by

$$\begin{aligned}
\tilde{S}_s(f_k) &= \frac{1}{N} \Re\{V_1(f_k)V_2^*(f_k)\} = \\
&= \frac{1}{N} \Re\{|V_1(f_k)||V_2(f_k)|e^{j\phi_1(f_k)-\phi_2(f_k)}\} = \\
&= \frac{1}{N} |V_1(f_k)||V_2(f_k)| \cos(\phi_1(f_k) - \phi_2(f_k))
\end{aligned} \tag{1.8}$$

where $\phi_1(f_k)$ and $\phi_2(f_k)$ are the phase of the DFT at the frequency f_k . The equation 1.8 can be interpreted as the scalar product of the phasors associated with the signals in the two channels of the instrument. So the operation of cross-correlation enables not only to reduce (ideally cancel) the noise present in the two independent channels, but also to completely eliminate the signals in both channels out of phase with each other by $\pm 90^\circ$.

1.2 Limits in noise measurements

As described in the previous paragraph, the cross-correlation spectrum analyser, reducing the uncorrelated noise, can detect a signal of amplitude below the noise of individual channels. The sensitivity of the instrument is limited by two factors:

- finite measurement time that imposes a residual random fluctuation due to residual uncorrelated noise;
- correlation of the instrumental noise, an effect that can not be eliminated by cross-correlation and constitutes the ultimate limit for sensitivity.

1.2.1 Measurement time

Performing the average over a finite time (ie on a finite number N_b of blocks) causes that the uncorrelated noise can not be completely eliminated, making the measure suffers from some degree of uncertainty. To properly set a session of measurement is therefore important quantify this uncertainty in terms of:

- total measurement time
- desired frequency resolution
- amount of uncorrelated noise
- amount of useful signal from the DUT

Since each block used to calculate the DFT is composed by N samples and there are N_b blocks, the total measurement time T_m needed to acquire all the samples is:

$$T_m = N_b N T_c = N_b \frac{1}{RBW} \quad (1.9)$$

Where T_c is the sampling time and RBW the frequency resolution of the measured power spectral density [8]. By indicating with S_{w1} and S_{w2} the uncorrelated noise of individual channels, it can be shown [1] that the standard deviation $\sigma_{\tilde{S}}$ of the measured power spectral density is a function of T_m :

$$\sigma_{\tilde{S}} = \sqrt{\frac{S_{w1} S_{w2}}{2 T_m RBW}} \quad (1.10)$$

Assuming the two channels identical $S_{w1} = S_{w2} = S_w$, eq. 1.10 can be simplified with

$$\sigma_{\tilde{S}} = S_w \frac{1}{\sqrt{2 T_m RBW}} \quad (1.11)$$

The total measurement time can be estimated from the equation 1.11 imposing $S_{DUT} = \sigma_{\tilde{S}}$ (with the conventional assumption that a signal can be detected when its amplitude is at least

equal to the superimposed fluctuations, or $SNR = 1$); the measurement time has a quadratic dependence of the uncorrelated noise S_w

$$T_m = \frac{1}{2RBW} \left(\frac{S_w}{S_{DUT}} \right)^2 \quad (1.12)$$

In practice it's important to note that T_m derived by the equation 1.12 it's just the acquisition time of all the necessary samples to achieve a signal noise ratio $SNR = 1$ and does not include the time needed to perform the cross-correlation digital elaboration of data. ¹

1.2.2 Instrument's sensitivity

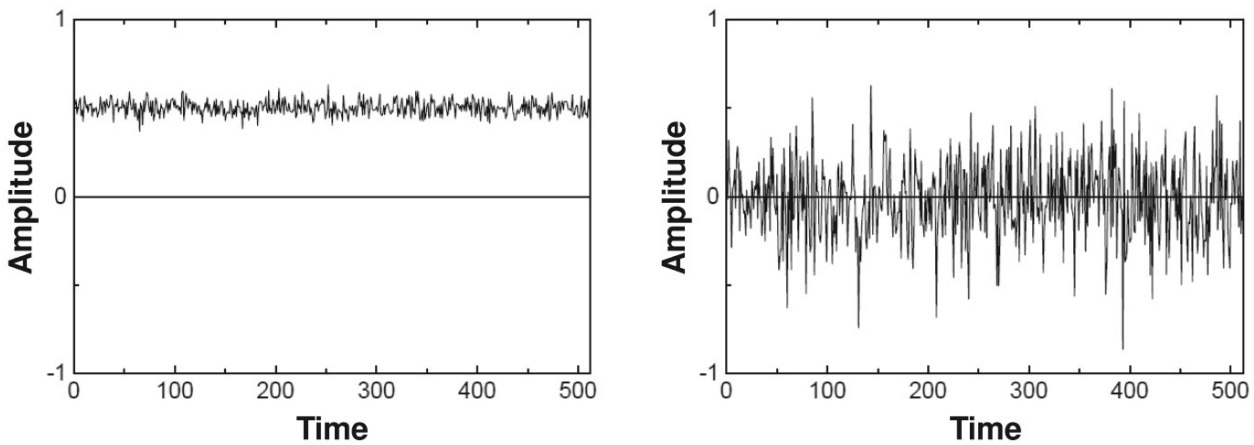


Figure 1.2: Output due to the instrumental noise: left with correlated noise, right with uncorrelated noise

The ultimate sensitivity limit of the correlation spectrum analyser is determined by the correlated noise present on both channels. This kind of instrumental noise gives an unknown value directly summed to the power spectral density of the input useful signal. Figure 1.2 shows the contribution of the two different types of noise, uncorrelated and correlated, on the measured power spectral density. On the left of the figure is reported the output in the case of a white correlated noise; on the right is reported the case of a white uncorrelated noise after a finite average time. The correlated noise, that cannot be removed by the cross-correlation because it is present on both channels, acts on the average value of the measure while uncorrelated acts on the dispersion around average value.

The topology of front-end stages and the DUT characteristics have direct impact on the amount of this two types of noises, as shown in sections 1.4 and 1.5; is important to highlight how they influence the electronic design choices.

- correlated noise corresponds to the minimum detectable input signal (definition of $SNR=1$) and therefore sets the ultimate limit for the instrument's sensitivity
- uncorrelated noise determines the measurement time needed to reach a given value of sensitivity (as stated in equation 1.12); an infinite measurement time is needed to eliminate all uncorrelated noise and reach the ultimate sensitivity limit imposed by correlated noise

¹Currently this is the main practical limit of the instrument: processing time can be up to two orders of magnitude bigger than acquisition time, depending on sampling frequency of adc and computer's performance.

The design of a specific front-end stage must therefore take care of both types of noise: an excess of correlated noise make the cross-correlation technique useless in comparison to a classic single channel analyser, while a high level of uncorrelated noise can increase the measurement time to an infeasible amount.

1.3 Not-identical channels

All the considerations made so far are based on the ideal assumption that the two channels are perfectly identical: it's important to study the effect of the non uniformities between the transfer functions of the two channels on the measure. Uncorrelated noise is any case eliminated by the cross-correlation because there is no any phase relationship between the noises of the two channels; a difference in the transfer functions can not in any way create any phase relationship between channels. This mean that the necessary time to reduce the effect of uncorrelated noise does not undergo change due to differences of the channels. Instead the signal from the DUT and the correlated noise suffers from the asymmetries of the channels because they are present on both of them. By the equation 1.8 can be seen that a phase of $\Delta\phi$ between the channels causes a reduction of $\cos \Delta\phi$ of the useful signal which results in a decrease of instrument's sensitivity. However, due to the typical low difference of phase (less than 5° in the full bandwidth), this phenomenon is negligible in most cases.

Different gains can not modify the signal to noise ratio so there are no changes on the time required to reach a determined precision of the measurement, but a calibration of the instrument by measuring the gains of both channels is required to obtain a high accuracy of the correlation measure. It remains to consider a possible delay between the two channels caused by different paths from the front-end amplifier to the ADC or due to ADC itself. If this delays τ are small compared to sampling time T_c , they can be modelled as a phase difference between the channels that are a terms $e^{j\omega\tau}$ in the frequency domain. If the delay is greater than the sampling time, the fact that the sequences have finite number of samples must be taken in to account: in the extreme case of delay greater than NT_c the two sequences are distinct and completely uncorrelated: performing the correlation result in a void signal. In the most realistic case of a delay less than NT_c it can be shown that the result of the correlation on a white signal with σ_x^2 is:

$$\mathbf{E} \left[\frac{1}{NT_c} V_1(\omega) V_2^*(\omega) \right] = \sigma_x^2 \left(1 - \frac{\tau}{NT_c} \right) \cos(\omega\tau) \quad (1.13)$$

The cosine term is due to the mismatch between the two channels introduced by the delay. The other term of reduction takes into account that with the increase of the delay therefore linearly decrease the portion of the signal in common between the two channels; overall a delay between the two paths decrease the useful signal similar to a phase displacement, leading to an increased measurement time. At high frequencies the delay between the two channels is the dominant effect: for example at 20 MHz a difference of 0.4m between the two transmission cable is necessary to produce a 5% decrease of the useful signal (assuming a typical speed of coaxial cables to be half the speed of light). During the construction this aspect has been taken into account and both channels have the same topology, pcb layout dimension and internal wire connection. The critical aspect can be then the length of external connection between the instrument and the acquisition system: is therefore necessary to use coaxial cables of the same length for the connection of the two channels. [10]

1.4 Current mode front-end

In a current-mode front-end the useful signal coming from the device is read by a transimpedance stage. With this scheme is very easy to bias the DUT since is connected to a virtual ground, which follows the voltage applied at the non-inverting terminal of the opamp.

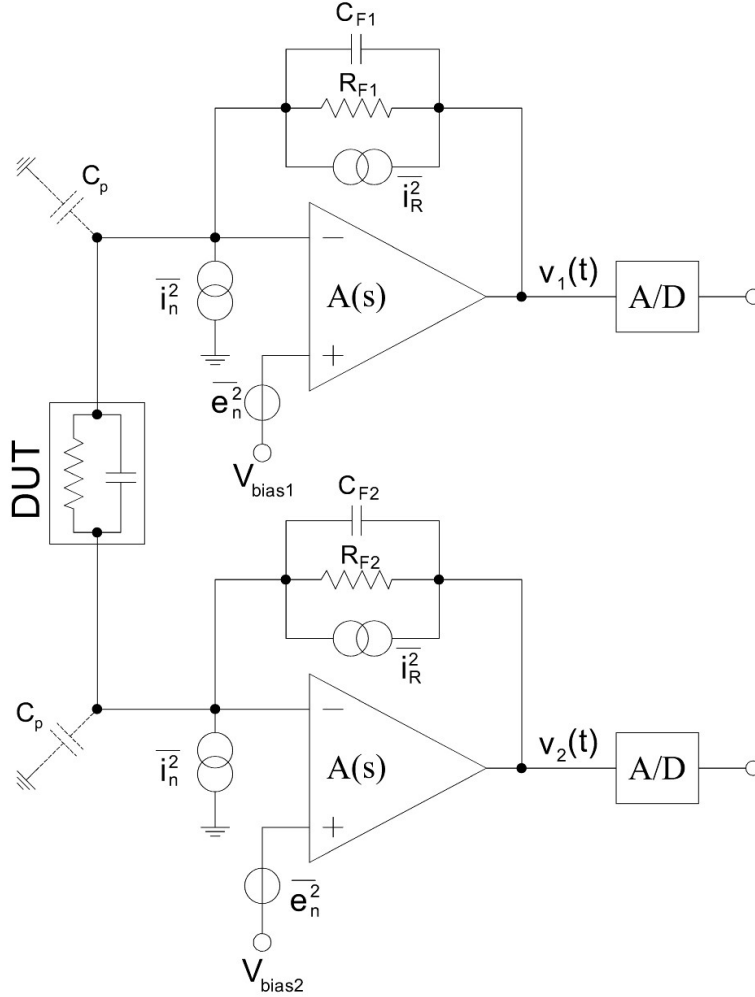


Figure 1.3: Generic transimpedance front-end

To obtain the correlated noise, and therefore find the performance limit of this topology, it is necessary to calculate the opamp's output signals V_1 and V_2 and then perform the cross-spectrum:

$$\text{Correlated noise} = \Re \{ \mathbf{E} [V_1(j\omega) V_2^*(j\omega)] \} \quad (1.14)$$

In the scheme 1.3 the voltages V_1 and V_2 are:

$$\begin{aligned}
V_1(s) &= V_{RF1,n} + I_{OA1,n}R_{F1} + E_{OA1,n} \left(1 + \frac{R_{F1}}{R_D \parallel \frac{1}{s(C_D+C_{p1})}} \right) + \sqrt{e_{nOA2}^2} \frac{R_{F1}}{R_D \parallel (1/sC_D)} \\
&= \sqrt{4KTR_{F1}} + \sqrt{i_{nOA1}^2} R_{F1} + \sqrt{e_{nOA1}^2} \left(1 + \frac{R_{F1}}{R_D \parallel \frac{1}{s(C_D+C_{p1})}} \right) + \sqrt{e_{nOA2}^2} \frac{R_{F1}}{R_D \parallel (1/sC_D)} \\
V_2(s) &= V_{RF2,n} + I_{OA2,n}R_{F2} + E_{OA2,n} \left(1 + \frac{R_{F2}}{R_D \parallel \frac{1}{s(C_D+C_{p2})}} \right) + \sqrt{e_{nOA1}^2} \frac{R_{F2}}{R_D \parallel (1/sC_D)} \\
&= \sqrt{4KTR_{F2}} + \sqrt{i_{nOA2}^2} R_{F2} + \sqrt{e_{nOA2}^2} \left(1 + \frac{R_{F2}}{R_D \parallel \frac{1}{s(C_D+C_{p2})}} \right) + \sqrt{e_{nOA1}^2} \frac{R_{F2}}{R_D \parallel (1/sC_D)}
\end{aligned} \tag{1.15}$$

where $V_{RF1,n}$, $V_{RF2,n}$ are the thermal noise of the feedback resistors, $I_{OA1,n}$, $I_{OA2,n}$ the equivalent current noise of the opamp, $E_{OA1,n}$, $E_{OA2,n}$ the equivalent voltage noise of the opamp, R_D is the DUT's resistance which, thanks to a proper V_{gs} biasing circuit, is the same from both channels. All the noise generators in the equation 1.15 are all independent of each other and then uncorrelated². Then the result can be obtained as the sum of separate contributions calculated individually. The opamp's input current noises $\overline{i_n^2}$ and the noises of the feedback resistances $V_{RF,n}$, since there are only on their respective channels, do not give contributions to correlated noise (they contribute only to uncorrelated noise of individual channels). The input voltage noise $\overline{e_{nOA1}^2}$, thanks to the feedback, causes a voltage variation of the virtual ground (the negative terminal of the opamp) which causes a current in the DUT which is read and amplified by both channels. These are the only correlated noise sources. The output voltage due to the single generator $\overline{e_{nOA1}^2}$ are

$$\begin{aligned}
V_1(j\omega) &= \sqrt{e_{nOA1}^2} \left(1 + \frac{R_{F1}}{R_D} \right) + j\omega \sqrt{e_{nOA1}^2} (C_D + C_{p1}) R_{F1} \\
V_2(j\omega) &= \sqrt{e_{nOA1}^2} \left(\frac{R_{F2}}{R_D} \right) + j\omega \sqrt{e_{nOA1}^2} C_D R_{F2}
\end{aligned} \tag{1.16}$$

Multiplying the parts of V_1 and V_2 that are in phase with each other it's possible to calculate how much of the noise $\overline{e_{nOA1}^2}$ is correlated between the two channels:³

$$\Re \{ \mathbf{E} [V_1(j\omega)V_2^*(j\omega)] \} = \overline{e_{nOA1}^2} \left[\left(1 + \frac{R_{F1}}{R_D} \right) \frac{R_{F2}}{R_D} + \omega^2 R_{F1} R_{F2} (C_D + C_{p1}) C_D \right] \tag{1.17}$$

The contribution due to $\overline{e_{nOA2}^2}$ is similar:

$$\Re \{ \mathbf{E} [V_1(j\omega)V_2^*(j\omega)] \} = \overline{e_{nOA2}^2} \left[\left(1 + \frac{R_{F2}}{R_D} \right) \frac{R_{F1}}{R_D} + \omega^2 R_{F2} R_{F1} (C_D + C_{p2}) C_D \right] \tag{1.18}$$

This correlated noise is calculated at the output of the amplifiers. It is more useful to give the equivalent noise at the input to make direct comparison with the signal from the DUT.

²In a case of bjt opamp this assumption is not completely true. For the following calculations, however, all noises will be considered independent of one another.

³For the orthogonality property, the correlation of signals equal but out of phase by 90° (in quadrature) is zero.

This can be done by dividing the outputs V_1 and V_2 by the respective gains in the bandwidth of the instrument (ie dividing the final result of correlation by $(R_{F1} \cdot R_{F2})$).

$$\begin{aligned} \overline{i_{n\text{correlated}}^2} &= \overline{e_{nOA1}^2} \left[\left(\frac{1}{R_{F1}} + \frac{1}{R_D} \right) \frac{1}{R_D} + \omega^2 (C_D + C_{p1}) C_D \right] + \\ &+ \overline{e_{nOA2}^2} \left[\left(\frac{1}{R_{F2}} + \frac{1}{R_D} \right) \frac{1}{R_D} + \omega^2 (C_D + C_{p2}) C_D \right] \end{aligned} \quad (1.19)$$

Using the same structure and operational amplifiers for both channels, the equation can be

simplified by imposing $\overline{e_{nOA1}^2} = \overline{e_{nOA2}^2} = \overline{e_{nOA}^2}$, $R_{F1} = R_{F2}$, $C_{p1} = C_{p2}$:

$$\overline{i_{n\text{correlated}}^2} = 2\overline{e_{nOA}^2} \left[\left(\frac{1}{R_F} + \frac{1}{R_D} \right) \frac{1}{R_D} + \omega^2 (C_D + C_p) C_D \right] \quad (1.20)$$

This value can be compared directly with the signal from the DUT fixing the ultimate

limit of sensitivity of the instrument. The magnitude of the correlated noise is inversely proportional to the impedance of the DUT: higher is the impedance higher is the separation between channels. At low frequencies the 1/f noise component of $\overline{e_{nOA}^2}$ may be the limiting factor. Special care should therefore be taken when designing the transimpedance amplifier by choosing low 1/f noise components for the input stage. At high frequencies, the second term in 1.20 increases and becomes the limiting factor when the capacitance of the DUT is particularly large: this is unavoidable and practically sets the effective bandwidth of the instrument. It is evident that this front-end topology is well suited for the characteristic of active devices and sensor based on mos structure or inverse biased diodes and piezoelectric sensors.

The uncorrelated noise value, affecting the required measuring time for reaching given sensibility, can be expressed, referring to the figure 1.3, as:

$$\overline{i_{n\text{uncorrelated}}^2} = \overline{i_{nOA}^2} + \frac{4KT}{R_F} + \overline{e_{nOA}^2} \cdot \frac{1}{R_F^2} \left| 1 + \frac{R_F}{Z_D} \right|^2 \quad (1.21)$$

with

$$Z_D = \frac{R_D}{1 + sR_D(C_D + C_p)} \quad (1.22)$$

It is useful to highlight the role played, both in correlated and uncorrelated equations, of the operational amplifier's noises sources. To minimize the instrument's correlated noise, and therefore decrease the threshold for a minimum detectable signal, the equation 1.20 suggest to chose an operational amplifier with the lowest possible $\overline{e_{nOA}^2}$ equivalent series noise; consequently from the equation 1.21 the uncorrelated noise becomes dominated by the opamp's current noise $\overline{i_{nOA}^2}$ and if this value is too high the minimum detectable signal, imposed by correlated noise, requires an excessively long measure time as indicated by equation 1.12: in fact both correlated and uncorrelated noise determines the overall instrument sensibility. Another key component for the current-mode front-end overall performance is the choice of

the feedback resistor R_F which affect both correlated and uncorrelated noise, the maximum dut's bias current and the transimpedance bandwidth: these requirements are in conflict with each other and therefore there is no optimal R_F value.

Because of this many degrees of freedom and interdependencies, there are not an ideal design but it must originate from the dut's characteristics (impedance, bias and expected noise) and a trade-off between the requirements in term of bandwidth and maximum available time for the measure.

1.5 Voltage-mode front-end

A voltage mode front-end is made by two identical voltage amplifier stage with their inputs connected together, as shown in figure 1.4. This structure is ideal when the DUT's resistance is *low* because minimize the correlated noise generated by the amplifier's input-equivalent noise generator.

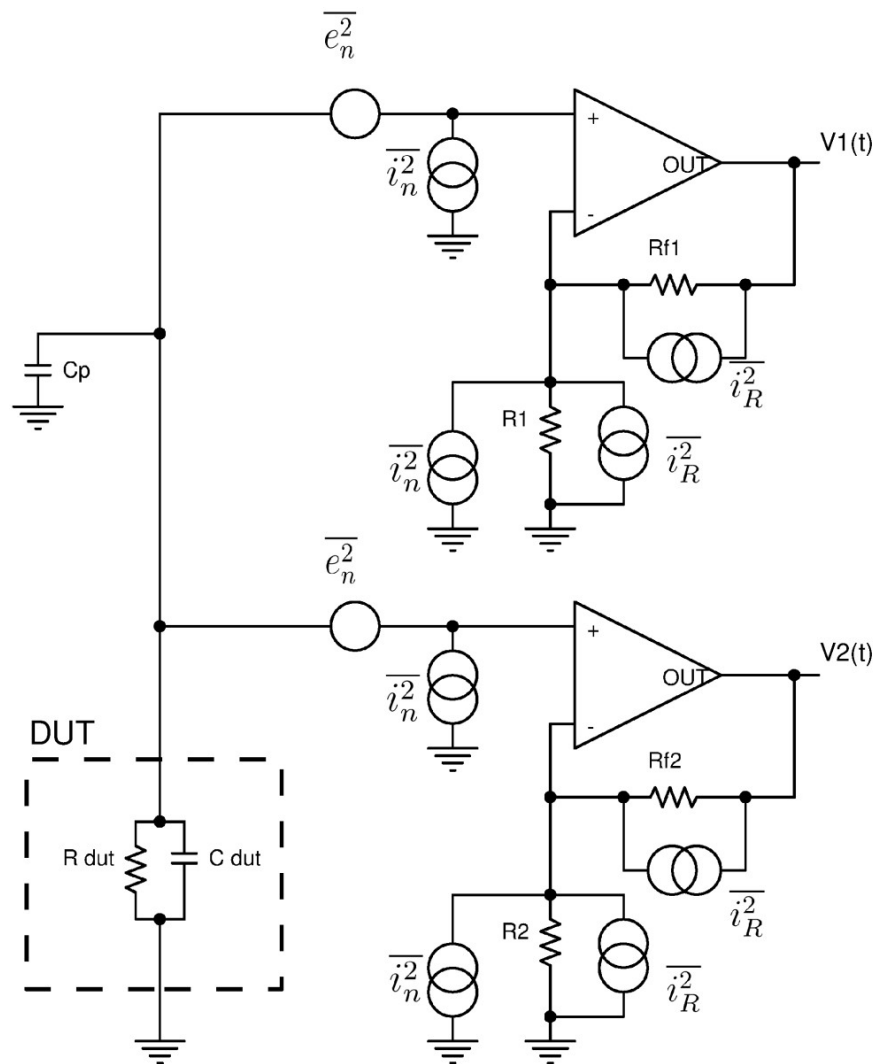


Figure 1.4: Voltage mode front-end: all possible noise sources are indicated

To calculate the correlated noise we must calculate the opamp's output signals V_1 and V_2 and then perform the cross-spectrum:

$$\text{Correlated noise} = \Re \{ \mathbf{E}[V_1(j\omega)V_2^*(j\omega)] \} \quad (1.23)$$

In the scheme 1.4 the voltages V_1 and V_2 are:

$$V_1(s) = [e_{n1} \cdot G_1] + [i_{n1+} \cdot Z_{dut} \cdot G_1] + [R_{F1} \cdot (i_{n1-} + i_{R1} + i_{RF1})] + [i_{n2+} \cdot Z_{dut} \cdot G_1] \quad (1.24)$$

$$V_2(s) = [e_{n2} \cdot G_2] + [i_{n2+} \cdot Z_{dut} \cdot G_2] + [R_{F2} \cdot (i_{n2-} + i_{R2} + i_{RF2})] + [i_{n1+} \cdot Z_{dut} \cdot G_2] \quad (1.25)$$

where Z_{DUT} is the impedance of the dut and parasitic capacitance of the nets between dut and amplifiers, G_1 and G_2 the non inverting gain of channel 1 and channel 2, respectively

$$Z_{DUT} = \frac{R_{DUT}}{1 + S \cdot R_{DUT} \cdot (C_{DUT} + C_P)} \quad (1.26)$$

$$G_1 = \left(1 + \frac{R_{F1}}{R_1} \right)$$

$$G_2 = \left(1 + \frac{R_{F2}}{R_2} \right)$$

i_{RF1} , i_{RF2} , i_{R1} , i_{R2} are the thermal noise of the resistors, i_{n1-} , i_{n1+} , i_{n2-} , i_{n2+} the equivalent current noise of the opamps, e_{n1} , e_{n2} the equivalent voltage noise of the opamps, R_{DUT} is the DUT's resistance and C_{DUT} it's capacitance. All the noise generators in the equations 1.24 and 1.25 are considered completely independent of each other and then uncorrelated. Therefore the result can be obtained as the sum of separate contributions calculated individually. The opamp's input voltage noises e_{n1} , e_{n2} , and the noises of the feedback resistances i_{RF1} , i_{RF2} , i_{R1} , i_{R2} , since there are only on their respective channels, do not give contributions to correlated noise (they contribute only to uncorrelated noise of individual channels). The input current noise i_{n1+} and i_{n2+} at the non-inverting inputs of the operational amplifiers, due to dut's impedance, causes a voltage variation across the dut, which is then read by both channels and are the sources of correlated noise.

Considering only these generators the equations 1.24 and 1.25 can be simplified

$$V_1(s) = [i_{n1+} \cdot Z_{dut} \cdot G_1] + [i_{n2+} \cdot Z_{dut} \cdot G_1] \quad (1.27)$$

$$V_2(s) = [i_{n2+} \cdot Z_{dut} \cdot G_2] + [i_{n1+} \cdot Z_{dut} \cdot G_2]$$

The output voltages due to the single generator i_{n1+} are

$$V_1(s) = i_{n1+} \cdot Z_{dut} \cdot G_1 \quad (1.28)$$

$$V_2(s) = i_{n1+} \cdot Z_{dut} \cdot G_2$$

and therefore

$$\begin{aligned} V_1(j\omega) &= \left[i_{n1+} G_1 \frac{R_{DUT}}{1 + (\omega R_{DUT}(C_{DUT} + C_P))^2} \right] - j\omega \left[i_{n1+} G_1 \frac{R_{DUT}^2(C_{DUT} + C_P)}{1 + (\omega R_{DUT}(C_{DUT} + C_P))^2} \right] \\ V_2(j\omega) &= \left[i_{n1+} G_2 \frac{R_{DUT}}{1 + (\omega R_{DUT}(C_{DUT} + C_P))^2} \right] - j\omega \left[i_{n1+} G_2 \frac{R_{DUT}^2(C_{DUT} + C_P)}{1 + (\omega R_{DUT}(C_{DUT} + C_P))^2} \right] \end{aligned}$$

Multiplying the parts of V_1 and V_2 that are in phase with each other it's possible to calculate how much of the noise i_{n1+} is correlated between the two channels: ⁴

$$\Re \{ \mathbf{E} [V_1(j\omega)V_2^*(j\omega)] \} = \overline{i_{n1+}^2} [G_1 G_2 |Z_{DUT}|^2 + \omega^2 G_1 G_2 |Z_{DUT}|^2 R_{DUT}^2 (C_{DUT} + C_P)^2] \quad (1.29)$$

The contribution due to i_{n2+} is similar:

$$\Re \{ \mathbf{E} [V_1(j\omega)V_2^*(j\omega)] \} = \overline{i_{n2+}^2} [G_2 G_1 |Z_{DUT}|^2 + \omega^2 G_2 G_1 |Z_{DUT}|^2 R_{DUT}^2 (C_{DUT} + C_P)^2] \quad (1.30)$$

From equations 1.29 and 1.30 it is possible to obtain the total correlated noise at the amplifiers output. Since the two channels are identical some simplifications can be made: $G_1 = G_2 = G$ and $\overline{i_{n1+}^2} = \overline{i_{n2+}^2} = \overline{i_n^2}$

$$\overline{v_{n\text{correlated},out}^2} = 2\overline{i_n^2} [G^2 |Z_{DUT}|^2 (1 + \omega^2 R_{DUT}^2 (C_{DUT} + C_P)^2)] \quad (1.31)$$

This correlated noise is calculated at the output of the amplifiers. It is more useful to give the equivalent noise at the input to make direct comparison with the signal from the DUT. This can be done by dividing the outputs V_1 and V_2 by the respective gains in the bandwidth of the instrument.

$$\overline{v_{n\text{correlated},in}^2} = 2\overline{i_n^2} [|Z_{DUT}|^2 (1 + \omega^2 R_{DUT}^2 (C_{DUT} + C_P)^2)] \quad (1.32)$$

The uncorrelated noise, input equivalent, can be expressed as

$$\overline{v_{n\text{uncorrelated},in}^2} = \overline{e_n^2} + \overline{i_n^2} \left(Z_{DUT}^2 + \frac{R_F^2}{G^2} \right) + \frac{R_F^2}{G^2} \frac{4KT}{R} + \frac{R_F}{G^2} 4KT \quad (1.33)$$

As for the current-mode front-end previously discussed, some general consideration can be made about the design of a voltage-mode front-end.

1.6 Current versus voltage measurement

As most of the primary physical noise sources in electronic devices are in the form of current, the current-mode scheme is often preferred. It has practical advantages in term of simplicity of connection since almost all of integrated semiconductor devices can be biased directly through the instrument transimpedance amplifiers, avoiding an external bias and coupling network; its weak point is the high level of correlated noise for devices with low impedance value. Consequently, the parameter to make the choice between current-mode or voltage-mode set-up is the dut's impedance.

⁴For the orthogonality property, the correlation of signals equal but out of phase by 90° (in quadrature) is zero.

Chapter 2

Instrument overview

As indicated in section 1.6 there is no an optimal front-end topology for all type of devices but instead the circuit must be adapted to the device characteristic, especially its impedance, to minimize correlated and uncorrelated noise and improve the sensibility. Previous version of the correlation spectrum analyser have, for simplicity of construction, front-end and all other circuits on a single board: they were then optimized for a specific type of dut ¹ but completely unsuitable for all other types. To improve the situation was decided to build this new version with a modular structure, showed in figure 2.1, as its main feature: the front-end is interchangeable while all others control and amplification circuits are placed on a dedicate distinct board, the mainboard, which is more complex compared to the equivalent function circuits on the old version, but can interface and manages virtually all type of present and future front-end without needing to be replaced or updated. The new other important feature is the system control scheme; all old instruments have trimmers and switches to set the bias voltages and three digit lcd display to show it to the user. These manual control suffer from generally low precision, temperature drift and are tiresome to use when the front-end have filters on dut bias voltages with sub-second time-constant and non-lineare dependence between applied bias voltage and current, as a mosfet for an example. In this new instrument all manual control are removed, replaced by a National Instruments DAQ pci control board placed installed inside the computer: therefore the software has changed, integrating both signal processing and instrument control.

¹Mosfet devices with relatively high, up to 1mA, channel current.

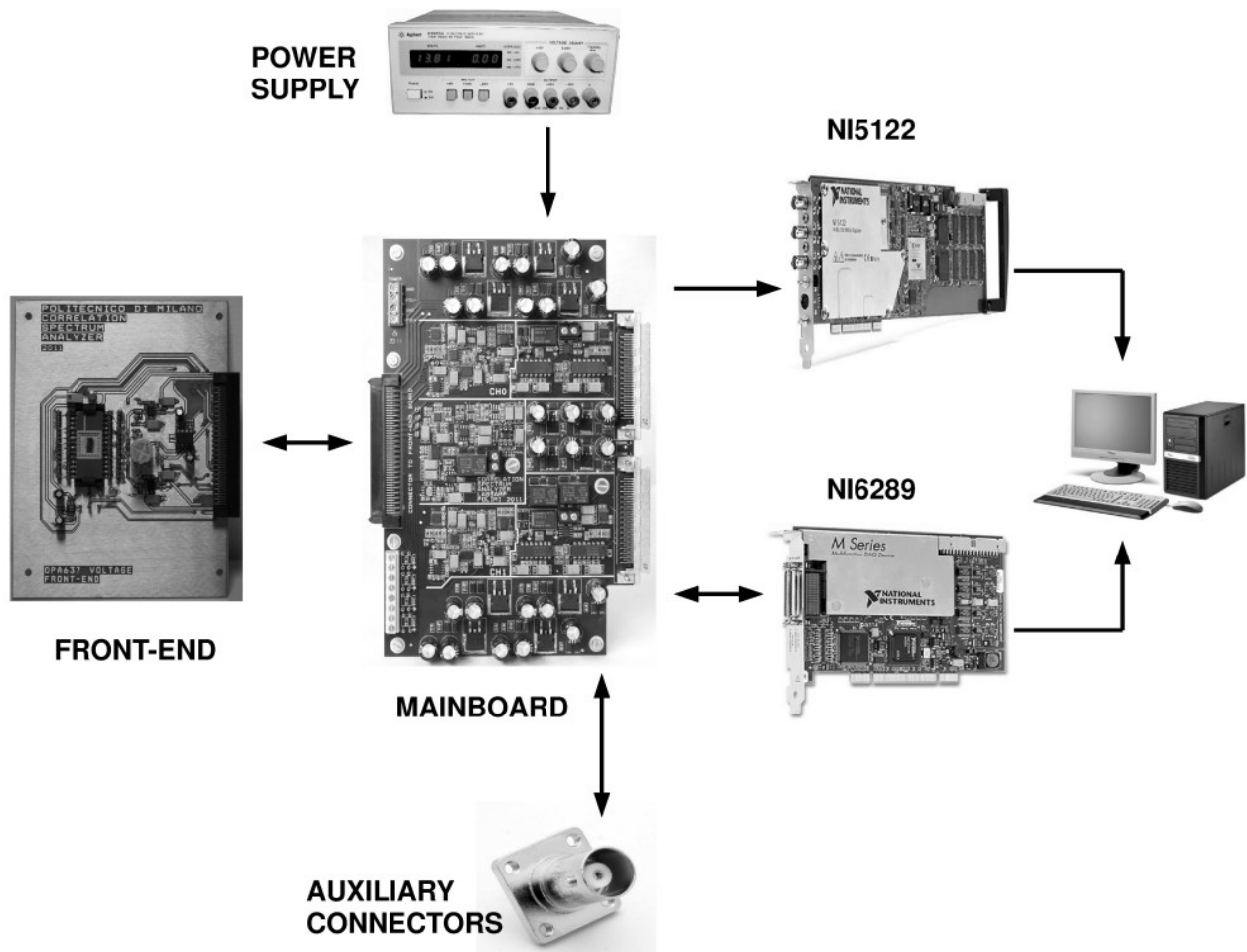


Figure 2.1: Overview of the instrument components and connections

Mainboard to Front-End connection

Front-end and mainboard are connected by a 100 pins 90 degree insertion connector; about half of this pins are dedicated to signals:

- analog signal from the front-end amplifiers output to the mainboard stages inputs
- power supply
- lines from NI6289 control board to the front-end: among these there are adc analog inputs, dac outputs and gpio digital signals; this give an high level of versatility to allow future development of any possible type of new front-end.
- pass - through lines from auxiliary bnc connectors

The remaining $\cong 50$ pins are dedicated to ground, to provide a good reference plane on the front-end board and a low inductance return path for the output signal of the front-end amplifiers.

Power Supply

The instrument must be powered by external dual $\pm 20V$ power supply with at least 500mA of output current. The on-board voltage regulator can run down to $\pm 17V$ and up to $\pm 35V$ without any performance degradation, but with increased heat production since there are only linear regulators on the mainboard.

Auxiliary connectors

There are four general purpose bnc connectors on the instrument front-panel. They are simply connected to the mainboard and then to the front-end through the 100 pin connector. Any laboratory instrument can be connected at these bnc's to measure or give additional bias voltages. During the thesis work was typically used when the voltages generated by the NI6289 board are too low to correctly bias the dut².

Fast digitizer NI-5122

This board is the digital part of the instrument: it has dual 14bit 100MS/s ADC's, one for each channel, with variable input gain and full scale level, selectable input impedance (50 Ω or 100M Ω , AC or DC coupling) and 32MB/Channel on-board memory. All its parameters are configurable by software.

Multifunction board NI6289

The NI-6289 is a high accuracy multifunction data acquisition board with 18 bits input ADCs and 16 bits output DACs and a number of GPIO pins. It is used to drive all digital command signals (relays, programmable output amplifiers, analog multiplexers) required to configure the instrument. Its output DAC's can swing between $\pm 10V$ and goes directly to the front-end board through the mainboard to front-end connector and are typically used to bias the dut, depending on the front-end type. Input ADC's are used to acquire DC outputs of front-end boards.

2.1 Physical design and layout

The main-board and the front-end are placed inside a thick rectangular aluminium enclosure: the entire instrument is visible in figure 2.2. On the right side there is a rectangular aperture for two multi-polar connectors to the NI6289 control board; on the same side there are the two channel's output bnc which must be connected to the NI5122 acquisition board. The pass-through connector are on the front-side while power connectors and switch are placed on the rear panel. To maximize the shielding effect the lid, not visible in the image, is electrically connected to box with a copper cable: this makes the entire enclosure a Faraday cage, preventing electromagnetic interference to enter the instrument and to be collected from the dut.³

²This has happened with Ofet devices

³Due to high sensibility of the instrument some interferences, especially from mains power networks, are always present in the acquired spectra.

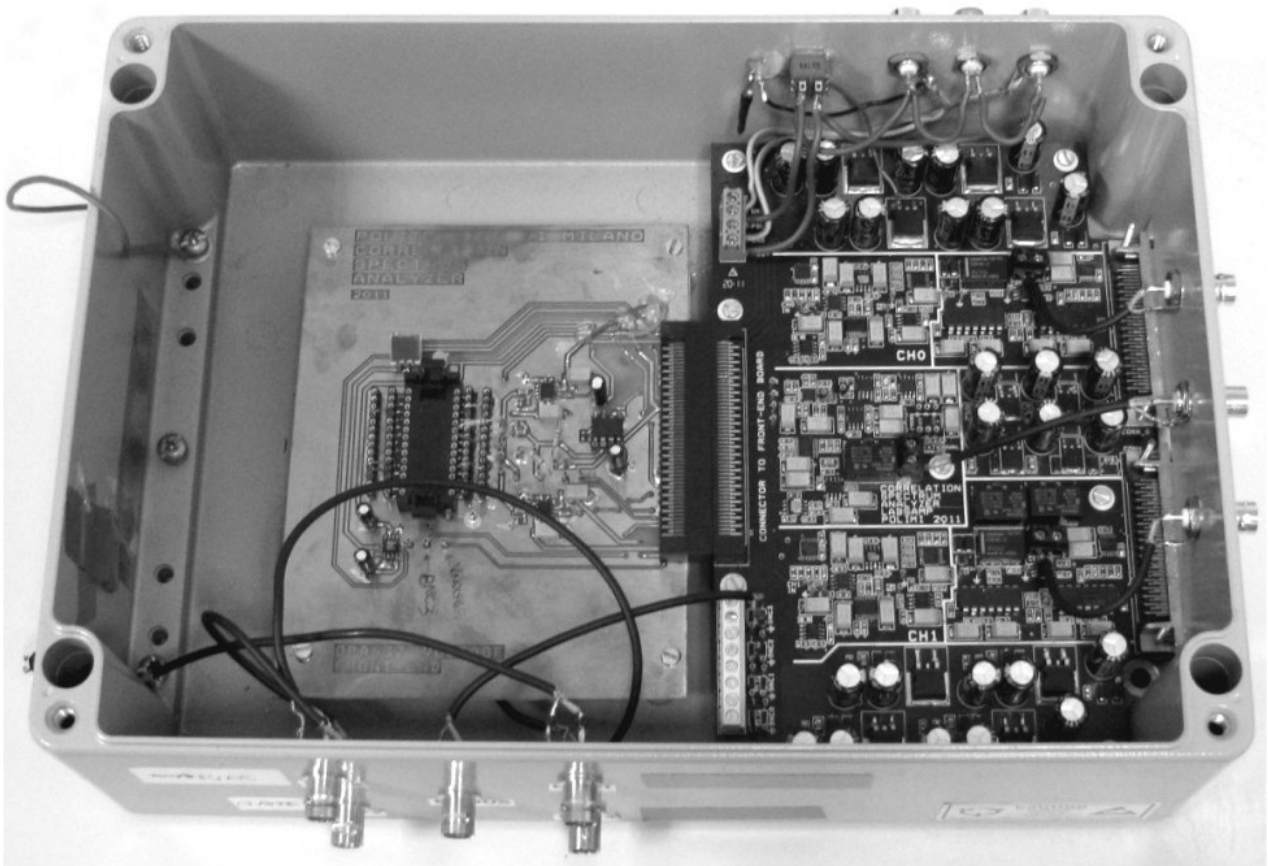


Figure 2.2: The instrument viewed from top side without cover lid. The mainboard is the board on the right

2.2 Graphical User Interface

The two National Instruments boards, and consequently the entire instrument, are controlled by a pc software developed in Visual Basic that give a full Graphical User Interface (GUI) to end users. The current appearance of the GUI is still of a debugging interface, with some advanced parameters for hardware low-level control; however it allows high level use of the instrument also without a complete and deep knowledge of underlying hardware. Figure 2.3 is the main control windows. The main graph shown the signals at the inputs of the NI5122 digitizer in real time: this feature allows to verify the output of the correlation spectrum analyser at the beginning of a measurement session and consequently set all the mainboard control parameters to keep the acquired signals in the correct range to avoid adc's saturation or under-use of their input dynamic; in fact this windows acts like an oscilloscope and therefore its control, the trigger and adc box, refer to those of an oscilloscope. The remaining area is occupied by various control reconfigured depending on the used front-end: at the start-up the software shown a pop-up windows to let the user to choose which of them is connected.

A specific control box, shown in figure 2.4, is dedicated to set-up and start the spectrum acquisition. Here is possible to choose between different measurement type (cross correlation between channels, single channel spectrum, ratio between channels, etc...) and enter the file name in which the measurements will be saved. At the end of a measure the software save two different file, named *genericfilename.scsa* and *genericfilename.cfg*: the first contain the result spectrum in form of a raw data, the second is a standard ascii text file reporting all

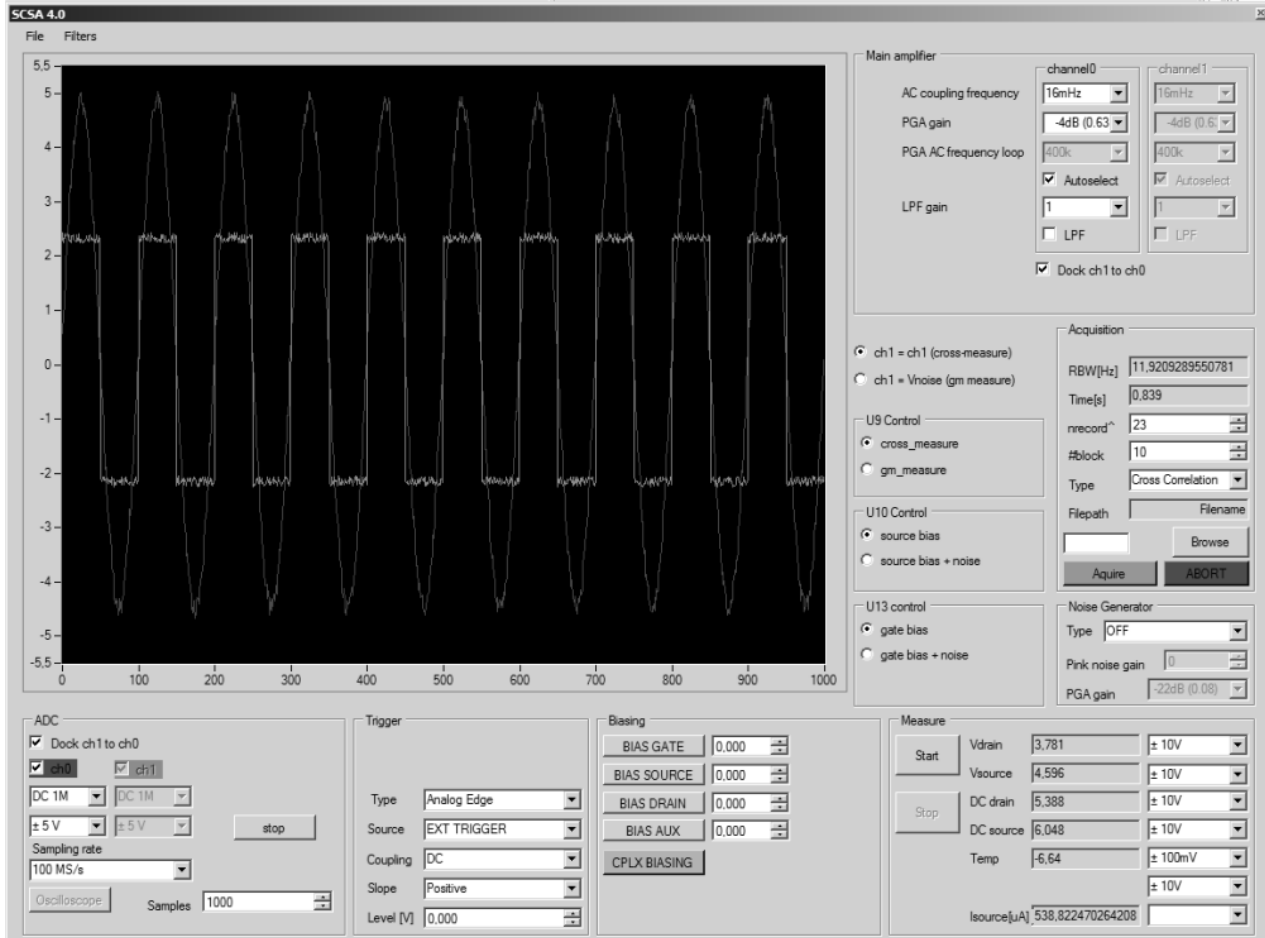
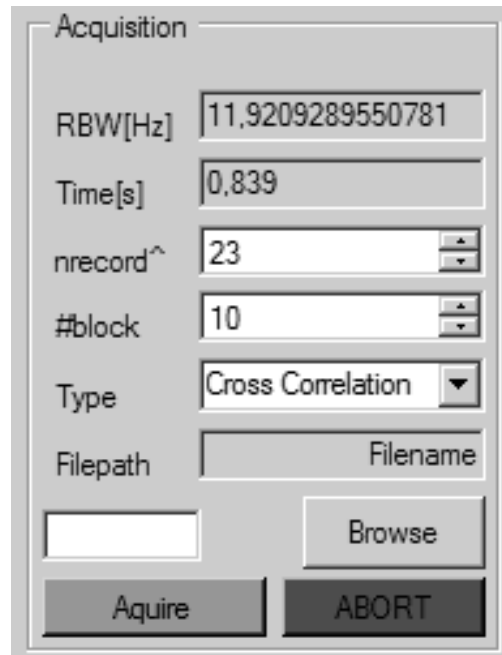


Figure 2.3: Main window of the instrument's control software

the hardware and software settings of the measure. It was decided to give the maximum possible control over the spectrum measures, therefore the two most important setting for a spectrum measure are the *nrecord* and *block* fields: $2^{nrecord}$ is the number of samples of the single acquisition block, block is the total number of block to acquire. From this two values, and sampling-rate, the software compute and shown the corresponding values of RBW and total acquisition time. At the press of the acquire button the instrument start the acquisition routine.

The other important software component is the file viewer, showed in figure 2.5 with a real magneto-resistance noise spectrum. With this tool is possible to open and view the saved .scsa file which contain the saved spectrum. It is also possible to convert a single raw .scsa file, or an entire folder, to standard .csv files that can be easily used for further post-processing.



Acquisition

RBW[Hz] 11,9209289550781

Time[s] 0,839

nrecord^ 23

#block 10

Type Cross Correlation

Filepath Filename

Figure 2.4: Signals acquisition control box: $RBW[Hz]$ and $Time[S]$ are read only fields, their value are calculated from nrecord, block and sampling rate entered values.

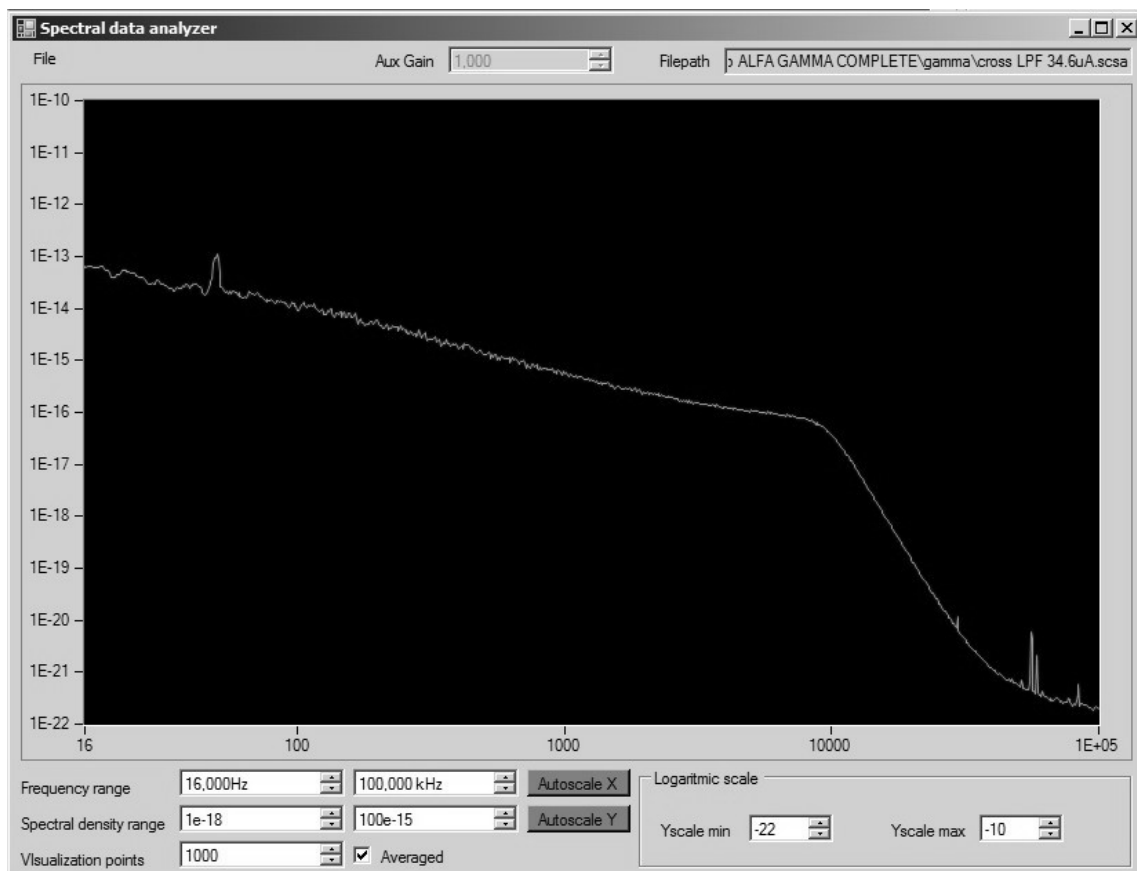


Figure 2.5: Visualization window for the acquired file. Axis limits are automatically sets by an autoscale algorithm, but can be manual entered by the end user

Chapter 3

Design of the mainboard

3.1 Mainboard function and capabilities

As shown in the chapter 2 the mainboard constitutes a central key component of the overall instruments: it is an hub between the front-end, control board, data acquisition board and external auxiliary signals which can be brought by bnc connectors. On the mainboard are placed the two main amplifier circuit, one for each channel, whose purpose is basically to take the signals from the front-end and drive the ADC placed on external NI5122 acquisition board inside the pc. They are in fact voltage amplifier with a band-pass transfer function: middle-frequency gain, high-pass and low-pass cut frequency are all configurable. There are also configurable noise generator, useful to do characterization measure on the DUT, for example transconductance g_m measure on a transistor type device. In figure 3.1 is shown a high level diagram of all circuit block; dark lines represent the analog signal path, while the grey ones are digital control signals. On the mainboard are placed all the power supply circuits for both the mainboard itself and the front-end.

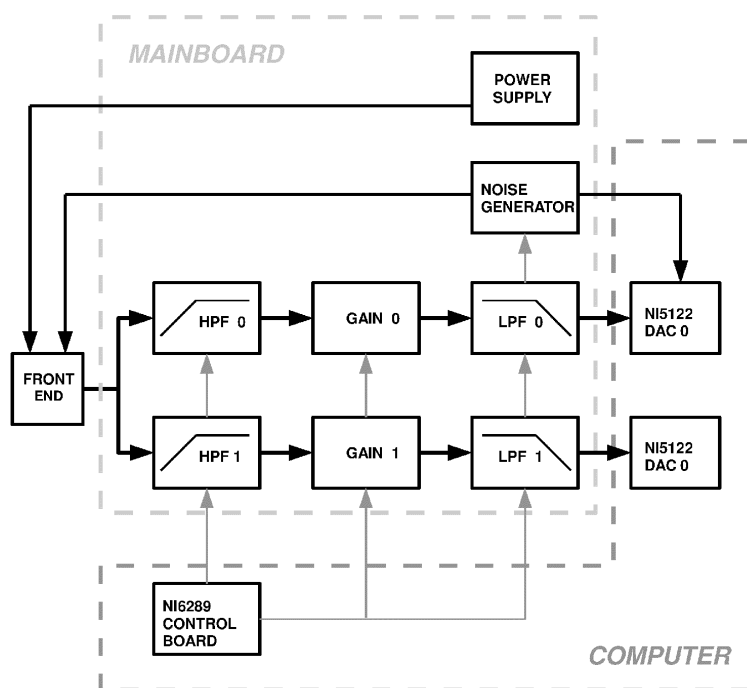


Figure 3.1: Block scheme of the mainboard subsections and their interconnections

3.2 Channel Amplifier

The channel's amplifiers on the mainboard amplifies the front-end output signal up to a useful level for the ADC in the acquisition board; since the front-end is interchangeable, and the acquisition board's full scale is selectable in a wide range from $\pm 100mV$ to $\pm 10V$, it's not possible to define a ideal fixed gain value; thus was decided to make the overall amplifier configurable by control software with selectable values for upper and lower bandwidth limits and middle frequency gain.

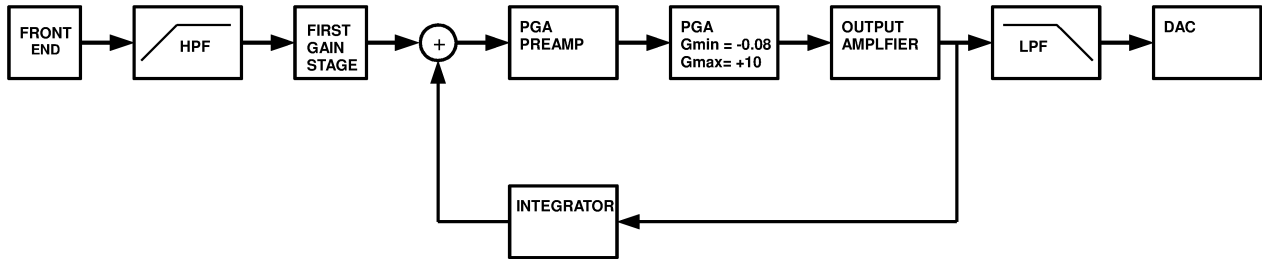


Figure 3.2: Diagram of operation of the acquisition channel amplifier on the mainboard

The overall design, visible in figure 3.2, start with an high-pass filter to remove the dc component always present at the output of the front-end stage due to its various offset source or as a result of dut polarization; for example in a current-mode front-end as the one described in section 1.4 the output of the transimpedance amplifiers reach almost the power rails when provide the maximum dut's bias current. Subsequently the first stage, in addition to provide some of the overall gain, decouple the filter from the programmable and output stage. The programmable gain amplifier can both amplify or attenuate the signal: this feature allows to obtain, with the maximum attenuation, an overall gain around unity for the mainboard channel amplifier, useful when the signals from the front-end swings almost rail to rail and therefore no amplification is needed to feed the acquisition board. An integrator placed in feedback loop remove the dc offset generated by the pga and output stage, which could saturate the adc when they are set at the lowest input range. An optionally low pass filter of $\cong 10kHz$ at the end of the chain allows to use low adc sampling rate and therefore reduce both the minimum detectable frequency and processing time when the full instrument bandwidth is not needed or the front-end is specifically designed for low frequencies.

3.2.1 High pass filter and first gain stage

To avoid high amplification of the dc voltage, always present at the front-end output due to offset or dut bias, the first stage is composed by an C-R high-pass filter whit fixed $C_{in} = 1\mu F$ capacitor and four selectable R_{in} of $1G\Omega$, $10M\Omega$, $300k\Omega$, $10k\Omega$ to obtain an high pass frequency of $160\mu Hz$, $16mHz$, $0,53Hz$, $16Hz$, respectively. The R_{in} selection is made by the ADG1409, a digitally controlled analog multiplexer.

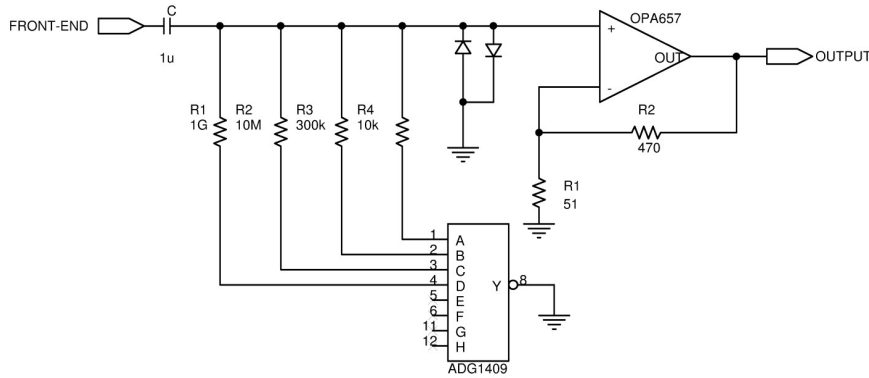


Figure 3.3: AC Coupling and first amplifier stage

To decouple the filter from the subsequent stages, the first gain stage is made by an operational amplifier in non-inverting configuration which must have the following characteristics:

- high input impedance, to not alter the filter response when the $R_{in} = 1G\Omega$ is selected
- low voltage offset and low input bias current, to avoid high dc offset at the output
- required bandwidth
- lowest possible noise, to not add additional uncorrelated noise

The ideal amplifier was found to be the J-Fet input OPA657, which has $R_{in} = 10^{12}\Omega$, $I_{bias} = 2_pA$, $V_{os} = 0.25mV$ from which follows a maximum output dc offset of $2.25mV$ when using $R_{in} = 1G\Omega$. It's voltage noise is $4.8nV/\sqrt{Hz}$, a very low value thanks to it's J-Fet input stage; this allow to ignore completely the mainboard amplifier's noise from the calculation of correlated and uncorrelated noise, which therefore depend exclusively by the front-end design. This opamp have an absolute maximum of $\pm 6.5V$ for supply voltage and input voltage range, thus is powered by the $\pm 5V$ rails. The front-end stage may instead be powered by both $\pm 15V$ and $\pm 5V$ rails, depending by the front-end design; therefore up to $\pm 15V$ can be theoretically present at the input of the OPA657, typically due to a step-change in the dut's bias voltage and a consequent temporary saturation of the front-end amplifier stage. To avoid damage at the OPA657 there are two diodes, placed in a back-to-back topology at the input of the operational amplifier: during normal cross-correlation measure the output of the front-end are very low, ideally only the noise of the front-end itself ¹, well below the diodes threshold voltage which act as an open circuit; they go in forward conduction only when the output of the front-end reach the threshold voltage, acting as a simple clamping protection. The OPA657 is configured in a non inverting-topology, giving a gain of $(1 + (R_1/R_2)) \cong 10,2$ and a $-3dB$ bandwidth of approximately $275MHz$

¹Overall the cross-correlation spectrum analyser are useful when the input signals coming from the dut are of the same magnitude, or even lower, of the front-end instrumental noise.

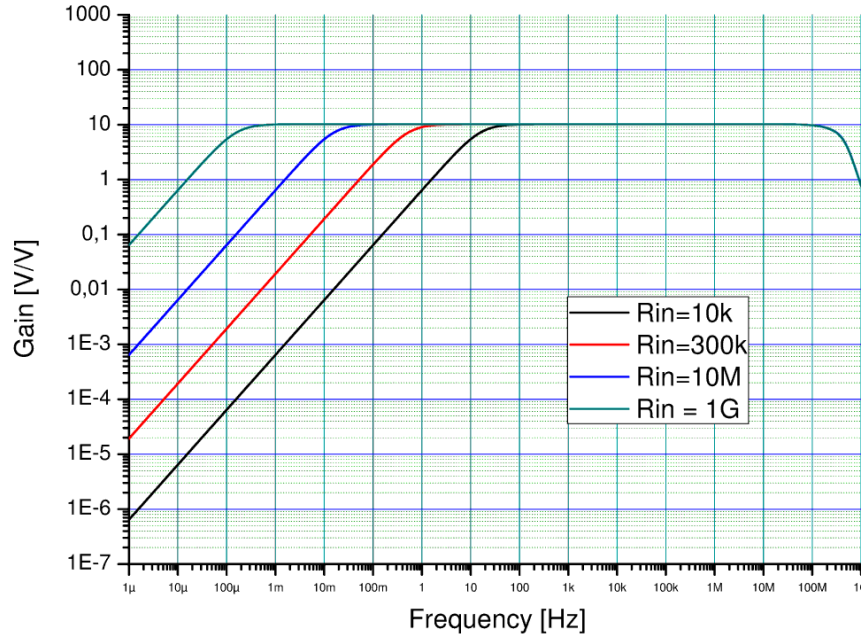


Figure 3.4: Simulation of first amplifier stage and ac coupling transfer functions, for each selectable R_{in}

Figure 3.4 reports simulations of the high pass filter and first gain stage for each selectable R_{in}

3.2.2 Programmable Gain Amplifier, Output Stage

The second part of the channel's amplifier is based on two integrated circuit, THS7001 and THS3091, both from Texas Instruments. The first is a high-speed programmable-gain amplifiers that consists of a separate low-noise input preamp and a programmable gain amplifier (PGA). The preamp is a voltage-feedback amplifier offering a low $1.7nV/\sqrt{Hz}$ voltage noise with a 100MHz (-3dB) bandwidth. The output pin of the preamp is accessible so that filters can be easily added to the amplifier. The 3bit digitally-controlled PGA provides a -22dB to 20dB gain range with a 6dB step resolution. In addition, the PGA provides both high and low output clamp protection to prevent the output signal from swinging outside the common-mode input range of the subsequent stage. The PGA provides a wide 70MHz (-3 dB) bandwidth, which remains relatively constant over the entire gain/attenuation range. These devices operate up to $\pm 16V$ supply voltage range thus is powered by the $\pm 15V$ rails. The preamp is configured as an inverting amplifier, with a gain of $-(R_1/R_2) = 2$ to make the sum of the signals from the preceding stage and from the active integrator loop. The PGA simply take the preamp-output, amplify it and drive the next stage made by the THS3091; this one is made by a current-feedback amplifier with a non-inverting gain of $(1+(R_1/R_2)) = 5$ which have enough strength (output current, slew rate, large signal bandwidth) to drive the 50Ω terminated transmission line formed by the coaxial cable and the acquisition board.

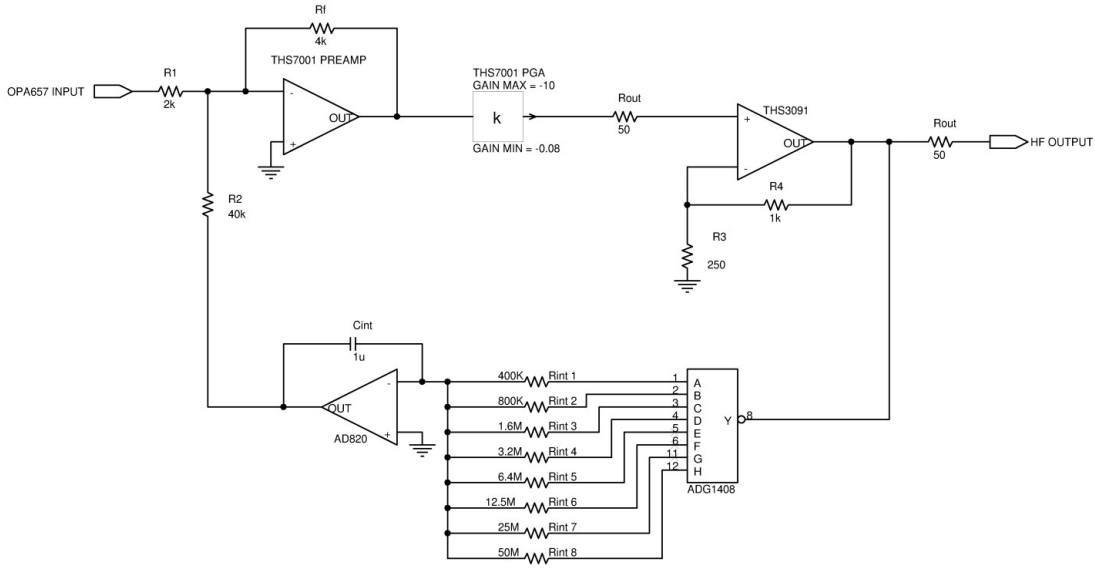


Figure 3.5: Programmable Gain Amplifier, output stage and integrator feedback loop

3.2.3 Integrator feedback loop

The total output offset, caused by the different amplifier of second stage, is eliminated by an additional feedback loop containing an integrator as shown in figure 3.5; this circuit synthesizes, with active components, the transfer function of an equivalent high-pass passive CR filter placed at the output, which is not feasible, due to the low output impedance of 50Ω due to the terminated transmission line.

The loop gain and ideal gain of the integrator stand-alone is

$$G_{loop_{int}} = -\frac{R}{R + \frac{1}{SC}} A_0 = \frac{A_0 R}{\frac{1+SCR}{SC}} = -A_0 R \frac{SCR}{1 + SCR} \quad (3.1)$$

$$G_{ideal_{int}} = -\frac{1}{SCR} \quad (3.2)$$

Therefore the real gain of the integrator stand-alone is

$$G_{real_{int}} = \frac{1}{1 + SCR(1 + A_0)} \cong \frac{1}{1 + SCRA_0} \quad (3.3)$$

Using it to calculate the loop-gain of the entire stage

$$G_{loop} = G_{real_{int}} [G_{preamp}] [G_{PGA}] [G_{outputstage}] = G_{real_{int}} [G_{andata}] \quad (3.4)$$

This can be used to calculate the real gain of the entire stage

$$G_{real} = \frac{G_{andata}}{1 - G_{loop}} = \frac{G_{andata}}{1 - G_{real} G_{andata}} \quad (3.5)$$

$$(3.6)$$

$$G_{real} \cong \frac{G_{andata}(1 + SCRA_0)}{G_{andata} + SCRA_0} \quad (3.7)$$

$$(3.8)$$

The transfer function has two singularity: a zero and a pole. To maintain constant the pole frequency at $16mHz$, the resistor R is selectable by an analog multiplexer, the ADG1409, as show in figure 3.5 In the table 3.1 there are correspondences between the PGA gain and the selected resistor.

$$f_{pole} = \frac{1}{2\pi(CR\frac{A_0}{G_{andata}})} \quad (3.9)$$

PGA Gain	Resistor
0.08	$400k\Omega$
0.16	$800k\Omega$
0.32	$1.6M\Omega$
0.63	$3.2M\Omega$
1.26	$6.4M\Omega$
2.52	$12.5M\Omega$
5.01	$25M\Omega$
10.0	$50M\Omega$

Table 3.1: Correspondences between PGA selected gain and integrator feedback loop resistor

For the active integrator the choise was the analog devices AD820, an opamp with the important features of low offset voltage and low bias current: the residual output offset is the sum of the offset of operational amplifiers used for the integrator and the potential drop on resistance R due to the current bias of the same opamp.

The choice of the resistor consequently set the value of zero's frequency, which then changes depending on the selected pga gain. Due to the high value of $A_0 \cong 150000$ the zero is well below the pole, and everything it's ok.

$$\begin{aligned} f_{zero,min} &\cong 22nHz \\ f_{zero,max} &\cong 2.65\mu HZ \end{aligned} \quad (3.10)$$

3.2.4 Anti aliasing filter

The need of a low-pass anti-aliasing filter coming from the limited performance of the acquisition board and the computer. At high frequency the limit is the shannon theorem which impose a minimun sampling frequency to acquire the signal without aliasing artifacts; at low frequency the limit for an useful measure is the time required to acquire at least, ideally, two samples per period. These two requirements can not be fulfilled simultaneously due to limited memory of the acquisition board: at $100MS/s$ the adc board memory, $32MByte$ for each channel, are filled after $\cong 183mS$, giving a minimum teoretical detectable frequency of $\cong 5.46Hz$. To solve this problem was decided to place an analog anti-aliasing filter at the end of the channel amplifier, which allow the use of a lower sampling frequency and consequently longer acquisition time, making possible to measure the input signal in to the milliHertz range. Another benefit of the low pass filter is the speed-up of data elaboration when a high frequency dut characterization is not needed: here must be remarked thath, with the maximum sampling rate of $100MS/s$ and available processing power, the elaboration is about hundred times longer than the sole acquisition time. With the low pass filters enabled the

sampling rate can be reduced at 100kS/s and the elaboration time becomes negligible: this means that the total measurement time is reduced to one-hundredth of the value at 100MS/s or, dually, that the same total duration at 100MS/s correspond now entirely of acquisition time, allowing a decrease of uncorrelated noise and better sensitivity.

The structure of the filter is shown in figure 3.6

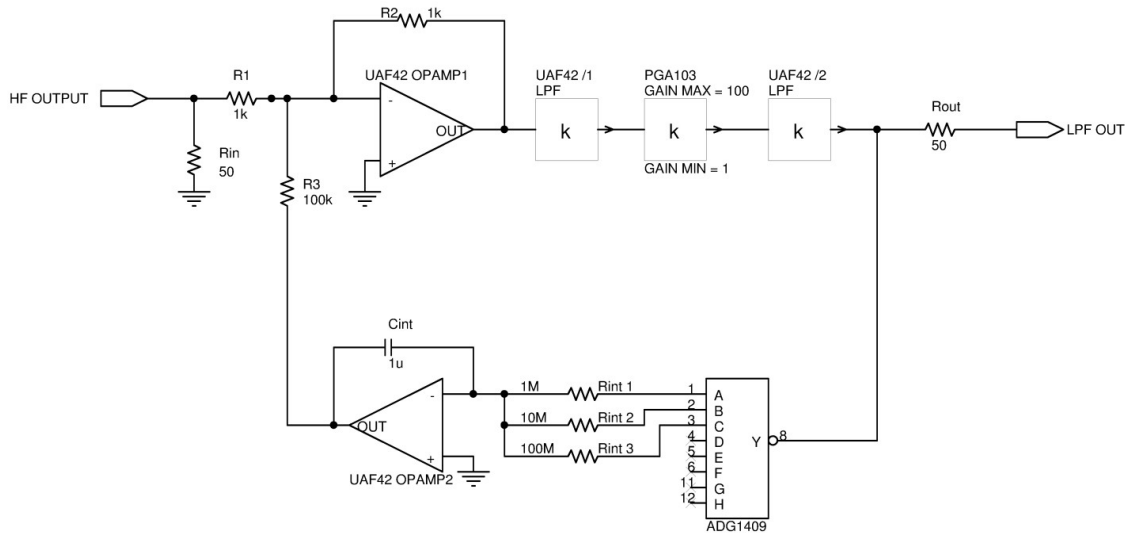


Figure 3.6: Low Pass filter stage: the two operational amplifiers and biquadratic cells low pass filters are integrated on the same device

Overall is a fourth order Butterworth 5kHz low-pass filter which have the flattest possible passband response. It was chosen the fourth order because higher order filters have a too high sensitivity to the components used that makes difficult to construct two filters with the same phase characteristics (as shown in paragraph 1.3 the phase difference between the two channels lead to a reduction in the useful signal output after the cross-correlation operation). The filter is splitted in two bi-quadratic cell with an additional optional gain stage placed between them, made by a single chip programmable gain amplifier PGA013; a double relay at the input allow to engage or disengage the anti-aliasing filter from the signal path. Each bi-quadratic cell is made with a Texas Instruments UAF42, a monolithic chip that include inverting amplifiers and integrators that can be configured for a wide range of low-pass, band-pass and high-pass filters; the two filtering stage was designed by the specific cad design program for the UAF42. In the UAF42 there is also another unconnected opamp with GBWP of 4Mhz for any other general purpose use. These two amplifier, one for each chip, are used in conjunction with the analog multiplexer ADG1409 to make an integrator placed in feedback loop around the filter stage. This circuit synthesizes, with active components, the transfer function of an equivalent high-pass passive filter CR at the output of the filters stage, to strongly attenuate the output DC offset generated by the anti-aliasing circuit itself, emphasized when the additional gain is setted to 10 or 100. It is exactly the same circuit topology used for the integrator loop around the programmable output amplifier and output stage. The residual DC output is due only to the dc offset of the operational amplifier used for the integrator and the voltage drop on the integrator's resistor R due to the input current bias of the same opamp. Since the operational amplifier integrated in the UAF42 have an offset voltage of $0.5mV$ and a input bias current of $10pA$ the maximum DC residual offset voltage of the anti-aliasing filter stage is only $1.5mV$

The 50Ω impedance matching at the input allows the output amplifier (THS3091) to work always in the same output load condition, regardless of whether the filters are engaged or disengaged, to avoid any static gain error. At this low frequency (few kHz) the impedential matching between the source and the cable is not required so the acquisition board input is configured by software at high impedance when the anti-aliasing filters are active: this avoid the use of an additional high current output buffer placed after the second UAF42 filter stage; to improve the stability of this last UAF42 a 50Ω resistor is placed at its output to isolate it from the coaxial cable capacity.

3.3 Noise generator

As stated in the relative chapters, some front-ends are able to perform some kind of characterization on the DUT; typically is very useful to have a transconductance g_m measure since it often appears in the equations that define the dut noise. The easiest way to measure the g_m with a spectrum analyser is by driving the gate (or other dut's input terminal) with a wide spectrum noise covering all the frequencies of interest: by calculating the ratio between the DFT of DUT's output current and the drive signal is possible to obtain, with a single measure, the DUT transconductance over the full instrument bandwidth. Typically all kind of microelectronic devices show a $1/f$ noise spectra superimposed over a white noise level. To make a good g_m measure over the entire frequency range without saturation is useful to have a noise generator capable of generate a $1/f$ noise superimposed over a white noise level. It was therefore decided to integrate a noise generator on the mainboard, able to generate configurable levels of white and $1/f$ noises. In figure 3.7 is shown a high level diagram of all circuit block of the noise generator section.

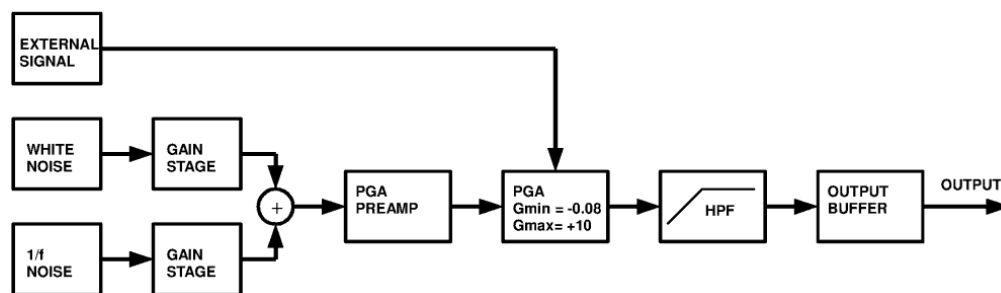


Figure 3.7: Noise generator circuits overview

To obtain the white noise the basic idea is to simply amplify the voltage noise generated by a resistor: in fact due to the limit of operational amplifiers it's impossible to obtain a flat noise generator over the entire useful bandwidth (16mHz, +40MHz) of the analyser with only a resistor and an opamp; the solution is to split the generator in three different bands and join them together; figure 3.8 shown the block diagram of this solution.

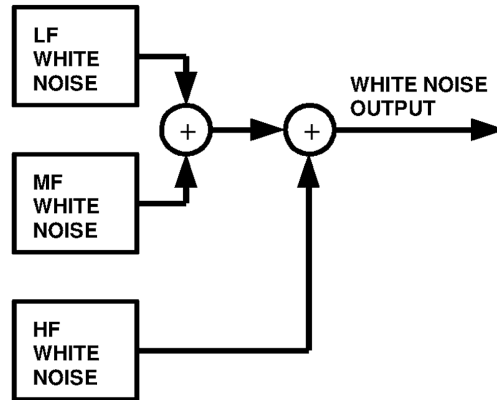


Figure 3.8: White Noise Generator block diagram.

The first two subsection are made around an OPA124, a precision difet operational amplifier chosen for its very low input current noise and corner frequency, to obtain a noise level dominated by the accurate value of the input resistor. The first subsection generate noise up to 10Hz, the second up to 10kHz. The third section is make around an OPA657 and contributes to the output noise from 10kHz and above; then they are joined by the CR-RC filter between them. Complete circuit is shown in figure 3.9

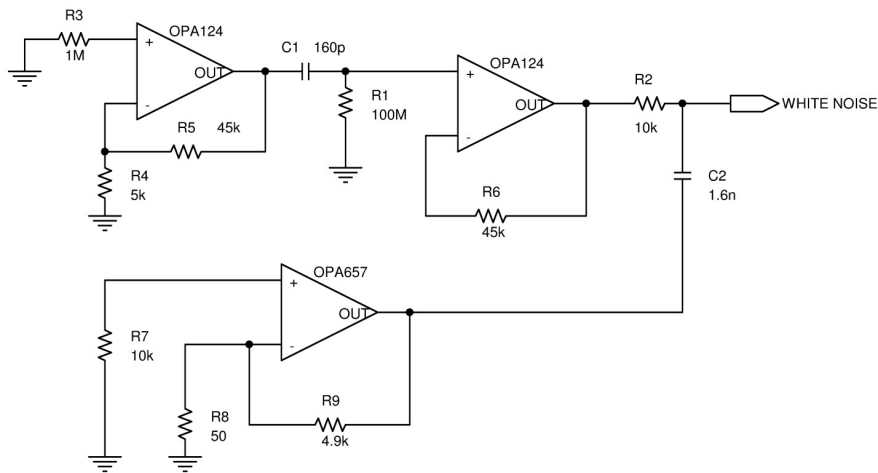


Figure 3.9: White Noise Generator complete circuit

Obviously this is a simplified analysis of the circuit which can not generate a *true white* noise; resistor tolerance, different temperature between them, noise generated by operational amplifier and feedback network: all this side effect contribute and change the ideal white output spectrum, but for the purpose of the generator this is not a problem. Since the transconductance is obtained as the ratio between dut's output current and noise generator signal, this one does not need to be *true white* but only relatively constant over the useful instrument's bandwidth.

To give maximum flexibility the $1/f$ spectra is generated by a selectable device: there is a place on the motherboard to plug a discrete n-channel mosfet, whose V_{gs} , and therefore its noise level, are adjustable by a digital controlled trimmer.

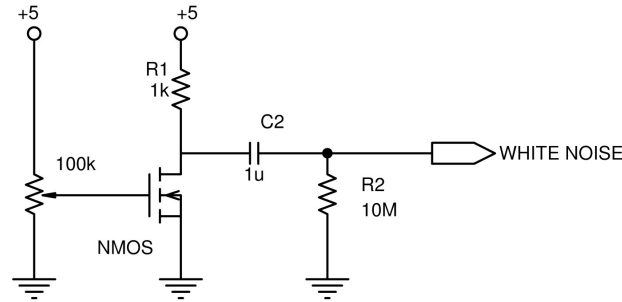


Figure 3.10: $1/f$ noise generator: the nmMos device is not soldered on the board, but there is a socket where a discrete device can be inserted. The trimmer that select the V_{gain} is digitally controlled by the control software

White and $1/f$ noises are then amplified by a factor of 10 by two opamp in a simple non-inverting gain configuration. For this role the choice is the ADA4817, an integrated circuit composed by two opamp whit GBWP of 1050MHz in the same package. The presence of an independent power-down pin for each amplifier allows to choose the noise source: only white noise, only $1/f$ noise, both together or no noise at all.

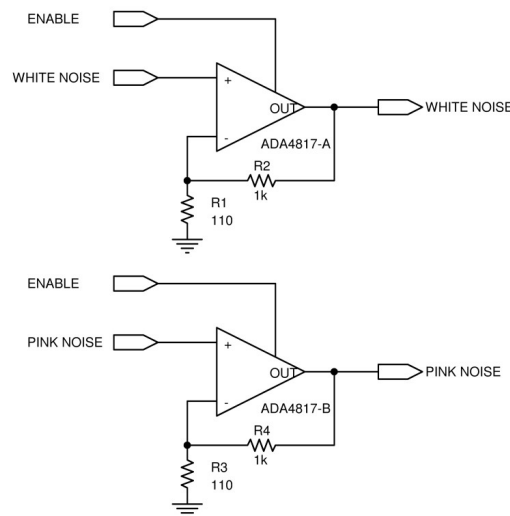


Figure 3.11: Independently gain stages for white noise and $1/f$ noise

After the white and $1/f$ gain stages there is a programmable gain amplifier, the same THS7001 used in the signal channels, consisting of an operational pre-amplifier and a programmable gain amplifier with gain ranging from -20db to +20db. The pre-amplifier is in a non-inverting configuration and perform the sum of white and $1/f$ noises, then the pga perform further amplification or attenuation of the noise level. An additional relay at the input of pga allows to connect (and amplify/attenuate) an external generator instead of the internal one. After the pga a 16mHz RC high-pass-filter remove the dc component generated by offsets and bias currents of all previous stages. Finally a buffer drive the output line to the front-end and the adc acquisition board.

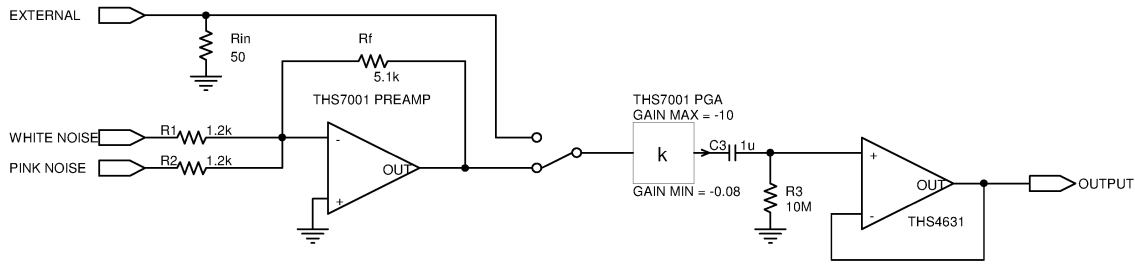


Figure 3.12: Programmable gain amplifier, high pass filter and output stage of the noise generator. The relay give the opportunity to connect an external generator

3.4 Power Supply

To separate as much as possible the two channels, and thus to obtain a low crosstalk between them, each one have its own power supply circuit. This section provide all the necessary voltage to the mainboard amplifier and to the frond-end. Each channel need four stabilized voltage to operate properly, $\pm 15V$ and $\pm 5V$. The $\pm 15V$ regulators works with external input ranging from $\pm 18V$ to $\pm 35V$, provided by an external laboratory power supply unit or lead-acid battery. The $\pm 5V$ regulators take the regulated $\pm 15V$ as inputs. The extremely high sensibility of the instrument prevent the use of high-efficiency switching regulator which typically create a lot of electromagnetic noise at the switching frequency and at the higher harmonics. Therefore each power supply line is made around a linear fixed voltage regulator of the LM7xxx series; they have built in current limits, thermal shut-down and safe area protection, making them very robust and easy to use. In the chosen D^2PAK package they can deliver over $1A$ of output current, much more than necessary to the second stage, to avoids creating a limit for future developments of more complex front-ends.

In addition there are four additional supply line, again $\pm 15V$ and $\pm 5V$, to power the noise generator on the mainboard and some auxiliary circuitry present on each front-end board, for example temperature sensor, magnetic field generator, bias circuitry for devices with substrate / bulk contact, etc... They are make with the same topology of the signal's channel's power supply circuit, the only difference is the choice of LM7xxx regulator in the much smaller $DPAK$ package, capable of only $500mA$ of continuous DC output current, more than adequate for the need of the noise generator and auxiliary circuitry.

3.5 Physical design and layout

The mainboard is made on a standard four layer pcb, 1.6mm overall thickness, 35μm copper thickness. Top layer are dedicated to analog signals and digital control signal run almost only on the bottom layer; the two inner layers are reserved to power supply signal and ground plane, respectively. The populated mainboard is visible in figure 3.13 with the various sub-circuits and connectors highlighted.

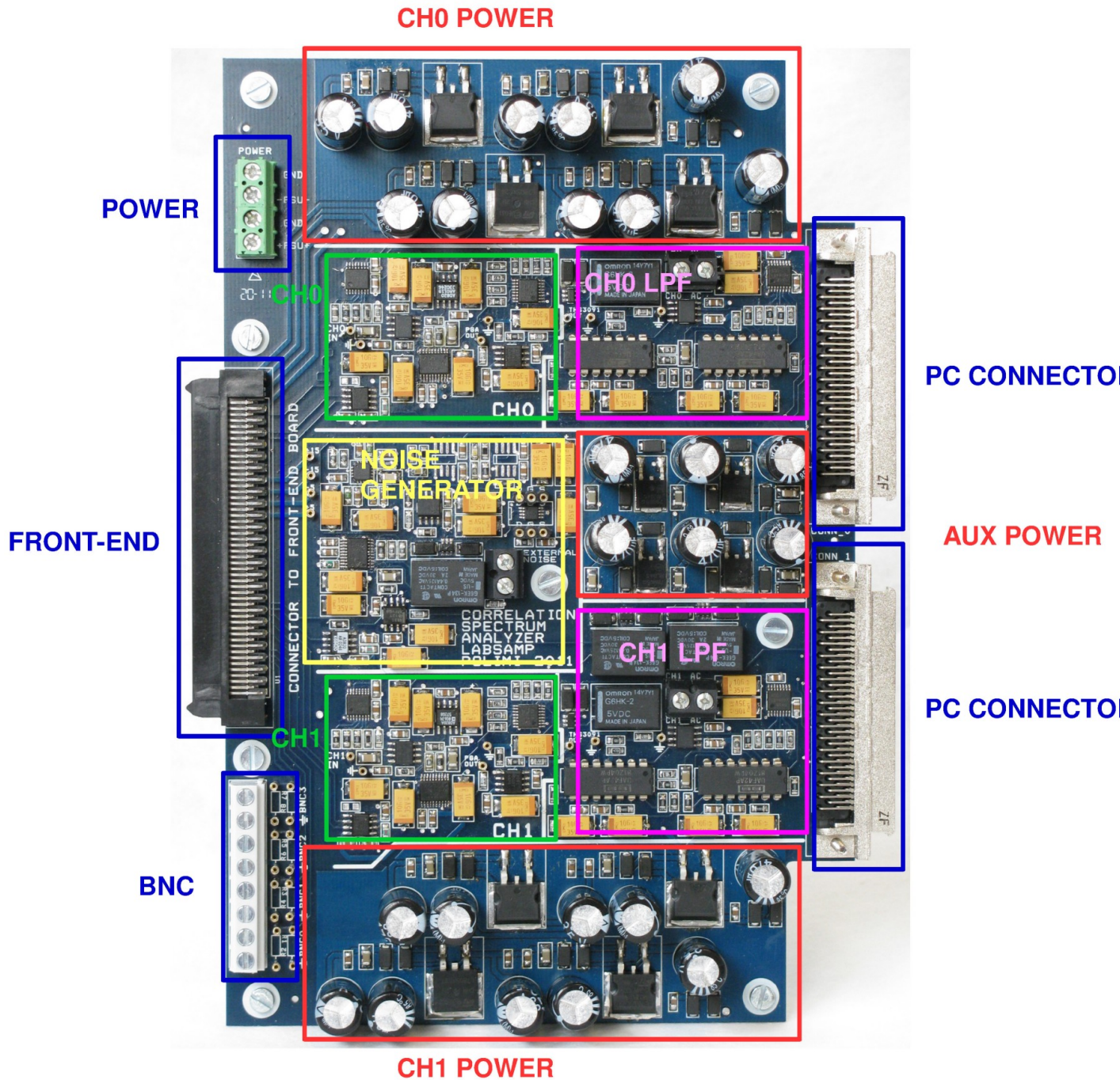


Figure 3.13: Image of the populated mainboard with highlighted main function blocks and connections

Chapter 4

Current sensitive front-end

The front-end described in this chapter is an ideal prosecution of previous works already done on cross-correlation based instruments [1], [2], [7]

It is a current-mode front-end designed to measure integrated semiconductor devices based on MOS structure that operate above the threshold gate voltage in saturation zone: this kind of devices have high drain-source and gate impedance, relatively high channel bias current (up to the mA range), and their noise are often dominated by the $1/f$ component; the goal of characterization is to reach the corner frequency of the $1/f$ noise, measure the white noise where it becomes prevalent and compare the value with that predicted by the semiconductor device model. It is also required to take the transconductance measure at the same bias condition of noise measure, to calculate the equivalent noise sources at the input of the DUT. Considering all this requirements, following the various trade-off described in the general analysis of the current-mode front-end (section 1.4) this circuit was designed with a relatively small feedback resistor to handle bias current up to 1mA and reach at least 10MHz of useful bandwidth. The bias network are able to perform g_m measure from both gate and source terminal, and moreover is possible to measure the drain-gate early resistance.

4.0.1 Design of the front-end stage

The feedback resistor R_F of the scheme in the figure 4.1 limits the current dynamic of the instrument: in this resistor flows the ac signal and the DUT dc bias current, so the value of this resistor can not be too high to avoid saturation of the transimpedance stage

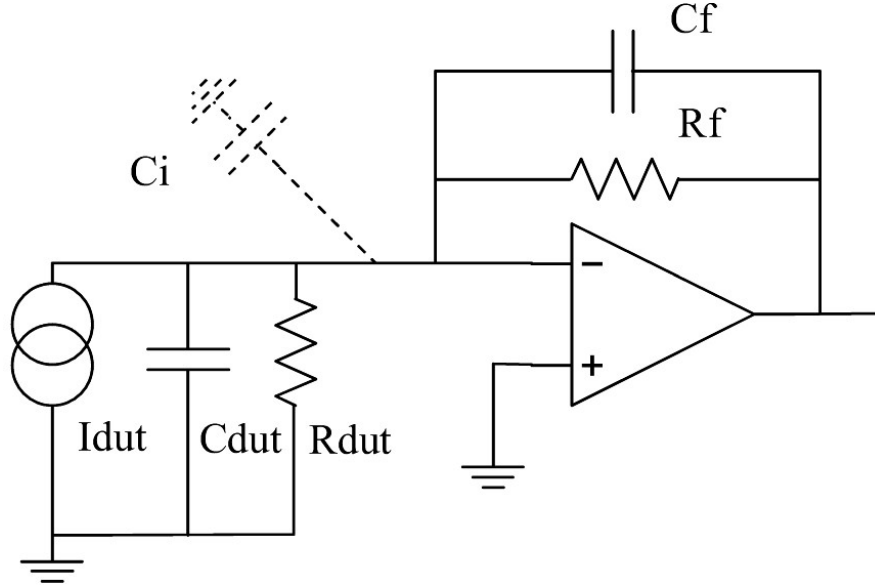


Figure 4.1: Basic transimpedance gain stage

Imposing the limits of $750\mu A$ for the bias current and $5V$ for the drain/source voltage bias (given with the virtual ground), R_F has been chosen with the equation:

$$|V_{rif}| + |I_{dut}|R_F < V_{out_{max}}$$

$$R_F \leq \frac{V_{out_{max}} - |V_{rif}|}{|I_{dut}|} \cong \frac{12.5V - |5V|}{|I_{dut}|} = 10k\Omega \quad (4.1)$$

The choice of R_F value is a critical aspect because it determines the maximum output current, the bandwidth and the total input current noise: an high value reduce the uncorrelated equivalent input noise but decrease the bandwidth and the output current, while a low value increase both bandwidth and current at the cost of increased uncorrelated noise.

The choice of R_F value, limits on maximum output swing and common mode input voltage, required bandwidth ($GBWP \gg 10MHz$), input current noise $\leq 1pA/\sqrt{Hz}$, voltage noise as low as possible and the needing of low bias current¹ $\ll 30\mu A$ have led to the choice of operational amplifier THS4021 by Texas Instruments which most significant parameters are shown in table 4.1.

To make the amplifier stable with phase margin $\Phi_m \geq 50$ with $C_i \approx 5pF$ the passive network shown in figure 4.2 has been added at the output of the amplifier.

The network, where all elements are dependent and interacting with each other was designed to have $C_1, C_2 \gg C_f, C_d^*$ with $C_d^* = C_{dut} + C_i$, so the reactive elements can be considered non-interacting in pairs. The compensated partition reduces the G_{loop} while the two resistors R_0 and R_x compensates the phase loss due to the finite output resistance of the opamp. In figure 4.3 is shown the feedback loop at low and high frequency.

¹To permit an accurate reading of I_{DUT} down to about $30\mu A$

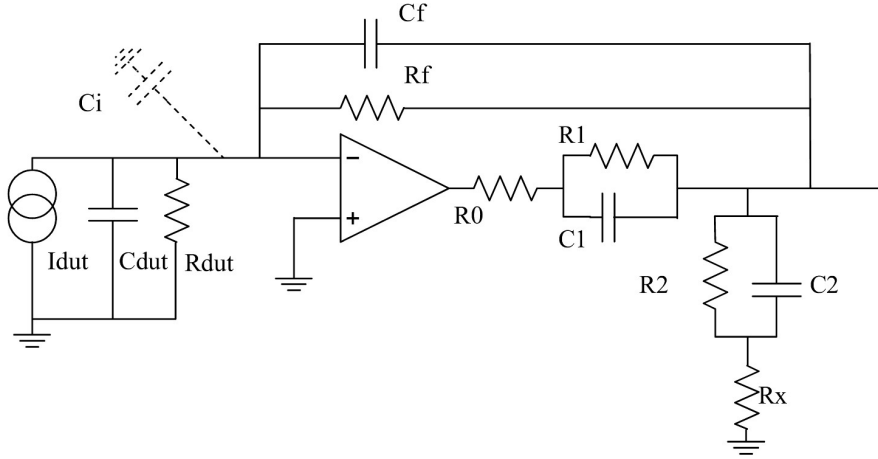


Figure 4.2: Designed transimpedance stage with complete feedback network

At low frequency, with $(R_x + R_0) \ll (R_1, R_2, R_f, R_{dut})$ and $R_1 \ll (R_f + R_{dut})$, there are two independent poles and two independent zeros.

$$\begin{aligned}
 f_{z,1} &= \frac{1}{2\pi(R_1 C_1)} \\
 f_{z,2} &= \frac{1}{2\pi(R_x C_2)} \\
 f_{p,1} &= \frac{1}{2\pi R_1 (C_1 + C_2)} \\
 f_{p,2} &= \frac{1}{2\pi(R_0 + R_x)(C_1 || C_2)}
 \end{aligned} \tag{4.2}$$

Imposing $f_{z,2} = f_{p,2}$ and an attenuation of 3 of G_{loop} by imposing $f_{z,1} = 3f_{p,1}$ (that is $C_2 = 2C_1$) the components values are: $R_0 = 50\Omega$, $R_x = 25\Omega$, $R_1 = 1k\Omega$, $R_2 = 100k\Omega$, $R_f = 10k\Omega$, $C_1 = 10nF$, $C_2 = 20nF$

Parameter	Condition	Typical value
Input voltage noise	$f > 10kHz$	$1.5nV/\sqrt{Hz}$
Input current noise	$f > 10kHz$	$2pA/\sqrt{Hz}$
Input impedance	$V_S = \pm 15V$	$1M\Omega 1.5pF$
Input offset voltage	$+25^\circ C$	$\pm 0.5mA$
Input voltage range	$V_S = \pm 15V$	$\pm 14.3V$
Voltage Output	$V_S = \pm 15V$	$\pm 15V$
GBWP	$G = 10$	$350MHz$

Table 4.1: Most significant parameters of THS4021 operational amplifier.

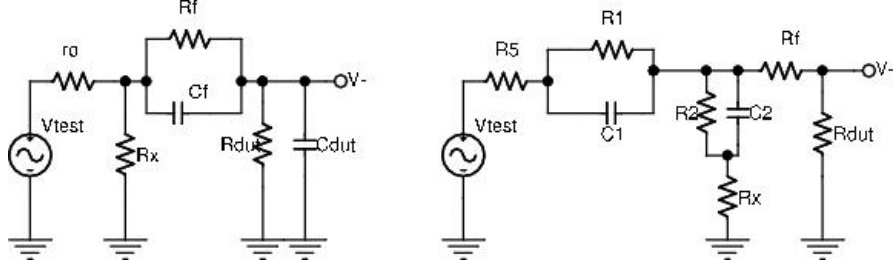


Figure 4.3: Feedback network at high(sx) and low(dx) frequencies

At high frequency there are other two poles and one zero:

$$\begin{aligned}
 f_{z,3} &= \frac{1}{2\pi(R_f C_f)} \\
 f_{p,3} &= \frac{1}{2\pi(R_f || R_{dut})(C_{dut} + C_f)} \\
 f_{p,4} &= \frac{1}{2\pi(R_0 || R_x)(C_{dut} || C_f)}
 \end{aligned} \tag{4.3}$$

All the poles and zeros of the G_{loop} are reported in the table with a $R_{dut} = 15k\Omega$.

Singularity	Value
$f_{p,1}$	$5.3kHz$
$f_{z,1}$	$16kHz$
$f_{p,1_{opamp}}$	$30kHz$
$f_{p,2} = f_{z,2}$	$318kHz$
$p,3e$	$4.6MHz$
$f_{z,3}$	$22.7MHz$
$f_{p,2_{opamp}}$	$168.7MHz$
$f_{p,4}$	$13.6GHz$

Table 4.2: Loop gain poles and zeros.

In conclusion the transimpedance amplifier is stable (phase margin $\phi_m \leq 50^\circ$) with a $R_{dut} = 15k\Omega$ and typical capacity of $C_{dut} = 100fF$. The stability is guaranteed for any DUT characterized by a resistance $R_{dut} \geq 500\Omega$ and a parasitic capacity negligible compared to $5pF$ estimated for the dut front-end connection. The feedback network introduces an additional equivalent input noise of $0.4pA/\sqrt{Hz}$, negligible compared to $2.4pA/\sqrt{Hz}$ given by the amplifiers and the feedback resistor R_f .

4.0.2 Drain and source bias network

The transimpedance topology of the front-end makes very easy to bias the DUT terminals, thanks to the fact that the negative input of the operational amplifier, and therefore the dut's terminal, is a virtual ground: its voltage DC value is the same applied to the positive input terminal, with only a small error due to non-infinite open loop gain A_0 of the operational amplifier.

$$\varepsilon = \left| \frac{G_{real} - G_{ideal}}{G_{real}} \right| = \left| \frac{1}{G_{lopp}(0)} \right| \quad (4.4)$$

The virtual ground effect requires a clean voltage reference to work properly: every signal present at the opamp's positive input is reflected at the dut's terminal, not only the dc value. In fact a noise at this terminal is in series with the input equivalent voltage noise of the opamp itself, and have consequently the same effect on correlated and uncorrelated noise as summarized in equation 1.20 and 1.21

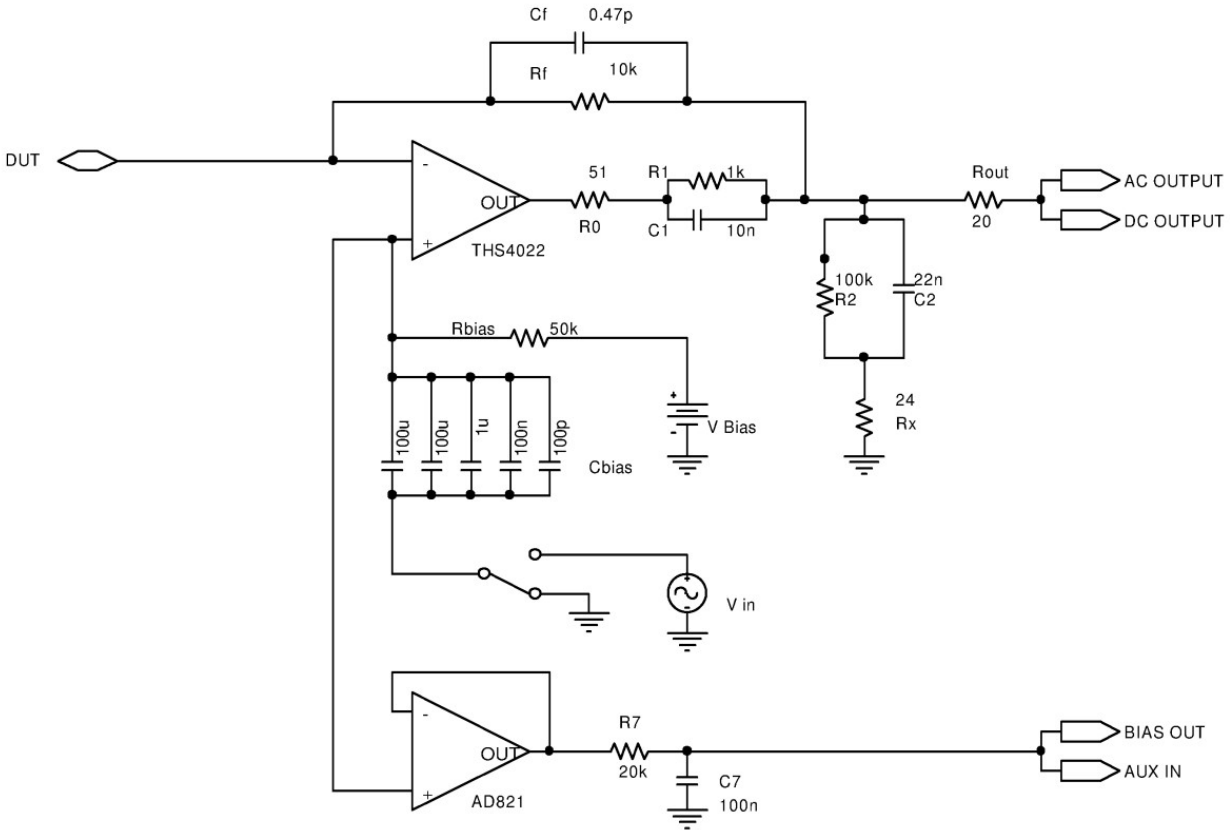


Figure 4.4: Transimpedance amplifier with bias circuitry

To minimize this problem the voltage reference, coming from the DAC of the national-instrument control board, pass through a low pass filter made by R_{bias} and 5 capacitor, valued $100\mu F$, $1\mu F$ and $100pF$ placed in parallel. The filter low pass cut frequency is then $16mHz$. The drawback of this solution is the voltage drop across the filter resistor R_{bias} , due to the THS4021 input bias current of $6\mu A$, which causes a uncertainty of $300mV$ on the voltage at the input pin. Decreasing this offset by lowering the resistor value is not a solution, because should correspondingly increase too much the value of the capacitor. The solution is to read

the value present at the non inverting input of transimpedance amplifier and consequently drive the voltage source. Its in fact a closed control loop on the bias value made by the adc, dac and pc software. It is possible to drive the DUT's terminal with useful signal by connecting a voltage source V_{in} at the capacitor's input of the RC filter, that act at the same time as an high-pass filter for the input signal and as a low-pass for the DC bias. This feature make possible to measure the DUT's g_m and R_0 , as will be shown later. The V_{in} come from the internal noise generator. This option is present only in the source's channel. The complete transimpedance circuit at both channels is shown in figure 4.4

4.0.3 Gate bias network

The gate bias network is designed to make possible to measure the correlated signal generated by the DUT (it own noise), its transconductance g_m from gate or source terminal, and the R_0 (the early resistor for a mosfet in saturation zone). This is achieved by the use of relè to reconfigure the circuit topology for a specific measure. In figure 4.5 is shown the overall front-end circuit, with all relay and passive components. In the subsequent sections of the text each configuration will be described simplifying this schematic to highlight only the relevant parts.

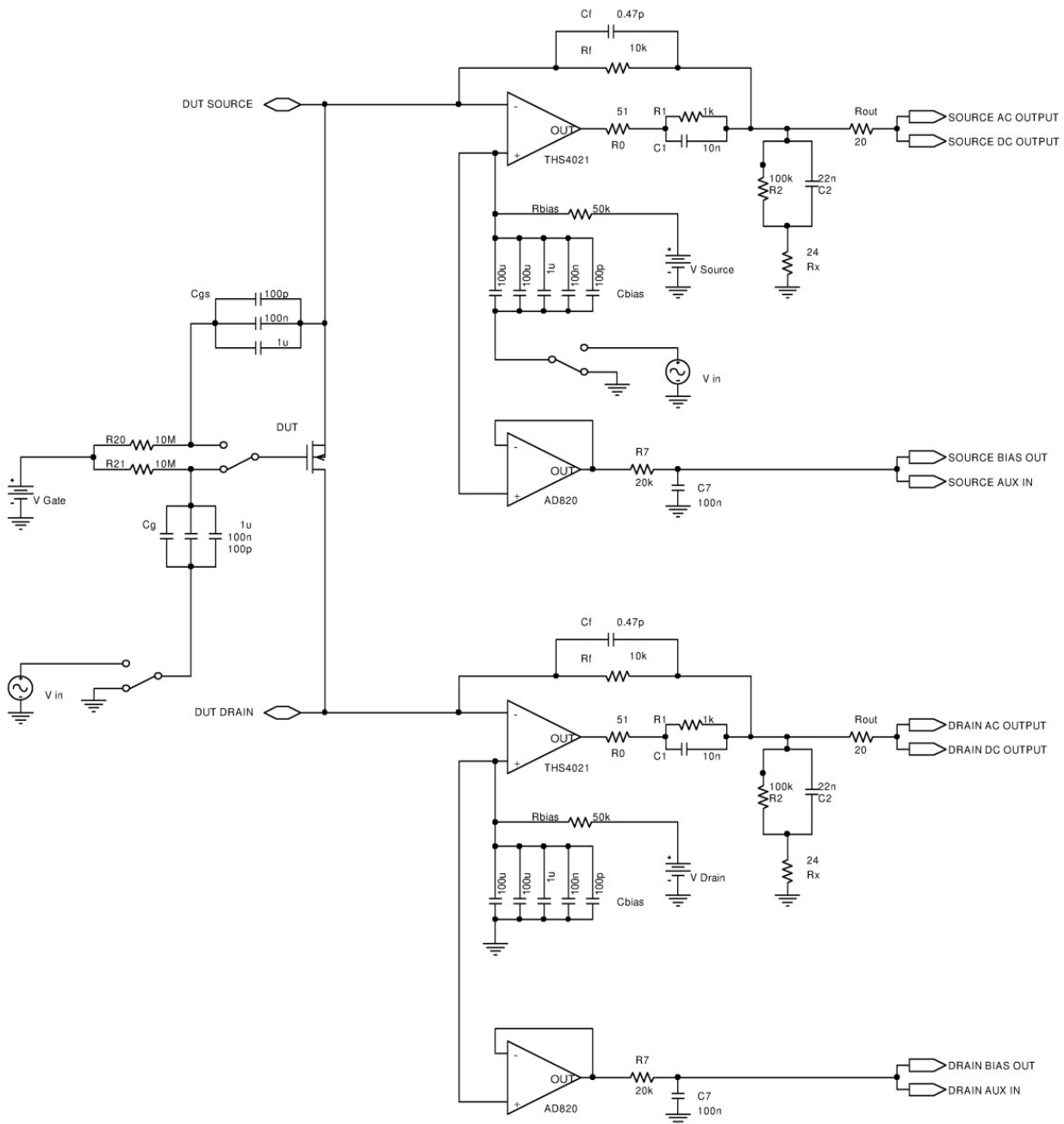


Figure 4.5: Complete current-sensitive front-end circuit

Cross-Correlation configuration

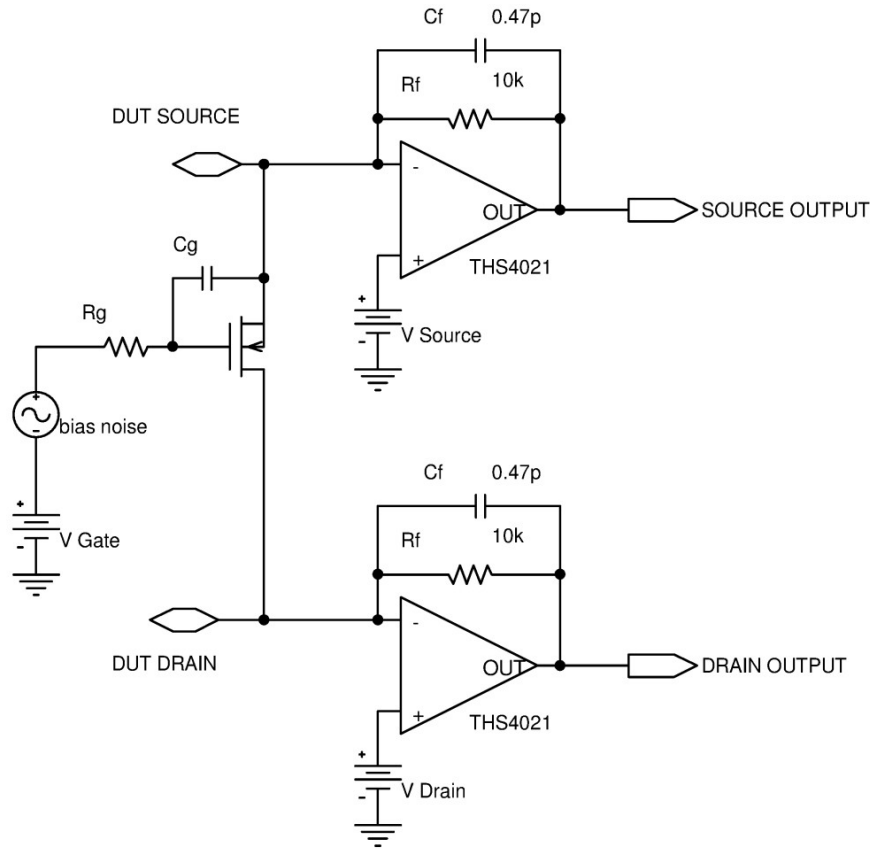


Figure 4.6: Current-sensitive front-end: cross-correlation configuration

This is the configuration for measure only the noise coming from the dut itself: only the DC bias value are present at the non-inverting inputs of the transimpedance amplifiers, and consequently at the dut's source and drain terminals. The signal generator is turned off and disconnected from both the source and gate bias networks. The DC generator for gate bias is made by the NI DAC output and has inevitably its own noise which, if the generator was put directly at the gate, would drive the transistor producing an unwanted correlated signal that would cover the current noise of the dut; therefore the DC gate bias generator must be filtered to attenuate this effect. The easiest solution is to place a low pass-filter between the generator and the dut's gate. The circuit is shown in figure 4.7: transimpedance loops and active bias circuit at the non inverting inputs have been simplified to enhance focus on the gate network. C_g and R_{20} are the low pass filter, C_{gs} is the dut's gate-source capacitance. This circuit effectively filter the noise of the dc generator starting from 16mHz due to $R_{bias} = 10M\Omega$ and $C_{filter} = 1\mu F$, but has a major flaw: is formally the current-mode front-end showed in figure 1.3 and are therefore valid all the considerations made in the relative chapter; the main difference between the two circuits is the dut, which is a transistor and not a simple bipole. In the equations 1.20 and 1.21 the impedance Z_D (eq 1.22), and thus the dut's resistance R_D , plays a critical role in determining the amount of correlated and uncorrelated noise: it is therefore essential to maximize the dut's impedance from both the drain and source terminal. In this circuit the two resistance are $R_d \cong R_{0,dut}$ seen from the drain and $R_s = 1/gm$ seen from the source. While $R_{0,dut}$ is the maximum obtainable from a single mosfet transistor, the $R_s = 1/gm$ is completely inadequate: it depend by the dut's polarization and can reach a so low

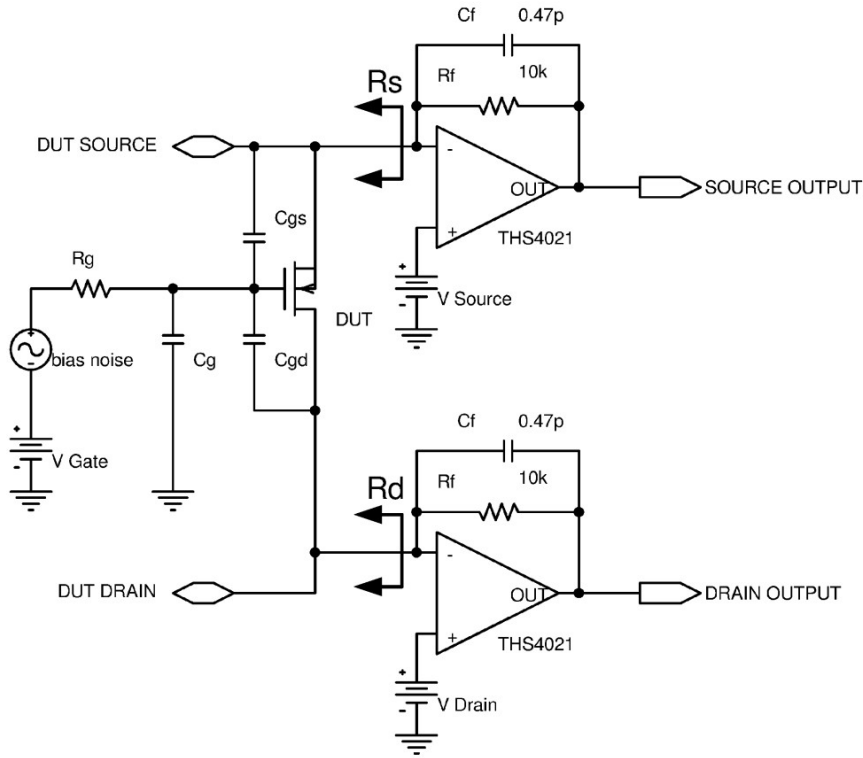


Figure 4.7: Current-sensitive front-end: wrong V_{gs} bias circuit

value that makes a enormous quantity of correlated and uncorrelated noises. The solution is shown in figure 4.8 Filter capacitor C_{filter} is placed between gate and source, in parallel to dut's C_{gs} . This change completely the impedance seen from the source transimpedance, while $R_d \cong R_{0,dut}$ remain unchanged.

This network split the dut impedance in two different component, one as dut impedance between channels and another impedance only on source channel in parallel whit cp of figure 4.2

Since $C_{filter} \gg C_{gd}$, Z_{dut} can be calculated in the following manner. At medium frequency, from 16mHz up to the intervention of C_{gd}

$$V_g = V_s \frac{R_{filter}}{R_{filter} + \frac{1}{SC_{filter}}} = \frac{SC_{filter}R_{filter}}{1 + SC_{filter}R_{filter}} \quad (4.5)$$

and therefore

$$i_{mos} = (V_{in} - V_g)gm = V_{in} \frac{gm}{1 + SC_{filter}R_{filter}} \quad (4.6)$$

from which it follows that

$$Z_{mos} = \frac{V_{in}}{i_{mos}} = \frac{1 + SC_{filter}R_{filter}}{gm} \quad (4.7)$$

The mosfet impedance have a zero at $1/2\pi C_{filter}R_{filter}$ and is valued $1/gm$ at lower frequencies. At frequencies much greater than the zero the C_{filter} capacitor can be considered completely closed, so the circuit can be simplified, as shown in figure in fact the dut's impedance between channel can be seen as a sum of three contribute: mosfet, r_0 , C_{gd}

There are also the two impedance between source and ground, drain and ground, made by R_{filter} and C_{filter} and C_{gd} . The possible drawback of this solution is the injection, due to C_{filter} , R_{filter} and C_{gd} , of correlated noise generated by the noisy gate bias generator and R_{filter} itself noise.

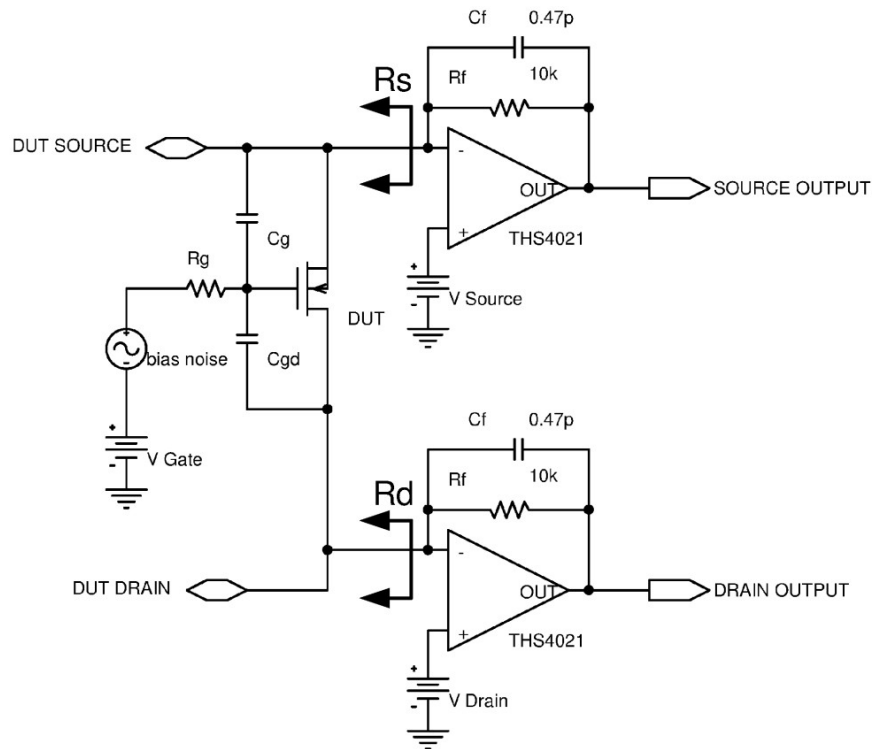


Figure 4.8: Current-sensitive front-end: correct V_{gs} bias circuit

Transconductance measure from gate input

This configuration is used to measure the dut's transconductance obtained as

$$g_m = \frac{I_{DUT}}{V_{in}} = \frac{V_{drain,output}}{gain \cdot V_{gate}} \quad (4.8)$$

where $gain$ is the global instrument gain from dut's drain current to the adc input. In this configuration the C_{gate} filter capacitor is detached from the source input and connected to the signal generator: the circuit made by C_{gate} and R_{gate} act as a low-pass filter for gate bias generator, to attenuate itself noise, and as a high-pass filter for the signal generator, to eliminate its DC offset which would change the V_{gate} bias. The circuit is the same of the figure 4.7 so the impedance from source transimpedance input is low as $1/g_m$, causing a lot of uncorrelated noise in source channel and correlated noise; these are problems for a cross-correlation configuration but can be ignored for the g_m measure since the dut's drain current is generated by the gate input signal and therefore can be orders of magnitude larger than that due to the operational amplifier input equivalent voltage noise source. In fact the front-end work as a traditional single channel analyser, forcing the dut's gate with an input signal and measuring the drain output current; the output of the source channel is ignored and its function is only to maintain the correct V_{source} bias voltage.

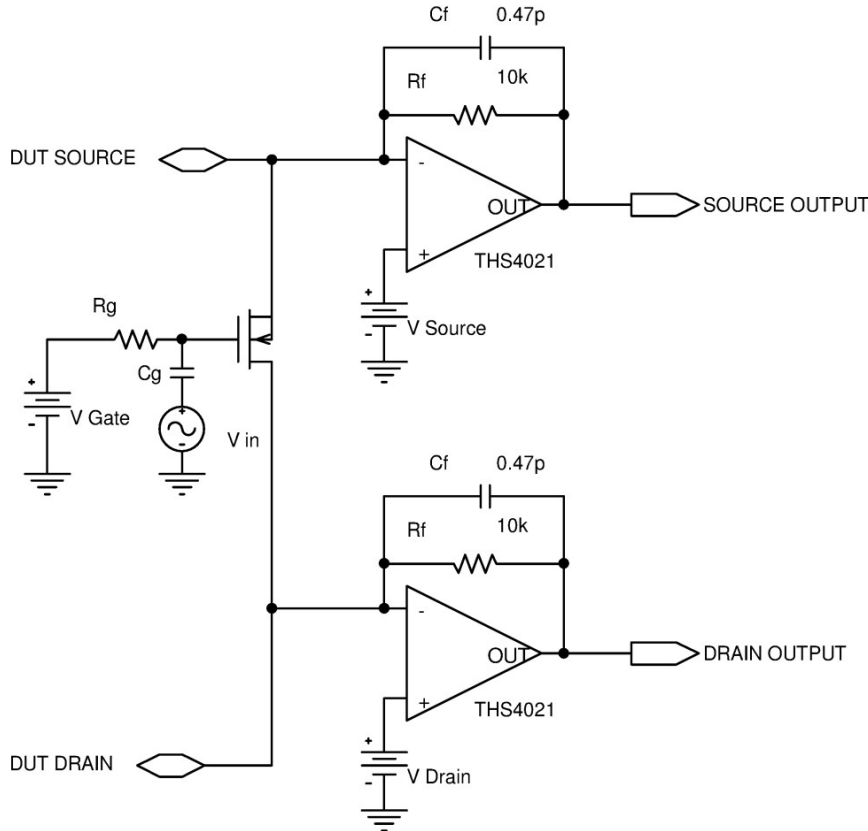


Figure 4.9: Current-sensitive front-end configured for DUT's g_m measure by injecting input signal at the gate terminal

Transconductance measure from source input

This configuration is essentially identical to the previous, the only difference is the input signal generator, which is injected in the dut's source terminal instead of the gate, as showed in paragraph 4.0.2 Thus the transconductance can be calculated as

$$g_m = \frac{I_{DUT}}{V_{in}} = \frac{V_{drain,output}}{gain \cdot V_{source}} \quad (4.9)$$

where *gain* is the global gain from dut's drain current to the adc input.

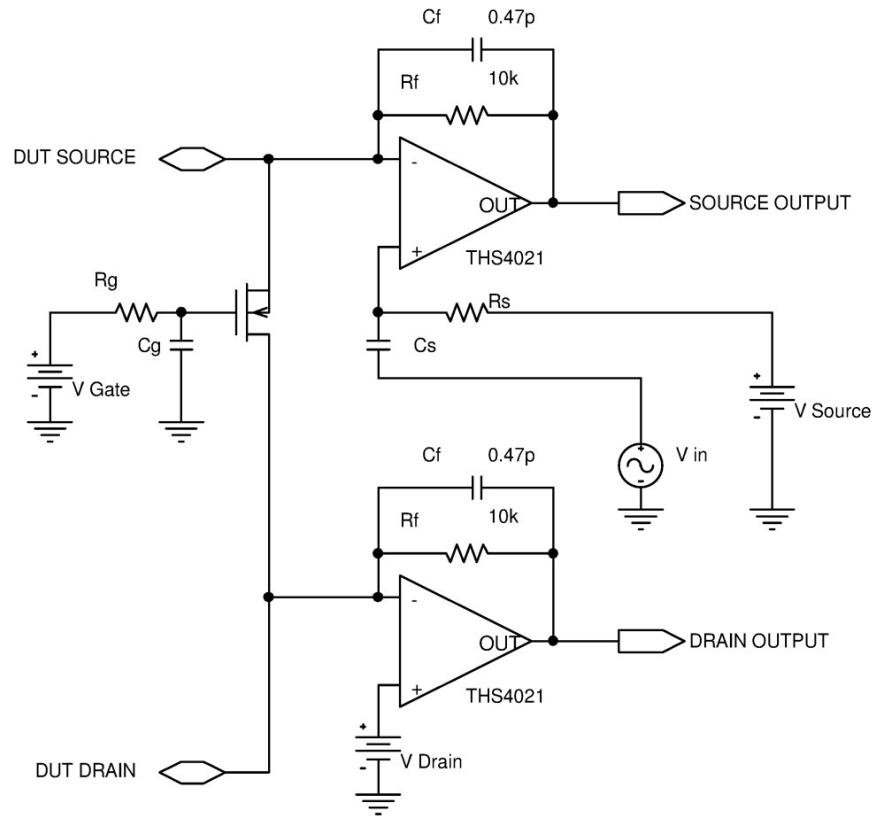


Figure 4.10: Current-sensitive front-end configured for DUT's g_m measure by injecting input signal at the source terminal

This mode of operation give the possibility to measure the transconductance g_m also for bipole or the channel resistance for mosfet devices in ohmic zone with low bias currents.

R0 measure configuration

In this configuration the front-end is basically in the cross-correlation configuration: the only difference is the addition of the input signal injected in the dut's source terminal as showed in paragraph 4.0.2. As showed in 4.0.2, thanks to the use of the C_{gate} capacitor placed between gate and source, the impedance between source and drain have the shape showed in 4.0.2 Starting from the intervention of the C_{gate} and R_{gate} network, the impedance is dominated by the dut's R_0 , which can then be determined as

$$r_0 = \frac{I_{DRAIN}}{V_{in}} = \frac{V_{drain,output}}{gain \cdot V_{source}} \quad (4.10)$$

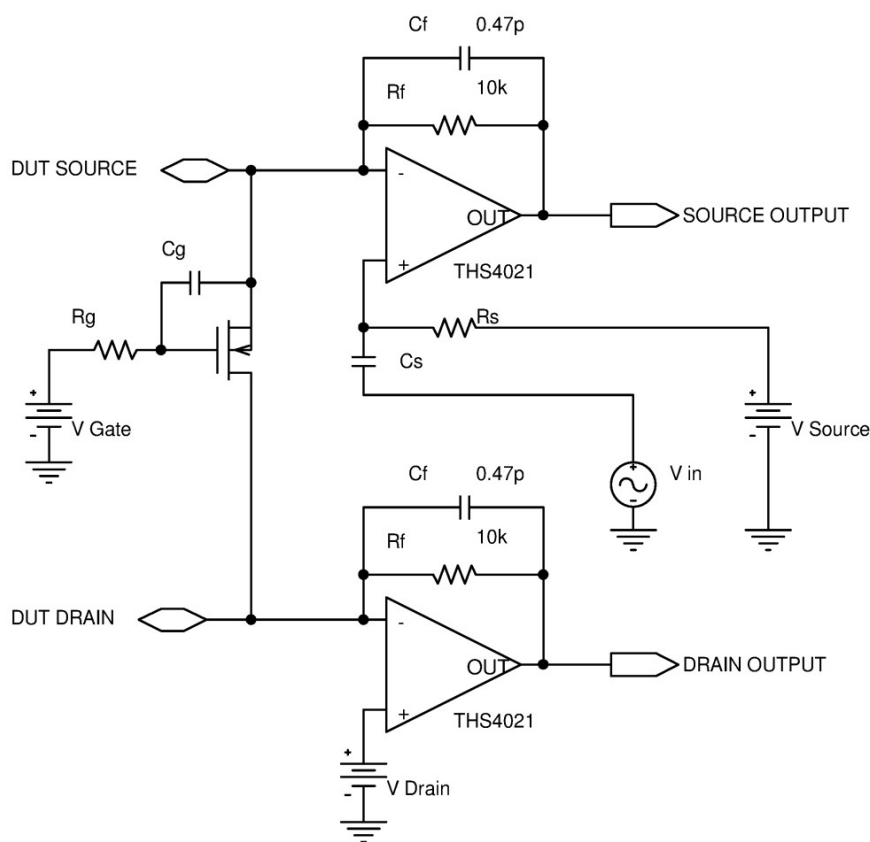


Figure 4.11: Current-sensitive front-end: configured for DUT's R_0 measure

4.1 Physical design and layout

The front-end board is made on a standard two layer pcb, 1.6mm overall thickness, 35 μ m copper thickness. Signals are routed as much as possible only on top layer, minimizing vias and track on the bottom, which is the ground plane reference. The populated board is visible in figure 4.12; the connector to the mainboard is the black one on the right side. The dut must be plugged into the 28 pin zif connector which provides, in addition to gate, drain and source connection, a number of other useful signals: power supply, digital gpio, analog voltage force / sensing and the mainboard signal generator. Is therefore possible to measure discrete packaged devices by simple inserting the pins in to the zif contacts, or integrated devices by bonding the die on a standard 28 pin dip chip carrier placed in the zif socket: in this case the auxiliary signals are useful to power and control circuits placed on the same dut's die or give other required bias voltage, a typical example is biasing the chip substrate.

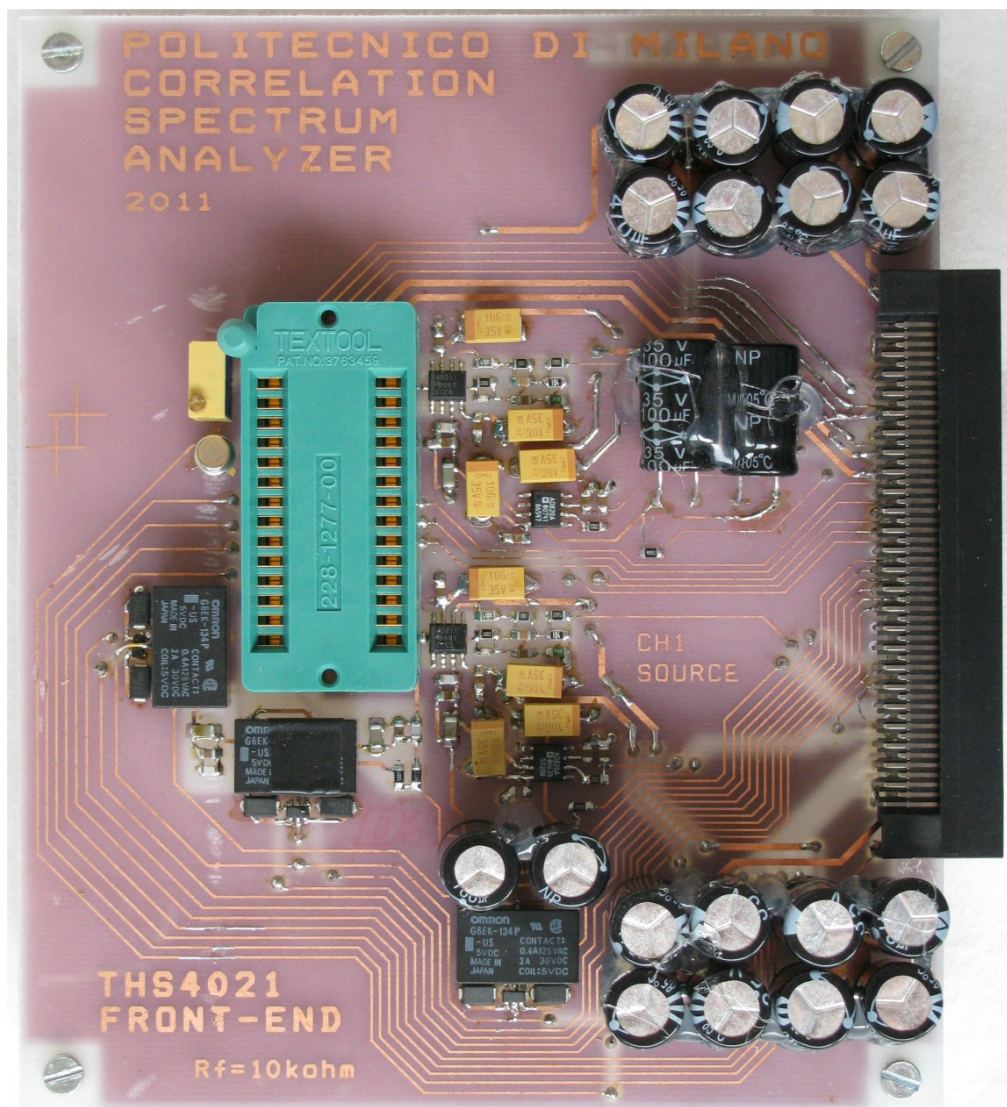


Figure 4.12: Current-sensitive front-end: realized front-end board viewed from the top side

Chapter 5

Front-end for Magnetic Tunnel Junction devices

Tunnel magnetoresistance (TMR) is a magnetoresistive effect that occurs in a magnetic tunnel junction (MTJ), which is a component consisting of two ferromagnets separated by a thin insulator. If the insulating layer is thin enough (typically a few nanometers), electrons can tunnel from one ferromagnet into the other. The magnetic tunnel junctions (MTJ) are based on the spin dependent tunneling effect; this causes MTJs to have different electrical resistances depending on the relative orientation of the magnetizations of the two electrode. Since this process is forbidden in classical physics, the tunnel magnetoresistance is a strictly quantum mechanical phenomenon.

Magnetic tunnel junctions are manufactured in thin film technology. On an industrial scale the film deposition is done by magnetron sputter deposition; on a laboratory scale molecular beam epitaxy, pulsed laser deposition and electron beam physical vapor deposition are also utilized. The junctions are prepared by photolithography.

In addition to being ideally suited as non-volatile magnetic random access memory, magnetic tunnel junctions MTJs are excellent magnetic field sensors. As such, they are used in read-write heads in the magnetic storage industry and played a big role in the increase in storage density of non volatile rams in the past few years. The purpose of this thesis work was to measure the noise characteristic of MTJ devices specifically designed for real time detection of magnetic beads with a double lock-in architecture.

5.1 Tunneling magnetoresistance theory

A magnetic tunnel junction (MTJ) consists of two layers of magnetic metal, such as cobalt-iron, separated by an ultrathin layer of insulator, typically aluminium oxide with a thickness of about 1 nm. The insulating layer is so thin that electrons can tunnel through the barrier if a bias voltage is applied between the two metal electrodes. In MTJs the tunneling current depends on the relative orientation of magnetizations of the two ferromagnetic layers, which can be changed by an applied magnetic field. This phenomenon is called tunneling magnetoresistance (TMR) which is a consequence of spin-dependent tunneling.

5.1.1 Tunnelling through a barrier

Tunneling is a purely quantum mechanical effect which refers to the penetration of a particle through a classically excluded region. Considering a step potential barrier (Fig 5.1) written

as equation 5.1

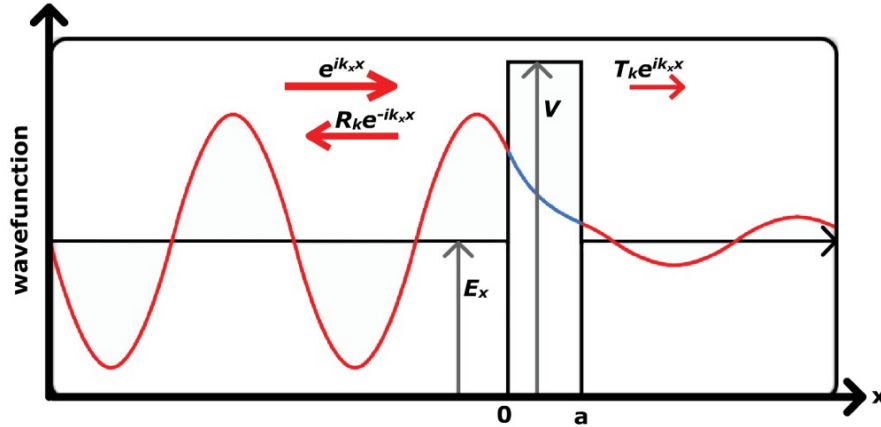


Figure 5.1: Tunneling through a barrier: reflected and transmitted wavefunctions

$$V(x) = \begin{cases} 0, & x < 0 \\ V, & 0 < x < a \\ 0, & x > a \end{cases} \quad (5.1)$$

In classical mechanics, a particle incident upon the barrier will be reflected if its energy is below the threshold ($E < V$) or will be transmitted if its energy is over the threshold ($E > V$). In a more rigorous way the particle have only probability of 1 or 0 to being transmitted or reflected, depending on its energy. The quantum mechanics view is different: particles are described by their waveform functions instead of a classic ballistic model. Therefore the particle have a finite probability to pass through the barrier even if its energy is below the threshold: this is the *tunneling effect* and its probability depends on the height and width of the barrier. For a monodimensional barrier potential, as the one in the figure 5.1, the tunnel probability can be derived analytically solving the time-independent Schroedinger equation for the wavefunction in the three regions ($x < 0, 0 < x < a, x > a$) and matching the boundary conditions in $x = 0$ and $x = a$. In a real systems the potential barrier profile differs from an ideal rectangular step. In these cases numerical approaches or approximations are used, like the WKB approximation that lead to

$$|T_k|^2 \approx \exp \left\{ -\frac{2}{\hbar} \int_0^a \sqrt{2m[V(\tau) - E]} d\tau \right\} \quad (5.2)$$

The WKB approximation can be applied to a Metal-Insulator-Metal structure, such as MTJ devices. The two metal electrodes are described by their Fermi energy level and the insulator act as the potential step barrier. Applying a voltage V between the electrodes slightly changes the barrier shape and splits the two Fermi levels of a quantity eV . This brings some empty levels in correspondence with the filled ones on the other side of the barrier, allowing a net tunneling current flowing from the negatively charged electrode to the positive one. The net current j from electrode 1 to electrode 2 is the difference between the two independent tunneling currents in the two directions:

$$j = j_{1 \rightarrow 2} - j_{2 \rightarrow 1} \quad (5.3)$$

Each one of the two contributions depends on the density of states in the two electrodes, their occupancy described by the Fermi distribution and the tunneling probability.[11]

The distinctive feature of an MTJ device is that the two electrodes are ferromagnetic conductors where the spin-splitting of the bandstructure leads to separate spin-up and spin-down density of states. An interpretation of this configuration is the *Jullière model* in which is assumed that the electron spin is conserved in the tunneling process, creates two parallel independent tunneling conduction channels by spin-up and spin-down (respect to the magnetization of the ferromagnet electrode) electrons. Therefore the equation 5.3 can be rewritten as:

$$j_{TOT} = \left[j_{1 \rightarrow 2}^{\uparrow} - j_{2 \rightarrow 1}^{\uparrow} \right] + \left[j_{1 \rightarrow 2}^{\downarrow} - j_{2 \rightarrow 1}^{\downarrow} \right] \quad (5.4)$$

The *Jullière model* simplifies considering the case of $T = 0^\circ K$. In this situation the densities of states functions in the electrodes can be approximated as constant step with their values replaced by those at the Fermi energy. This leads also to ignore the "reverse current" from electrode 2 to electrode 1. Therefore the equation 5.4 can be simplified to

$$j_{TOT} = \left[j_{1 \rightarrow 2}^{\uparrow} + j_{1 \rightarrow 2}^{\downarrow} \right] \quad (5.5)$$

The tunneling coefficient in the equation 5.2 is assumed independent from electron spin. The MTJ's conductance can be calculated as follow

$$G \propto [(\rho_{1\uparrow} \cdot \rho_{2\uparrow}) + (\rho_{1\downarrow} \cdot \rho_{2\downarrow})] \quad (5.6)$$

It is useful, for MTJ application purposes, to calculate the *TMR* ratio, where G_P and G_{AP} are the conductances in the two extreme cases of parallel (P) and anti-parallel (AP) alignment of the electrodes magnetization vectors:

$$TMR = \frac{G_P - G_{AP}}{G_{AP}} \quad (5.7)$$

The two conductances can be derived from equation 5.6, where N_1, N_2 are majority electrons and n_1, n_2 are minority electrons, respectively in electrode 1 and 2.

$$G_P \propto (N_1 \cdot N_2) + (n_1 \cdot n_2) \quad (5.8)$$

$$G_{AP} \propto (N_1 \cdot n_2) + (n_1 \cdot N_2) \quad (5.9)$$

Introducing the *effective spin-polarization factor* P_i which is a measure, ranging from 0 to 1, of how much an electrodes is "polarized"

$$P_i = \frac{N_i - n_i}{N_i + n_i} \quad (5.10)$$

The TMR ratio 5.7 can be rewritten as

$$TMR = \frac{G_P - G_{AP}}{G_{AP}} = \frac{2P_1P_2}{1 - P_1P_2} \quad (5.11)$$

The tunneling conductance and the magnetoresistance dependence on the bias voltage for a typical MTJ structure are plotted in figure 5.2

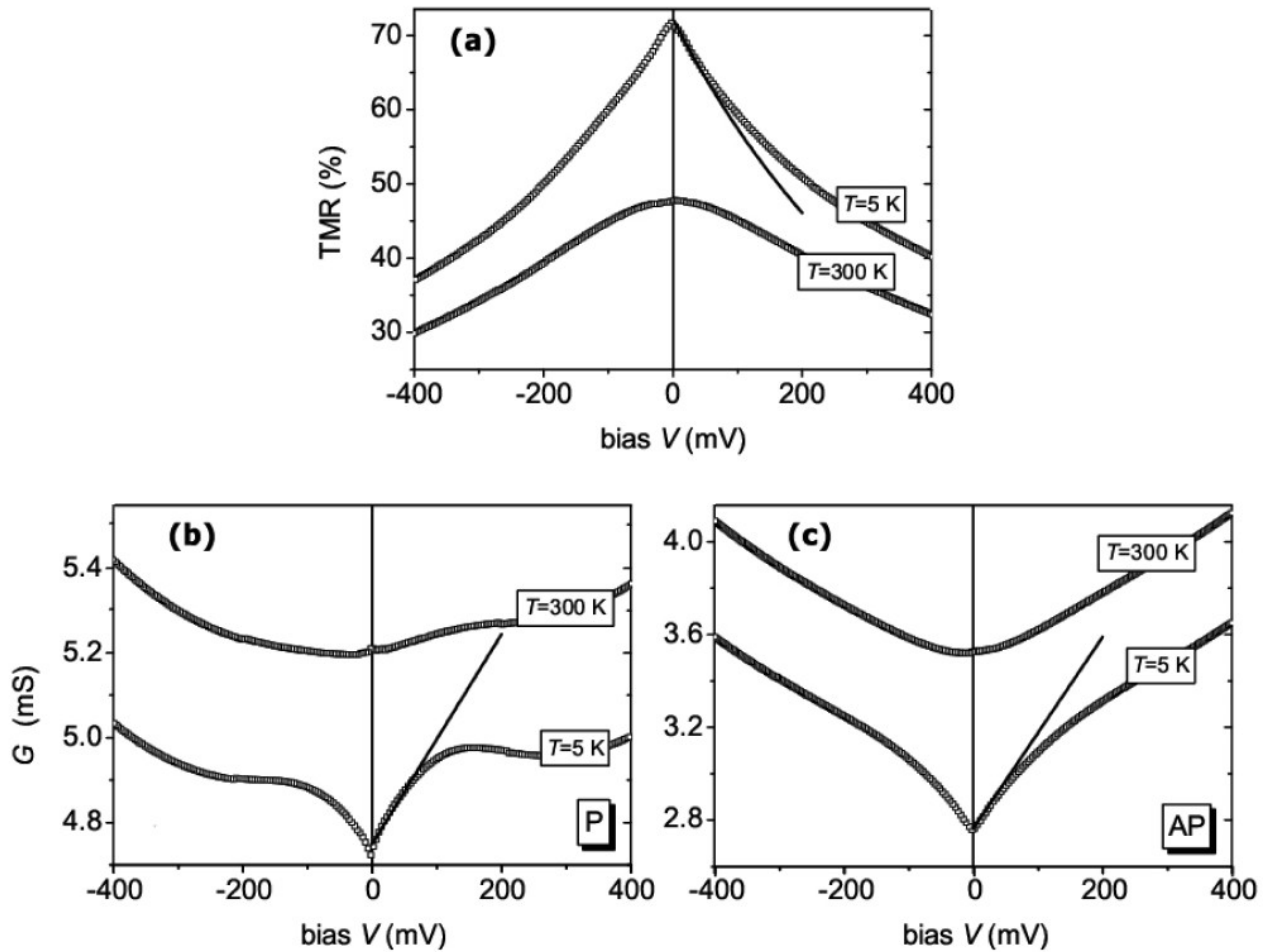


Figure 5.2: Bias dependence of the TMR ratio (a) and of the conductance for parallel (b) and anti-parallel (c) configurations in a CoFeB/AlO_x/CoFeB junction at $T = 5\text{ K}$ and $T = 300\text{ K}$

It is possible to notice a significant decrease of the TMR ratio increasing the applied voltage: A criterion of merit is often the voltage $V_{1/2}$ at which the TMR becomes half of its maximum value; furthermore, at low temperatures, for bias voltage tending to zero, the TMR drop almost linearly, differing radically from the parabolic response predicted by theory. Jullière model is widely used for describing spin-dependent tunneling systems, but fails in many ferromagnet/insulator/ferromagnet junctions because some phenomena are not included in the physical model of the device, particularly concerning the junction barrier interface and insulator properties. However, for the design of a cross-correlation front-end, no further detailed model are needed. The dependence on the temperature, visible in figure 5.2 and more detailed in figure 5.3 tends to decrease for all kinds of MTJs of about 25% from 4.2°K to 300°K [11]

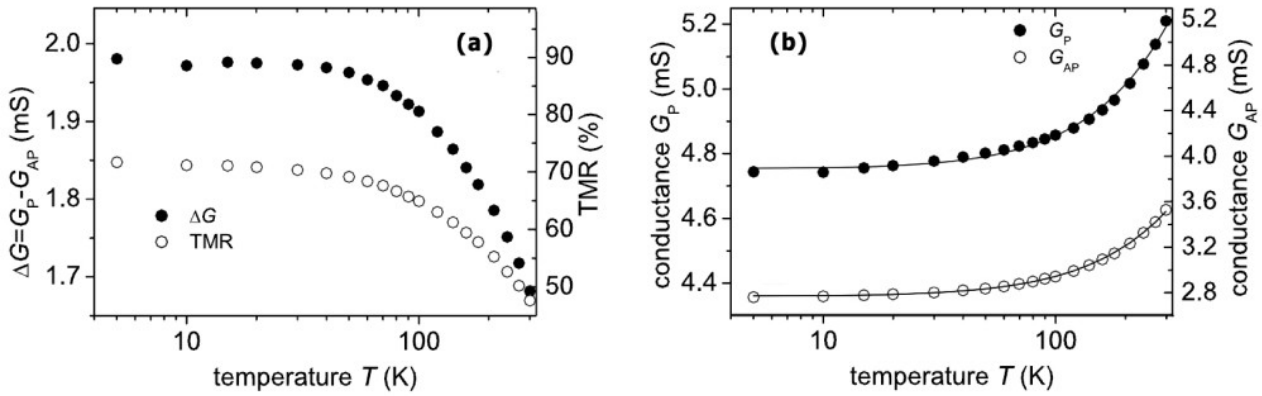


Figure 5.3: (a) The quantity ΔG and TMR as a function of temperature. (b) Temperature dependence of the P and AP conductance at a bias of 2mV. Same CoFeB/AIO_x/CoFeB junction as in figure 5.2

5.1.2 Sensor layout and characteristics

In figure 5.4 are showed the basic structure from which the sensor will be fabricated through photolithography. The core TMR structure is made by the two CoFeB layer and MgO isolator. The Ta/Ru/Ta buffer and Ta/Ru capping structures affect the crystallization of the CoFeB MTJ junction layers. [11] The Ru/CoFe/IrMn is an *exchange biased synthetic antiferromagnet* which act as a fixed magnetic reference for the bottom CoFeB pinned layer of the MTJ junction; in contrast the top CoFeB layer magnetization is free to follow the external field and is the "sensor element" of the device.

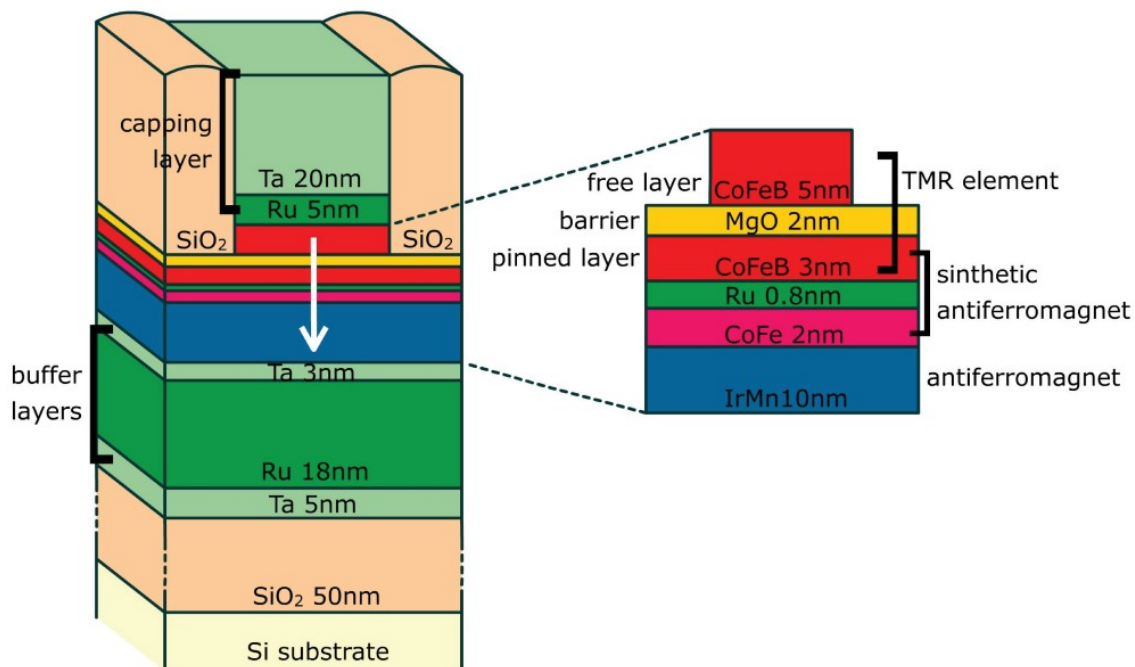


Figure 5.4: Transversal structure of a MTJ device

The overall sensor structure is made on a standard silicon substrate and is electrically isolated from this one by a layer of silicon oxide.

5.2 MTJ noise sources

Typical noises sources in MTJ devices are [13]

- Thermal Electronic Noise
- Shot Noise
- Thermal Magnetic Noise
- Electronic and magnetic $1/f$ Noise
- Random Telegraph Noise (RTN)

Thermal Electronic Noise pervasively appears in all types of conducting media due to the random motions of charge carriers agitated by local temperature variations near Fermi level. Such an electron migration phenomenon can be regarded as Brownian motion. In MTJs, this thermally induced noise is approximately white noise, it appears almost at all frequencies and is described by the well-know equation 5.12

$$S_V^{therm,elec} = 4k_B T R \quad (5.12)$$

Shot Noise is associated with the discreteness of electrical charge caused by the stochastic nature of the electron emission process. Since the emission events are uncorrelated, the emission process of an individual electron from a cathode can be considered as Poisson distribution. The corresponding fluctuations power density is described by the well know equation 5.13

$$S_I^{shot} = 2eI \quad (5.13)$$

While the shot noise is expected in tunneling systems, several research groups find shot noise levels lower than the value calculated by equation 5.13 In MTJ devices the junction is small enough for the electrons to become correlated in high biased level due to interaction of Coulomb repulsion effect and Pauli exclusion principle that limit the density of electrons. This lead to a sequential correlated tunneling of electrons through the barrier. Usually for MTJ devices, the thermal electronic noise and the shot noise are expressed by the single equation 5.14,

$$S_V^{therm-shot} = 2eIR^2 \coth\left(\frac{eV}{2k_B T}\right) \quad (5.14)$$

Thermal Magnetic Noise arise from magnetization fluctuations in MTJs, is frequency independent and can be considered as white noise. There is also **Magnetic $1/f$ Noise** component originated by random fluctuations of magnetic domains which causes random fluctuations of device resistance.

Electronic $1/f$ Noise is virtually ubiquitous in all electronic devices; the sources of this kind of noise is never completely identified and the describing formula is typically empirically derived from experimental measure rather than from a single physical phenomena. For MTJ can be described by

$$S_I^{elec1/f} = \alpha_{elec} \frac{V^2}{Af^\beta} \quad (5.15)$$

Where V is the applied voltage and A is the junction area and α_{elec} is the *Hooge parameter*. The exponent β ranges between $0.6 \leftrightarrow 2.0$ for MTJ devices.

Random Telegraph Noise (RTN) is not always visible as is shadowed by $1/f$ noise at low frequencies. The power spectrum of RTN is Lorentzian and it is given by

$$S_I^{RTN} = \frac{S_0}{1 + (f/f_0)^2} \quad (5.16)$$

where S_0 is the frequency-independent value, f_0 is the characteristic roll-off frequency described by $f_0 = (2\pi\tau)^{-1}$ and τ is the relaxation time of Lorentzian fluctuations.

5.3 Design of the voltage-mode front-end

Since the target dut have maximum resistance of $1k\Omega$, the front-end is based on a voltage-mode topology, which is the ideal choice for low-impedance dut, as described before in section 1.5. The lock-in frequency, the final application for which these sensors are designed, is typically of a few tens kHz [15]: consequently the front end was designed for at least 1MHz bandwidth to go slightly over and have more complete noise characterization. The complete front-end circuit is shown in figure 5.5

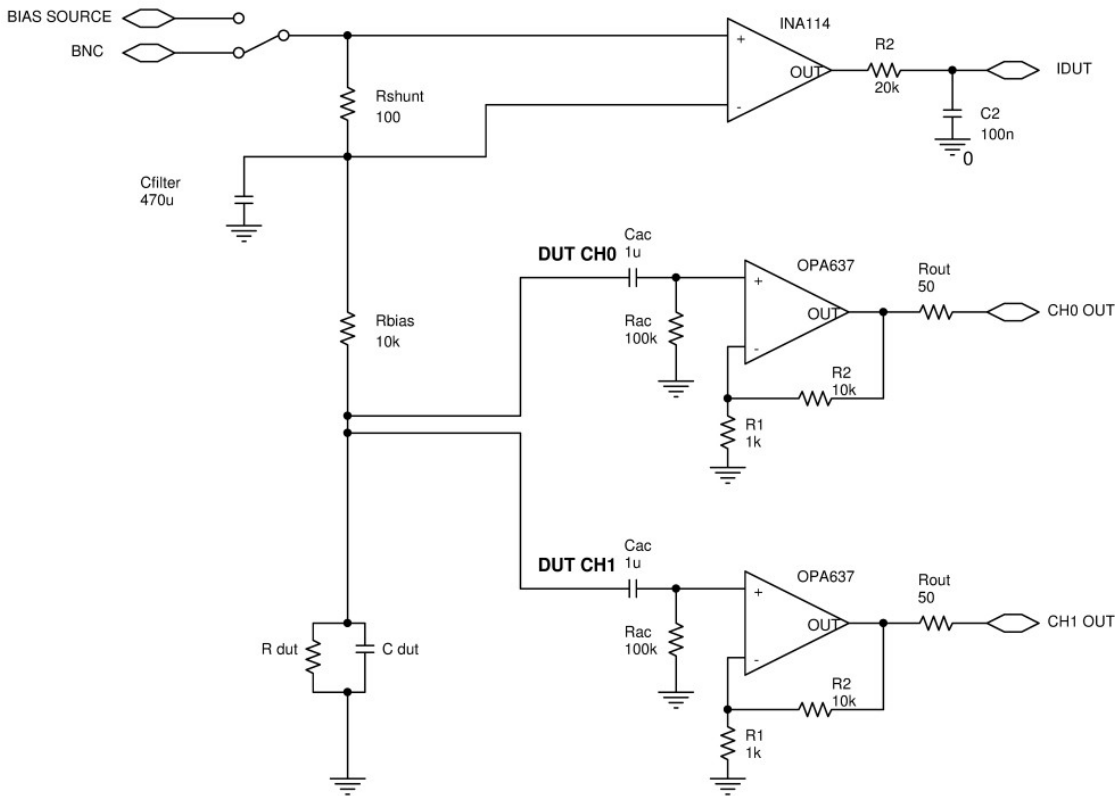


Figure 5.5: Complete front-end circuit for MTJ noise measure

The two channels are made around a low noise fet input operational amplifier, OPA637, in a simple non inverting configuration with a gain $G = (1 + R_2/R_1) = 11$. The main difference between the ideal voltage-mode front-end shown in figure 1.4 and this circuit is the capacitive coupling made by R_{AC} & C_{AC} between the dut's and the input of the amplifiers; its required by the high dc bias voltage of some MTJ devices, above the input dynamic range of the OPA637, limited between $+2.0V$ and $-3.5V$. The choice of $C_{AC} = 1\mu F$ and $R_{AC} = 100k\Omega$ led to an

high pass filter cut frequency of 1.6Hz. The drawback of this solution is the presence of R_{AC} , that has effect on both correlated and uncorrelated noise: it change the dut's impedance from 5.17 to 5.18 and moreover add its own contribute to correlated and uncorrelated noises.

$$Z_{DUT} = \frac{R_{DUT}}{1 + S \cdot R_{DUT} \cdot (C_{DUT} + C_P)} \quad (5.17)$$

$$Z_{DUT,R_{AC}} = \frac{R_{DUT} || 2R_{AC}}{1 + S \cdot R_{DUT} || 2R_{AC} \cdot (C_{DUT} + C_P)} \quad (5.18)$$

The resistor's current noise $4KT/R_{ac}$ is in the same position of the opamp positive input equivalent noise generator so it contribute in the same way, equations 1.32 and 1.33, to correlated and uncorrelated noise.

The dut is biased by a variable voltage generator and a series resistor R_{BIAS} ; this one is formally in the same position of R_{DUT} so, as the dut, change the Z_{DUT} value and introduce correlated noise that, as usual, affect the instrument sensibility. To monitor the dut's bias current a shunt resistor ($R_{shunt} \ll R_{bias}$) is placed between the voltage generator and the bias resistor. A classic three opamp instrumentation amplifier, INA114 by Texas Instruments, read the voltage drop across the shunt resistor to obtain the I_{DUT} value. The capacitor C_{FILTER} and the resistor R_{SHUNT} form a passive RC low-pass filter that attenuate the inevitable noise coming from the dc bias generator.

The choice of R_{BIAS} resistor is critical, since it influence both bias current and correlated noise: higher values minimize the noise but decrease the maximum dc bias current. The adopted solution was simply to not choose a fixed value, but left this resistor, and R_{shunt} too, interchangeable depending on the dut specific needs. To increase I_{DUT} without decreasing R_{BIAS} its possible to use an external voltage generator (BNC input in figure 5.5) instead of the one provided by the pc control board, which can reach a maximum of $\pm 10V$. This is a simple solution but requires an external low noise voltage generator as well an external precision amperometers, since the the INA114 can sustain up to $\pm 48V$ without damage but works only up to its supply rails, which are $\pm 15V$. However, both solution are present on the front-end board to remove any restrictions and make the circuit suitable for any type of MTJ devices.

5.4 Physical design and layout

The front-end board is made on a standard two layer pcb, 1.6mm overall thickness, 35 μm copper thickness. Signals are routed as much as possible only on top layer, minimizing vias and track on the bottom, which is the ground plane reference. The populated board is visible in figure 5.7; the connector to the mainboard is the black one on the right side. The magnetoresistor array is placed and bonded in a dip ceramic chip holder that must be placed in a zif socket surrounded by two double row of contact. The connections to the front-end amplifiers are made by free detachable copper wires. Each one unselected device of the array can be independently left open or tied to ground on both contact: this minor feature has allowed to identify and model the parasitic interaction between the devices themselves and chip substrate. Figure 5.6 shown a close-up view of the contact system.

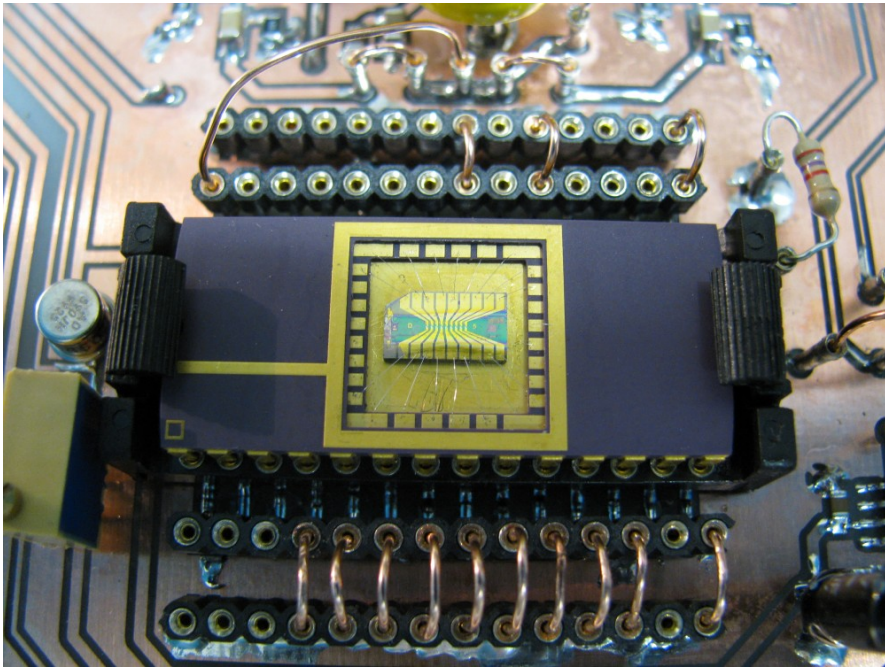


Figure 5.6: Close up of MTJ chip carrier inserted in to the front-end board

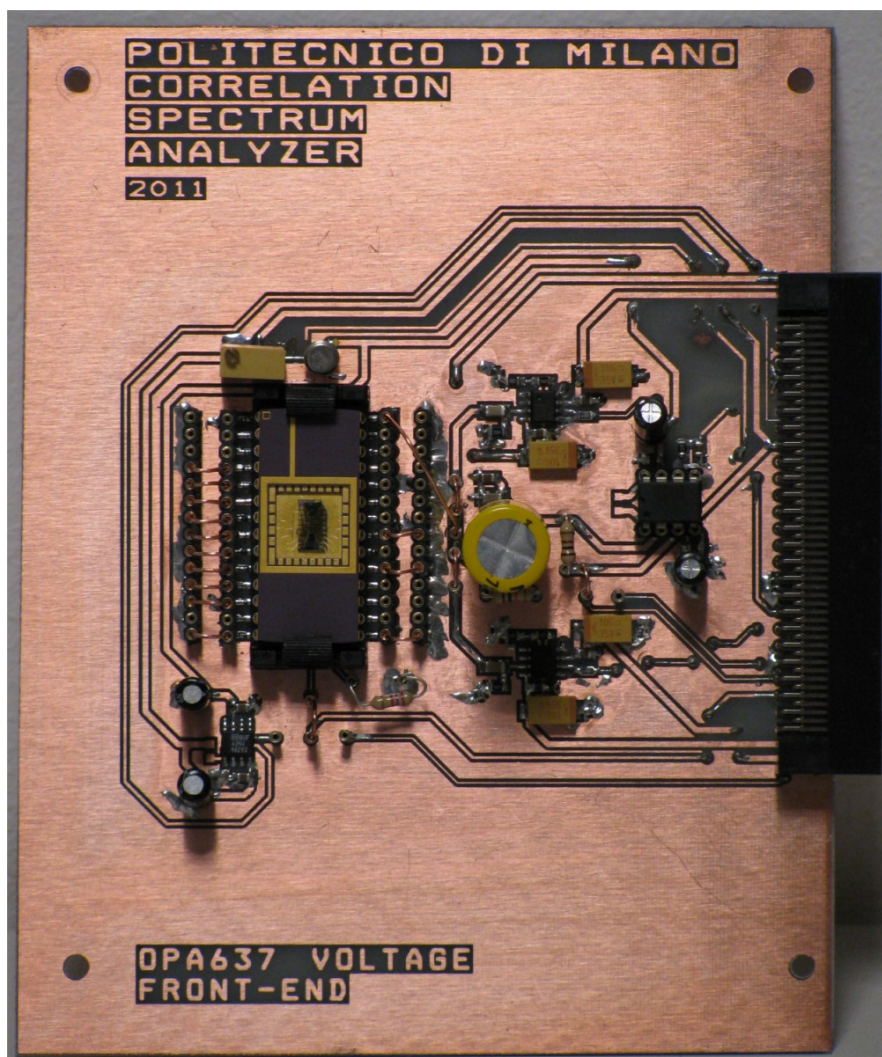


Figure 5.7: Front-end board for MTJ noise measurement viewed from the top side

5.5 Front-end validation

Before starting to work on MTJ devices, two simple test measure was made on standard discrete resistors. In the fist one, shown in figure 5.8, the bias current was changed from zero up to the maximum value: all three measure are in good agreement whit the expected value, exopt above 1MHz, where growth come from the instrument itself. This phenomenon, also evident in MTJ measures, has not been fully understood but depends strongly on the impedance at the front-end inputs.

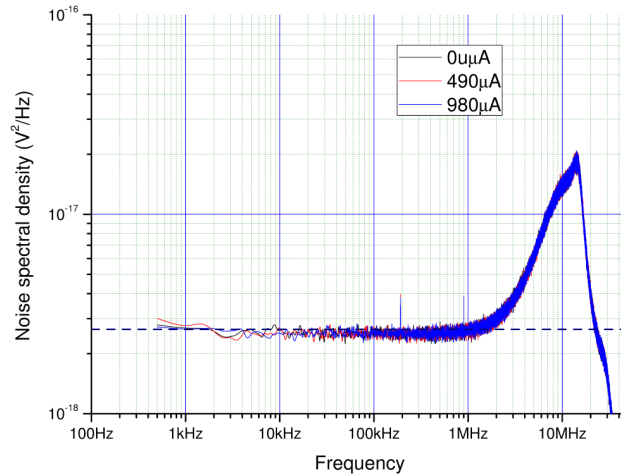


Figure 5.8: Noise of 160Ω resistor at three different bias voltage; high frequency measure without low pass filter

The second test, reported in figure 5.9, was made whit low pass filter activated to verify the results at low frequencies: its evident a strong interference at 50Hz, ans subsequent harmonics, due to the power network. The instrument has proved to be very sensitive to these issues and therefore care must be taken to avoid this unwanted signals: the red measure was acquired with the instrument case fully closed and all possible source of interference, like notebooks power switch, placed as far as possible from the instrument. Despite these precautions some peaking are still present at 50Hz and 200Hz.

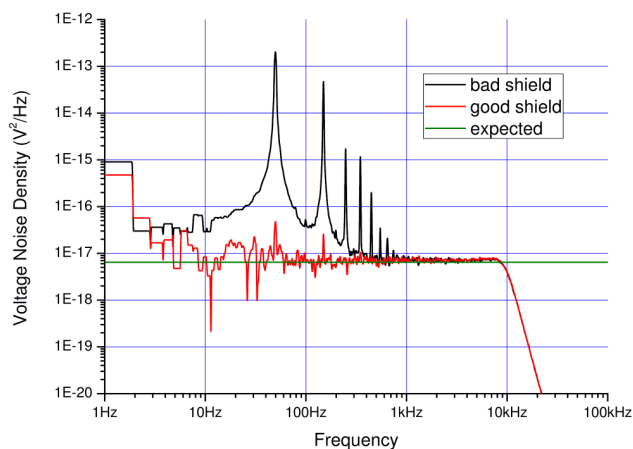


Figure 5.9: Noise of 390Ω resistor with no bias and low pass filter activated; effect of external electromagnetic noise sources

5.6 MTJ characterization and noise measurement

To test the correlation spectrum analyzer a sample device consist of a single silicon die of about 3mm x 7mm with eight identical and independent MTJ are used. The structure scheme are showed in figure 5.10 and figure 5.11 is a photograph of the array through a microscope. These sensors can have various resistance, depending on the MgO oxide tickness: 10k Ω (2nm), 1k Ω (1.4nm), 100 Ω (0.9nm).

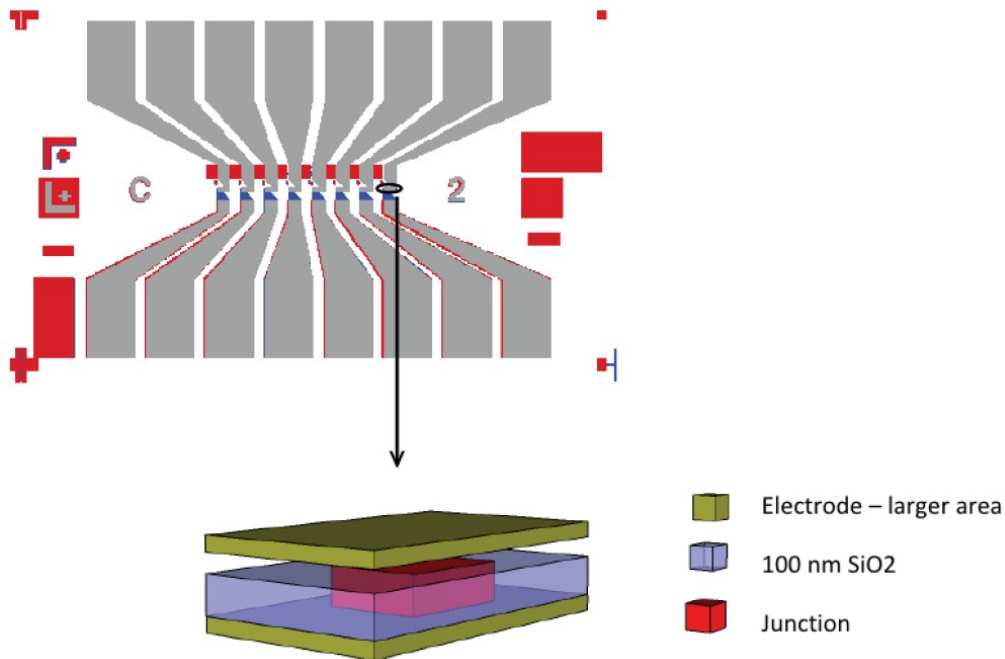


Figure 5.10: Magnetic Tunnel Junctions, array of devices on single die



Figure 5.11: Magnetic Tunnel Junctions, array of devices on single die, photograph by optical microscope

5.6.1 Measures on $1k\Omega$ MTJ devices

This sample chip was been already heavily used in a previous number of tests: only two devices were found working, the other six have been found damaged with only 50Ω junction resistance. This two working devices, renamed $alpha = \alpha$ and $gamma = \gamma$, were characterized by a number of measure.

Figure 5.12 is the result of a dc voltage sweep between $\pm 1V$ with a $2mA$ current limit and no external magnetic field applied, made to verify the functionality of the device and obtain the MTJ's resistance, simply calculated as the ratio $R = V/I$ and reported in figure 5.13 for both devices.

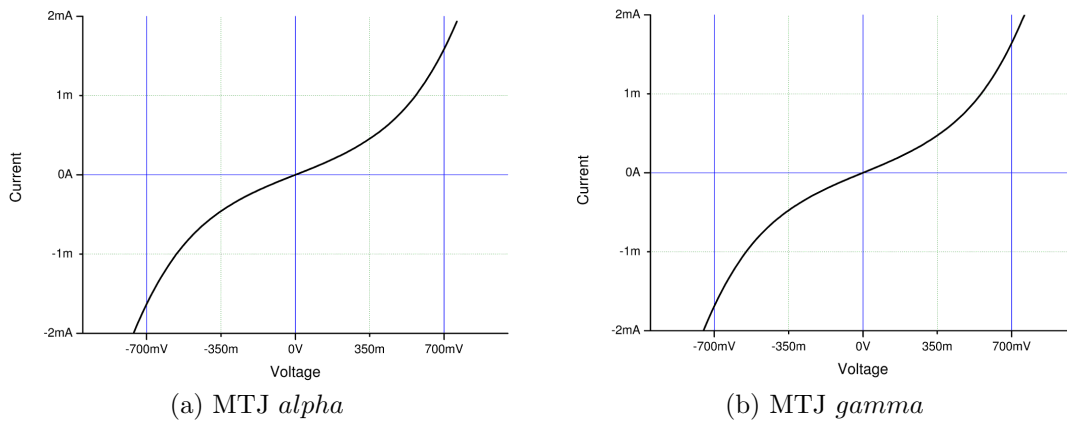


Figure 5.12: $1k\Omega$ MTJ, I-V characteristics, $2mA$ current limit

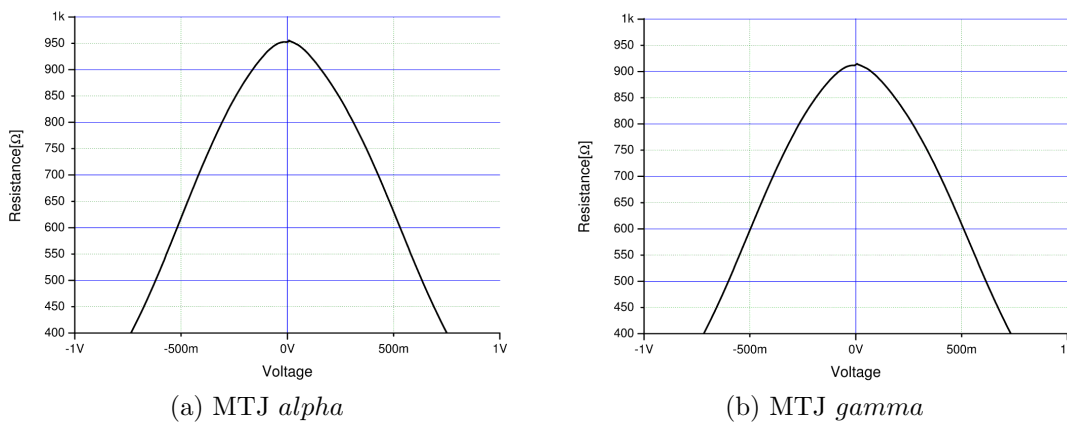


Figure 5.13: $1k\Omega$ MTJ: constant voltage resistance

The first noise characterization where made on MTJ γ biased at relatively high current, up to $200\mu A$, much more than the bias current used in the MTJ applications [15]

Therefore the chosen resistor value were $R_{BIAS} = 10k\Omega$, $R_{SHUNT} = 100\Omega$; the device resistance at the different measurement current are listed in table 5.1 and the noise measures are shown in figure 5.14. All the following measure have been made with the instrument in the *high frequency configuration* (anti-aliasing filters disabled, sampling rate of $100MS/s$) and $3.15s$ of correlation time.

At $0\mu A$ of bias current the measured noise is in perfect agreement with the expected white noise $4KTR$ of a 915Ω resistor(dotted line); there is no presence of shot noise at all, even at the higher bias current of $200\mu A$. For all bias current the total noise is entirely dominated by

the $1/f^\beta$ contribute, with a slope $\beta \cong 0.84$

Other measures are taken at bias currents of $10\mu A$, $20\mu A$, $30\mu A$, $40\mu A$ to extrapolate the dependence of $1/f$ noise on the bias current: the result are show in figure 5.15 where the noise are evaluated at 10kHz.

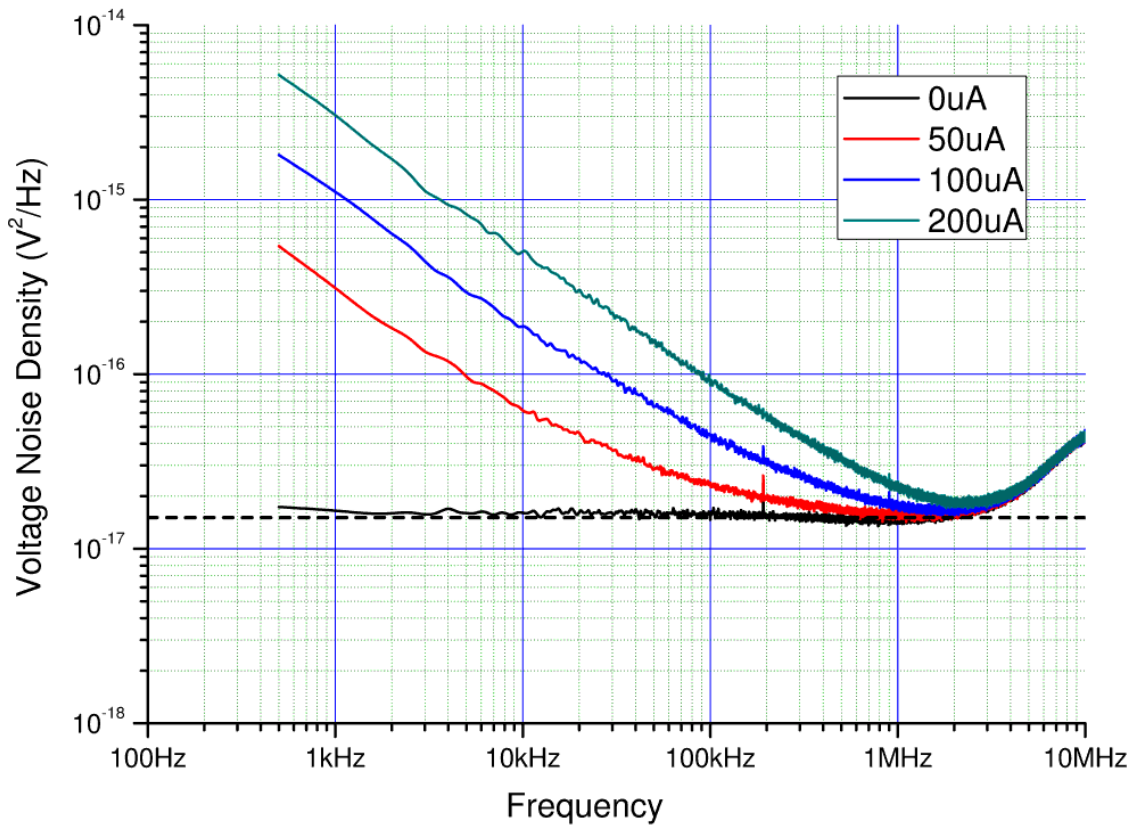


Figure 5.14: Voltage Noise Density of MTJ γ ; dotted black line is the white thermal noise expected at $0\mu A$

BIAS Current	Resistance
$0\mu A$	915Ω
$50\mu A$	901Ω
$100\mu A$	866Ω
$200\mu A$	780Ω

Table 5.1: MTJ γ , resistance at different measured bias current

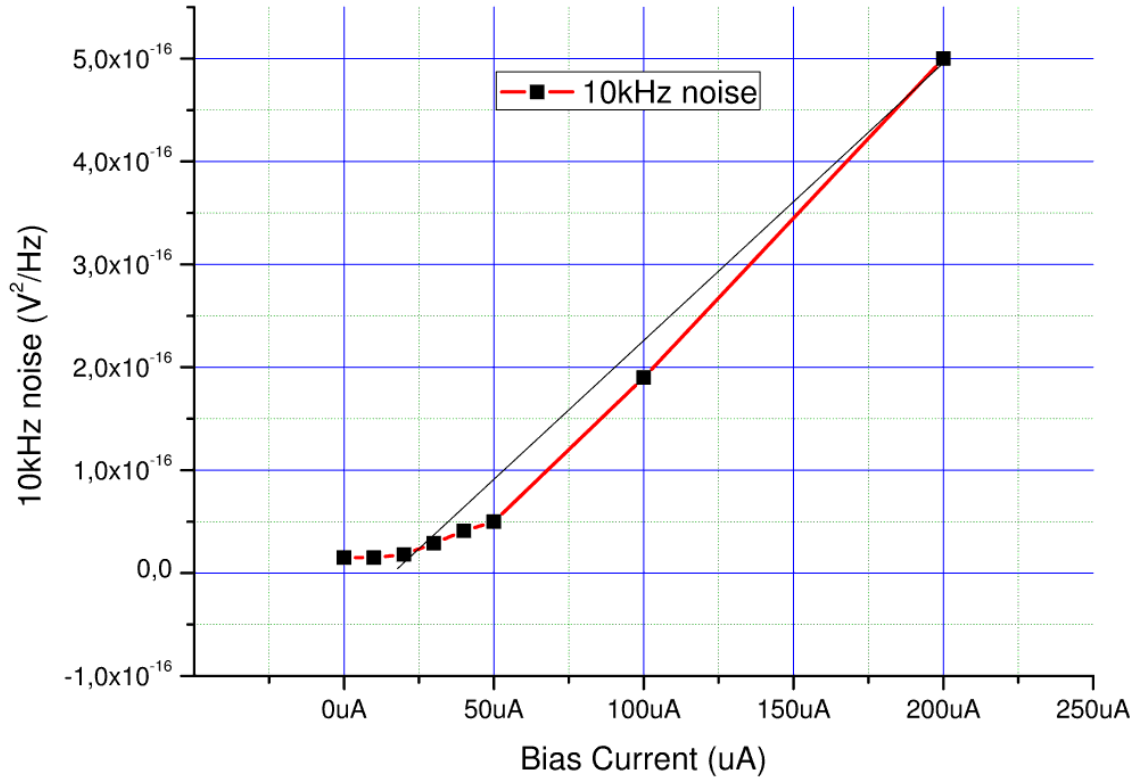


Figure 5.15: MTJ γ , noise sampled at 10kHz at different bias currents

To validate these measures previously shown an artificial DUT was constructed with the same impedance characteristic of the device. A measure with an LCR meter showed a capacity of around $60pF$ in parallel with the MTJ device; consequently the artificial dut was made by the parallel of $1k\Omega$ resistor and $100pF$ ceramic high speed capacitor. The resistor is slightly higher and the capacitor slightly bigger than the real MTJ to have some degree of confidence. This artificial DUT was biased with the same bias currents of the MTJ to ensure that the measured noises are really generated by the MTJ and does not come from unexpected instrument effect. The measures on the artificial DUT are shown in figures 5.16 and 5.17; there is no $1/f$ evidence of low frequency noise generated by the instrument's front-end. The noise growth at high frequencies (above 300kHz) come from the instrument itself. This phenomenon has not been fully understood but depends strongly on the impedance at the front-end inputs.

After it has been verified the operation of the instrument and the validity of the noise measures, a second measurement set on both device alpha and gamma was made, to investigate the noise behavior of the MTJ with lower and more realistic current ranging from $1\mu A$ to $10\mu A$ at $1\mu A$ step, and from $10\mu A$ to $50\mu A$ at $5\mu A$ step. With this lower bias current the value of R_{BIAS} and R_{SHUNT} was increased to decrease the unwanted correlated noise from R_{BIAS} itself and the noise from bias voltage generator. The new chosen values are $R_{BIAS} = 47k\Omega$ and $R_{SHUNT} = 1k\Omega$. At each current value two different measures where made, one at high frequencies as the previous set at $50\mu A$, $100\mu A$, $200\mu A$ and another one at lower frequencies with the low-pass filters enabled; they have been graphically overlapped between 1kHz and 5kHz to create a smooth conjunction between them. The results, only for selected bias current values to keep the graph readable, are shown in figures 5.20 for the device *alfa* and 5.18 for the device *gamma*. Figures 5.21 and 5.21 show the noise sampled at various frequency for each bias current value.

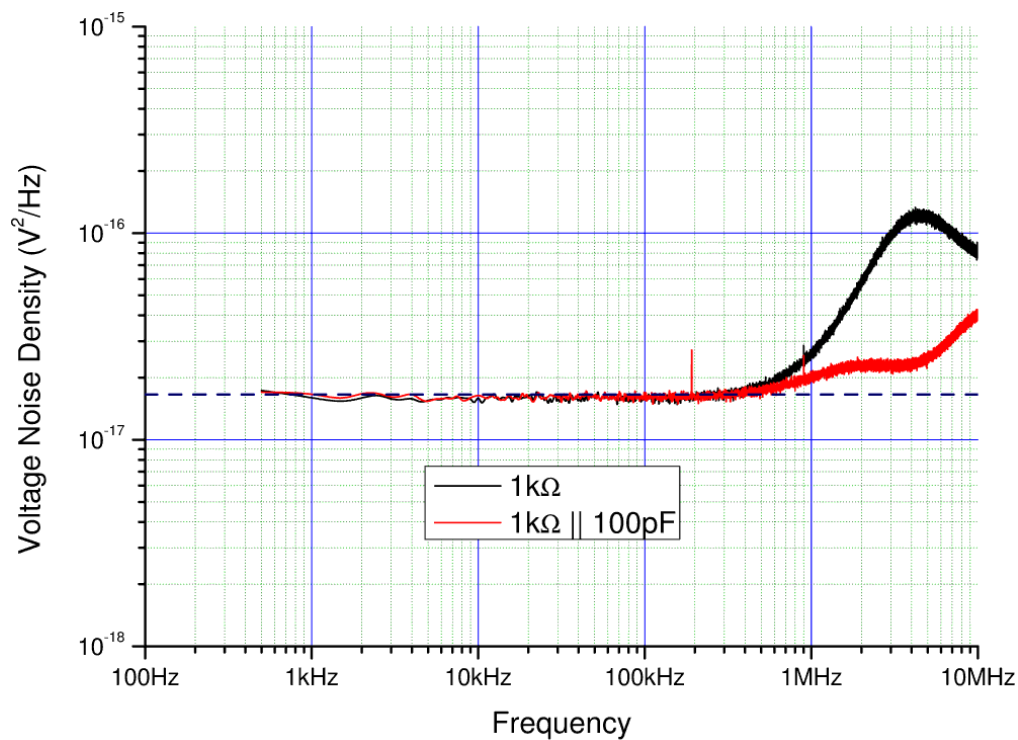


Figure 5.16: Measured noise of a $1k\Omega$ resistor with and without $100pF$ parallel capacitor; dotted blue line is the expected white thermal noise

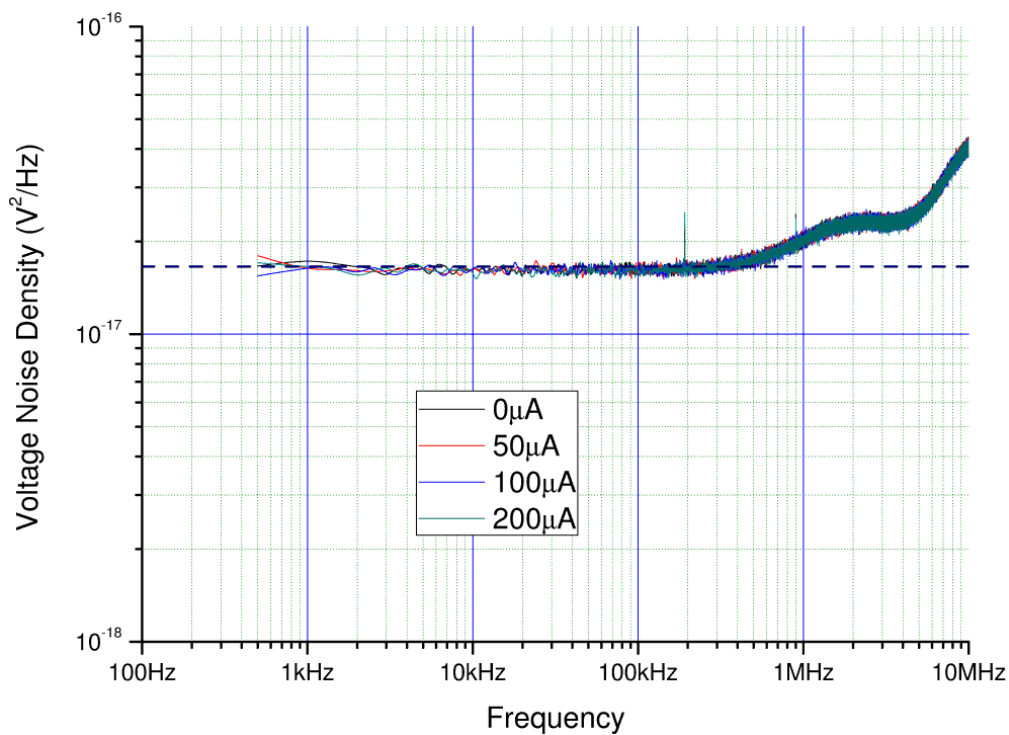


Figure 5.17: Measured noise of the artificial DUT made by $1k\Omega$ resistor and $100pF$ parallel capacitor, at same bias currents of figure 5.14; dotted line is the expected white thermal noise

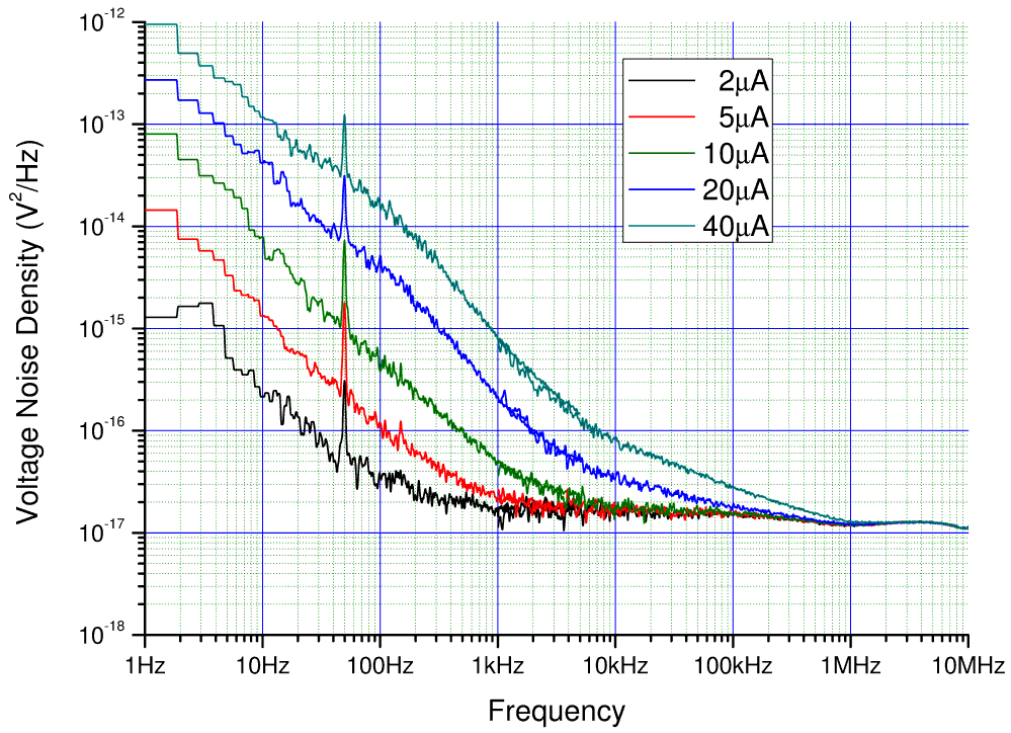


Figure 5.18: MTJ γ , measured voltage noise density. Each curve is an union of a measure at low frequency and another one at high frequency

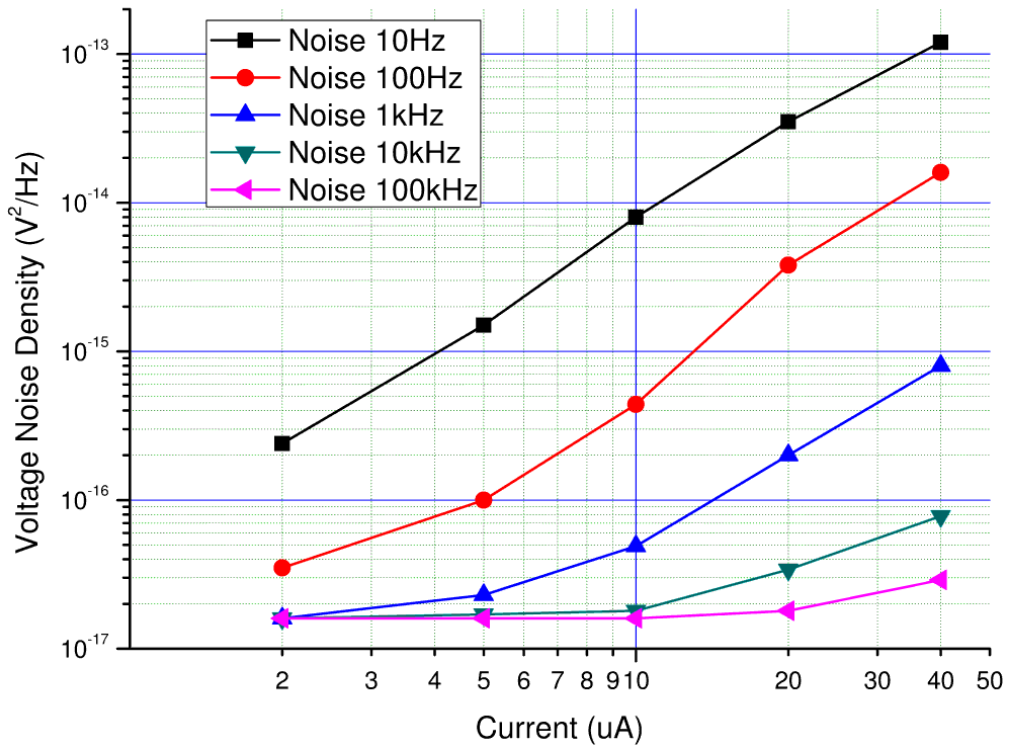


Figure 5.19: MTJ γ , voltage noise density sampled at various frequencies, against bias current

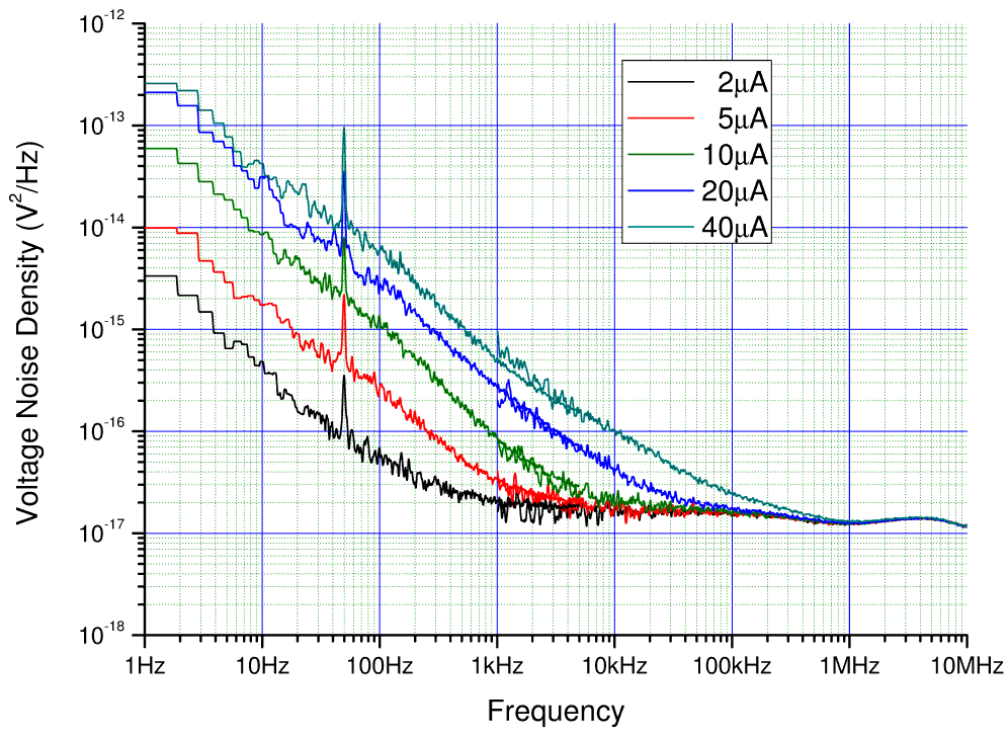


Figure 5.20: MTJ α , measured voltage noise density. Each curve is an union of a measure at low frequency and another one at high frequency

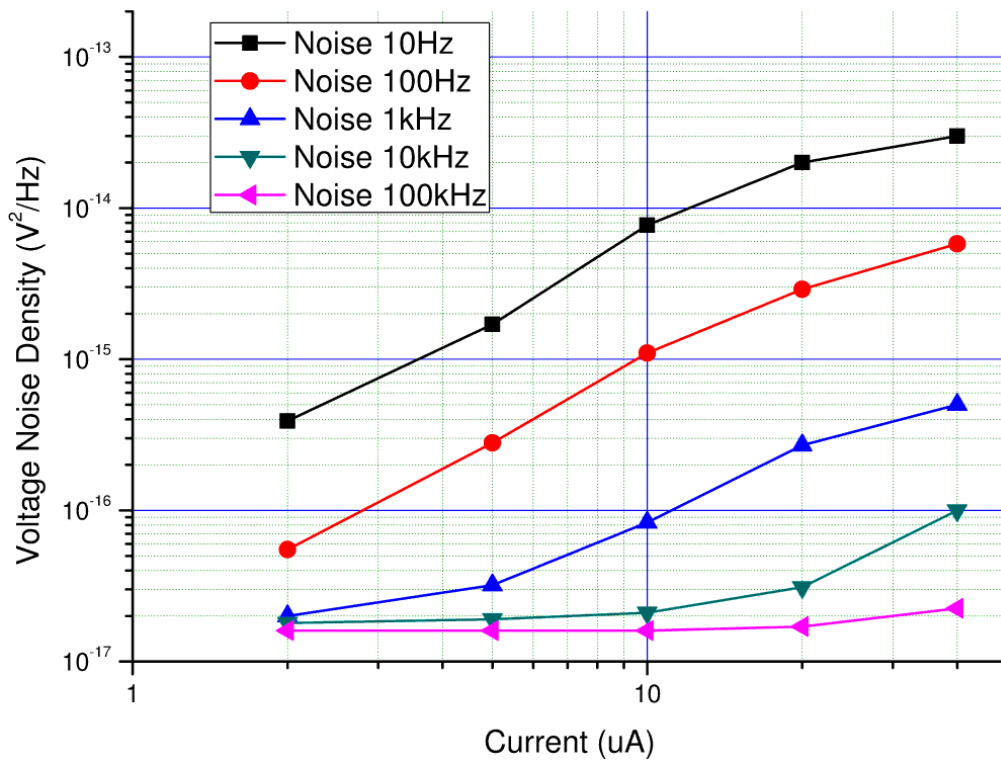


Figure 5.21: MTJ α , voltage noise density sampled at various frequencies, against bias current

5.6.2 Measures on 10k Ω MTJ devices

A set of measure was briefly made on MTJ sensor characterized by $\cong 10k$ resistance. The instrument were configured in the high frequency mode, thus the low pass filters at 10kHz were deactivated. The noise measures are shown in figure 5.22 where the red solid line is the thermal noise of a 11.5k Ω resistor that is the measured resistance of the device. Differently from the 1k Ω devices there is an evidence of shot noise. In figure 5.23 are represented:

- (solid black line) measured noise sampled at 50Hz, as a function of bias current
- (pink dotted line) measured noise sampled at 10kHz, as a function of bias current
- (solid red line) value predicted by theory considering only shot and thermal noise, see equation 5.14
- (solid blue line) value predicted by theory considering the shot noise, thermal noise and the 1/f noise calculated by the Hooge relation, see equation 5.15

The measure at 10kHz is in good agreement with the model that consider only shot and thermal noise, while the noise at 50Hz grow at a more than linear rate, predictable by an Hooge empirical model.

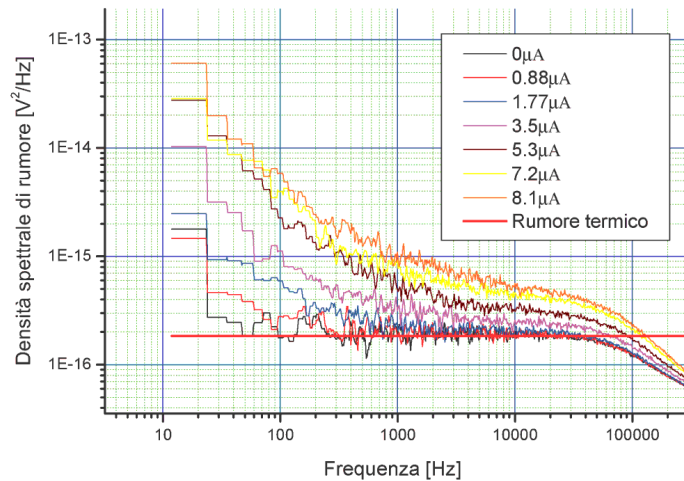


Figure 5.22: 10k Ω MTJ device; measure noise spectral density

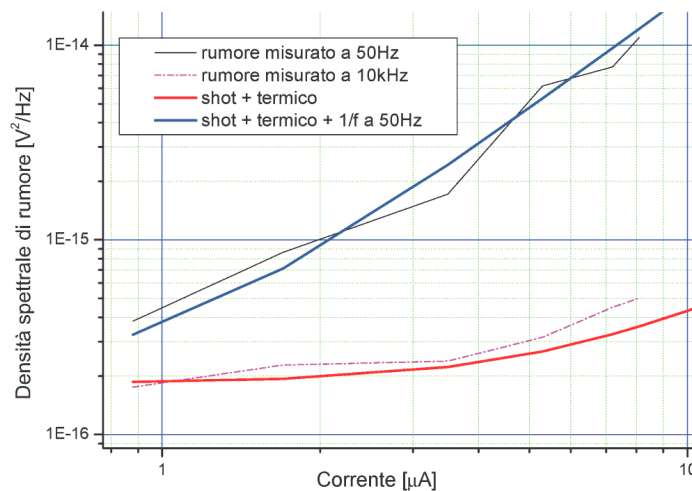


Figure 5.23: 10k Ω MTJ device noise against bias current

5.6.3 Measures on 100Ω MTJ devices

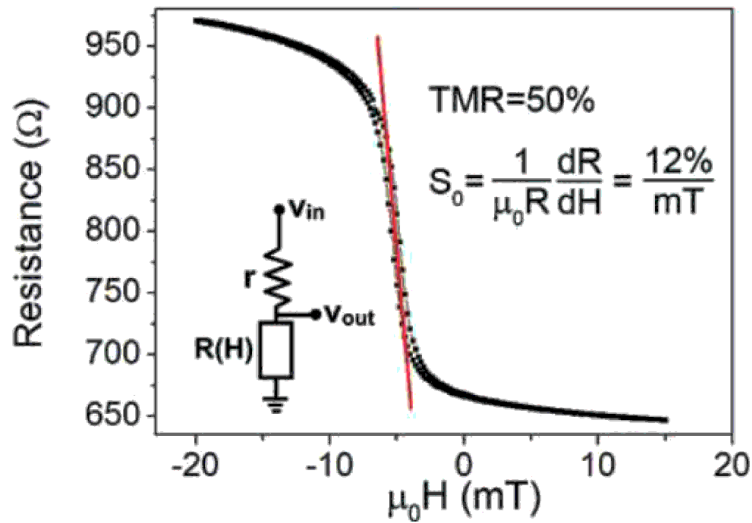


Figure 5.24: R-H plot for a typical MTJ device: maximum sensibility (red line) correspond to a non-zero applied magnetic field

The devices with resistance of 100Ω are made with an MgO oxide thickness of only 0.9nm; to avoid any damage the bias voltage across the dut was always kept below 20mV corresponding to a maximum bias current of 200μA. With this low bias condition is hard to clearly identify a shot noise, since it is always lower than the expected thermal noise of a 100Ω resistor. This device was measured also with applied magnetic field by the use of permanent magnets: the importance of this measure is evident looking at the figure 5.24 where is reported a typical R-H, resistance value as a function of applied external magnetic field, of an MTJ device: the maximum sensor sensibility is obtained with an applied external fixed value magnetic field and therefore is important to evaluate the MTJ noise in this condition.

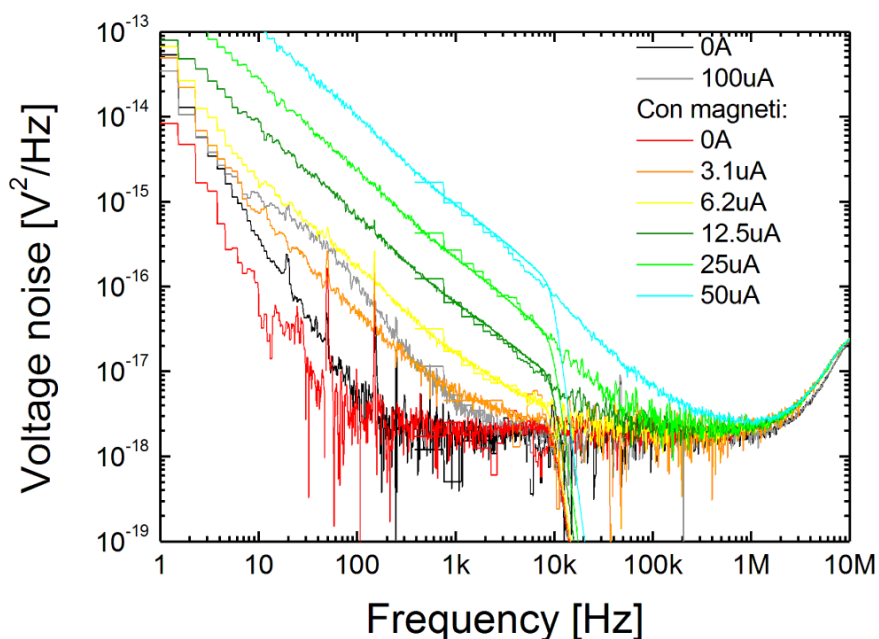


Figure 5.25: 100Ω MTJ device C2-1, measured noise with and without applied magnetic field

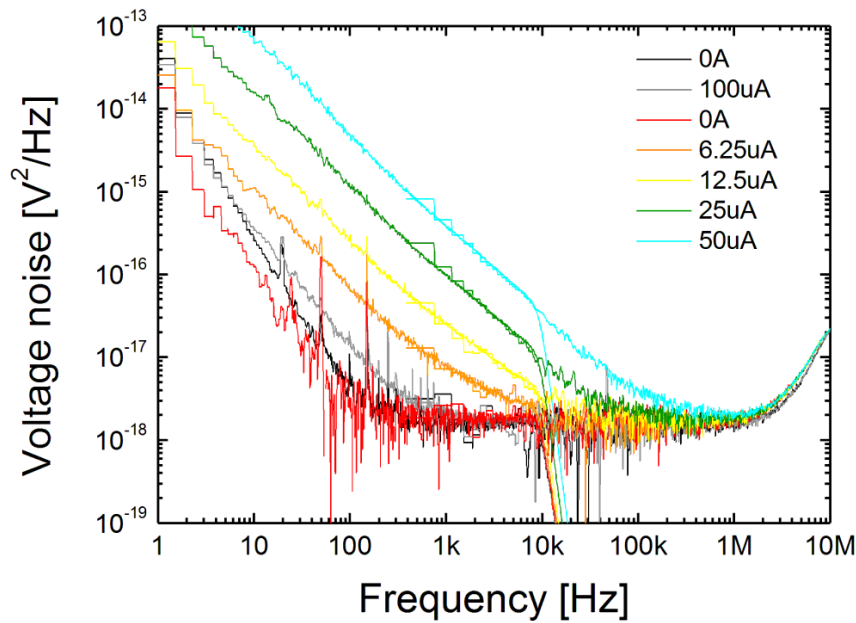


Figure 5.26: 100Ω MTJ device C2-2, measured noise whit and without applied magnetic field

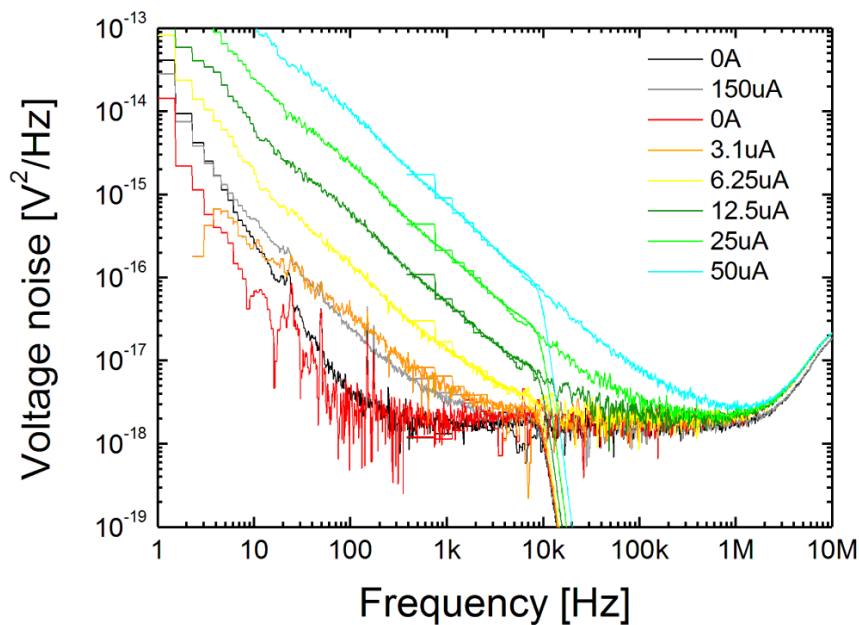


Figure 5.27: 100Ω MTJ device C2-5, measured noise whit and without applied magnetic field

The results of three device of the same array are shown in figures 5.25, 5.26, 5.27; at each current value two measures where made, one at high frequencies and another one at low frequencies with low-pass filters enabled, they have been graphically overlapped to create a smooth conjunction between them; coloured lines are whit magnetic field, dark and grey without. The effect of applied magnetic field is a strong increase of 1/f noise that grows in good agreement with the equation 5.15. In conclusion the maximum sensitivity zone, obtained by an external magnetic bias field, unfortunately correspond to the maximum value of 1/f noise of magnetic origin; these results are of primary importance for the design of a lock-in amplifier based on these devices.

Chapter 6

Low-frequency noise in P3HT fibers O-Fet

A lot of solid-state electronic applications have already been revolutionized due to the low-cost, solution-based processing and flexibility of organic semiconductors; however many fundamental issues related to charge-carrier transport in conjugated materials are still not completely understood, especially in devices with strongly reduced dimensions. For instance, low-frequency noise is inherently and ubiquitously present in electronics, but the way it changes upon moving from bulk crystal conducting media to nanostructures is still poorly investigated. In fact, such flicker ($1/f$) noise becomes more and more significant in devices approaching nanoscale, thus being an important factor which limits their performance. Furthermore, being very sensitive to variations of ambient conditions and to external contaminations, it can be also exploited as probe mechanism in sensing applications. For these reasons, studying the behavior of flicker noise in nanostructures such as polymer nanofibers has both fundamental and technological interest.

This chapter is focused on the use of the cross-correlation spectrum analyzer to investigate the flicker noise in two different types of organic field-effect transistors (OFETs) based on P3HT: in one type the active material is organized as conductive polymer nanofibers, in the other the P3HT is in the form of a thin film. The noise in the devices, working in accumulation regime in air conditions, is well described by the Hooge empirical model, which suggests a behavior dominated by mobility fluctuations. Importantly, the Hooge constant, α_H describing the current power spectral density of fluctuations, is suppressed by at least one order of magnitude in the device based on nanofibers, with respect to thin film devices fabricated using the same organic material.

Polymer nanofibers and other similar nanostructures generally exhibit a charge-carrier mobility significantly enhanced with respect to thin films made of the same material due to a more ordered molecular arrangement. These nanostructures can be produced by a variety of methods including electrospinning and soft lithography, all of them leading to an improvement of device behavior compared to OFETs based on thin films.

6.1 Structure of Ofet based on P3HT nanofibers

Polymer nanofibers for this study are realized by a solvent-assisted micromolding method. Ofet devices are fabricated by a bottom-contact architecture, with a n-doped Si substrate as common gate electrode, a 100 nm-thick thermally-grown SiO₂ dielectric, and lithographically-defined Cr/Au electrodes as source (*S*) and drain (*D*). The channel width (*W*) is varied between 100 μm and about 3 mm, and the length (*L*) is varied between 6 μm and 25 μm . Dimethyldichlorosilane (DMDS) is deposited prior to nanofibers, in order to improve the semiconductor/dielectrics interface. Quartz masters made by electron-beam lithography and reactive ion etching are used for molding elastomeric replicas made of PDMS. Organic nanofibers are then produced by depositing on the devices a 1 μL droplet of a 0.2 mM dichlorobenzene solution of regioregular P3HT, and positioning the PDMS molds on top, with features along the D-S gap, until complete solvent evaporation. The resulting conductive fibers connect source and drain, show a diameter around 300 nm and are arranged in an array with period of 1 μm . Figure 6.1 is an image by optical microscope showing the buried contact pads and overlying fibers. For comparison, P3HT thin film OFETs are realized by spin-coating (1000 rpm for 60 s) the same solution on the same SiO₂ / electrodes structure. Also the active medium in these devices has a thickness of 300 nm.

The field effect mobility, μ , is determined by the device characteristics equation 6.1 where *C* is the gate dielectric capacitance per unit area, *L* is the channel length and Z_{eff} is the effective channel width, which in nanofiber-OFET is given by the width of each single nanostructure times the number of D-S connecting fiber. Devices based on nanofibers exhibit a quite stable value of the mobility, $\mu = 10^{-2} \text{cm}^2 \text{V}^{-1} \text{s}^{-1}$ while thin film OFETs show instead a value which is strongly variable in the range $\mu = 2 \cdot 10^{-3} \leftrightarrow 10^{-5} [\text{cm}^2 \text{V}^{-1} \text{s}^{-1}]$ depending on the specific device geometry and preparation conditions.

$$I_{DS} = \frac{Z_{eff}}{2L} C \mu (V_{GS} - V_{TH})^2 \quad (6.1)$$

The source-drain current I_{DS} dependence on the source-drain voltage V_{SD} , reported in figure 6.2(a) and 6.2(b), highlights in all the devices the typical p-type behavior of P3HT-based OFETs, working in accumulation mode. In nanofiber devices is observable a non complete current saturation at high V_{DS} . Such effect is usually due to residual impurities from device processing which lead to increased hole density in the transistor channel. Related to this, V_{TH} has positive values (9V and 4V for nanofiber and thin film OFET, respectively), which also suggests the presence of intrinsic accumulated holes in the conduction channel. The corresponding transfer characteristics, $I_{DS}(V_{GS})$ and $|I_{DS}|^{1/2}(V_{GS})$ curves (for $V_{DS} = -50\text{V}$) for nanofibers and thin film devices are shown in 6.2(a) and 6.2(b), respectively.

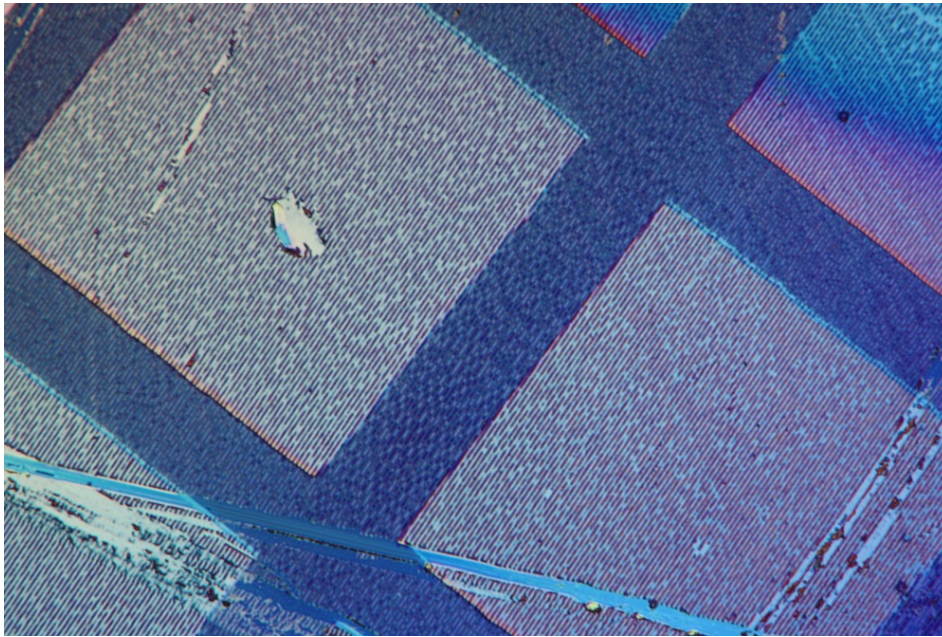


Figure 6.1: Ofet based on P3HT nanofibers imaged by an optical microscope: buried electrode contacts are clearly visible under the active nanofibers layer with scratches caused by contact probe tips.

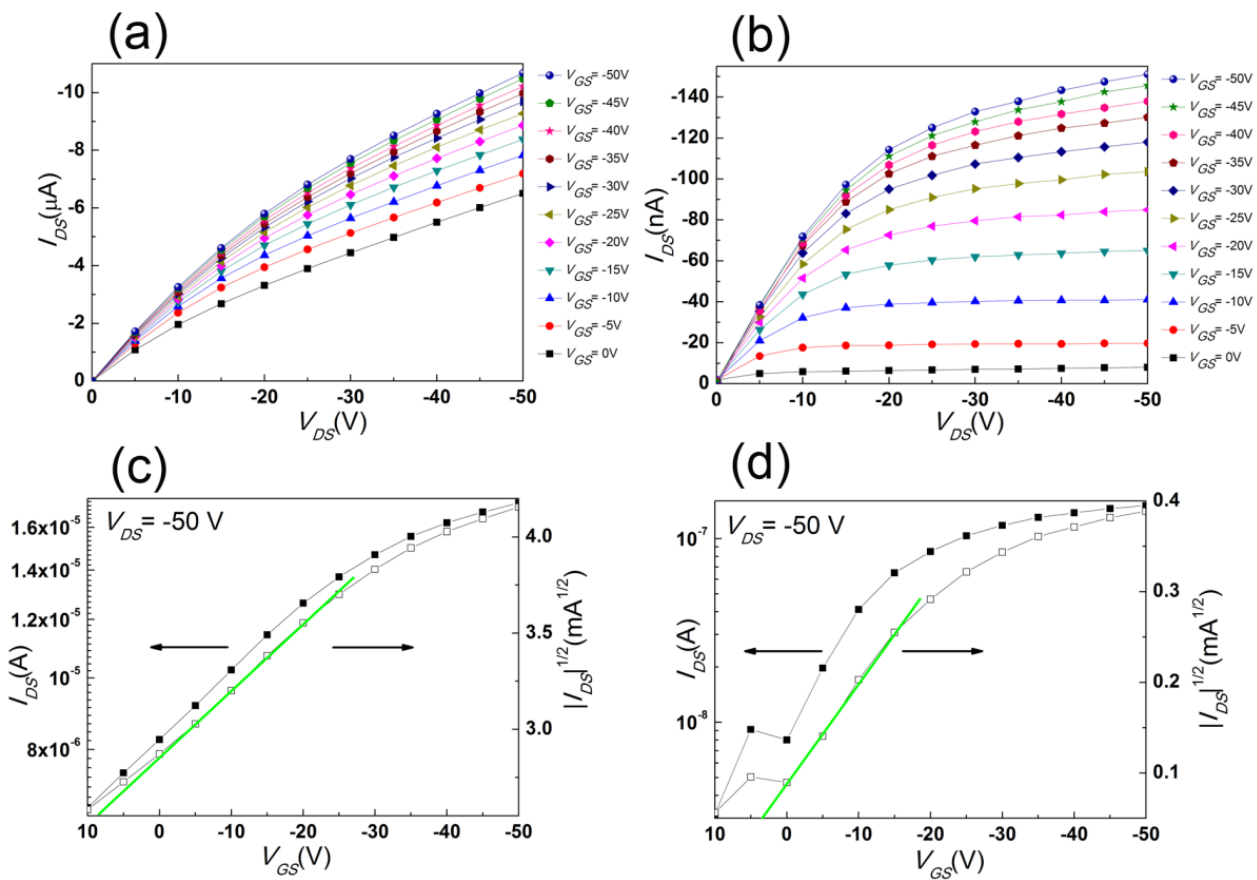


Figure 6.2: Output characteristics of OFETs based on polymer nanofibers (a) and thin films (b). Channel length $L = 12 \mu\text{m}$ for both structures. (c, d) Are the corresponding transfer characteristics $I_{DS}(V_{GS})$ (left vertical scale) and $|I_{DS}|^{1/2}(V_{GS})$ (right vertical scale) for a fixed $V_{DS} = -50\text{V}$. Continuous lines are linear fits of data.

6.2 Integrator-Differentiator cascade amplifier

The first choice to perform noise measurement on ofet devices is a current mode front-end made by a transimpedance stage for each channel, as the one showed in figure 1.3. Is useful to reassume here the structure of a simple single-channel transimpedance stage figure[6.3] to point out its design constraints.

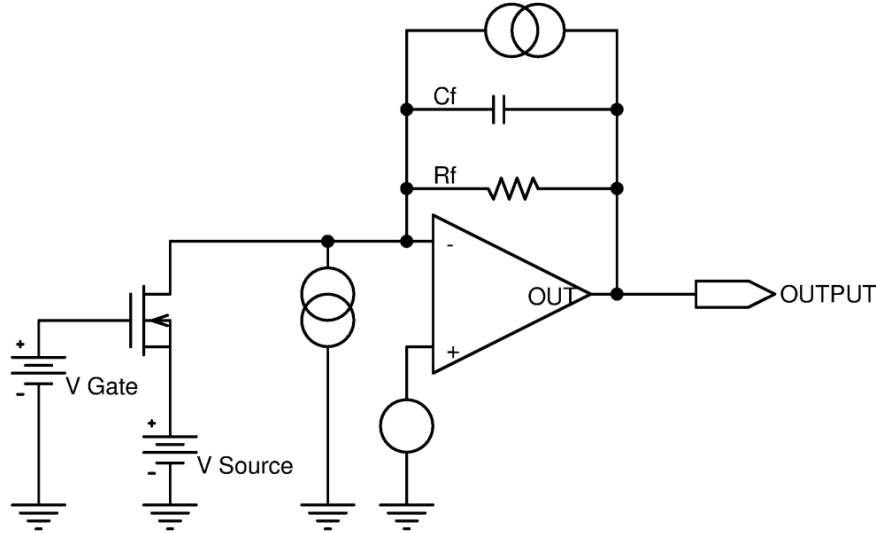


Figure 6.3: Single stage transimpedance amplifier

The transimpedance gain is a single pole low-pass function

$$\begin{aligned} G_{LF} &= R_f \\ f_p &= \frac{1}{2\pi C_f \cdot R_f} \end{aligned} \quad (6.2)$$

Input equivalent current noise is the sum of three different contribute from the opamp and feedback resistor

$$\overline{i_{n,in-eq}^2} = \frac{\overline{e_n^2}}{R_f^2} + \overline{i_n^2} + \frac{4KT}{R_f} \quad (6.3)$$

And there is an upper limit for the feedback resistor's value since it have to supply the dut's bias current.

$$I_{BIAS} \cdot R_f \leq V_{OUT,MAX} \quad (6.4)$$

The feedback resistor R_f is present in all three equations, therefore its choice is a trade-off between noise, bandwidth and bias current constraints. The ideal amplifier for this configuration would be a fet-input operational amplifier with very low current noise $\overline{i_{n,in-eq}^2} \cong fA/\sqrt{Hz}$ to reduce the overall uncorrelated noise and therefore the measurement time. Consequently the feedback resistor value must be at least in the range of hundreds of $M\Omega$ to keep its noise contribute in the same range of that of the amplifier. Is at this point that emerges the bandwidth problem of this configuration: even the smallest resistor, smd package 0402, have a parallel parasitic capacitance of $C_p \cong 1pF$, almost entirely created by the package itself and independent from the resistor value; this one act in fact as the C_f capacitor in the circuit of figure 6.3 and even for a relatively small $R_f = 100M\Omega$ it creates a pole of $f_p \cong 1.6kHz$ that is too low to make good characterization of the ofet devices. To overcome this problem an alternative amplifier topology is used, the integrator-differentiator cascade transimpedance

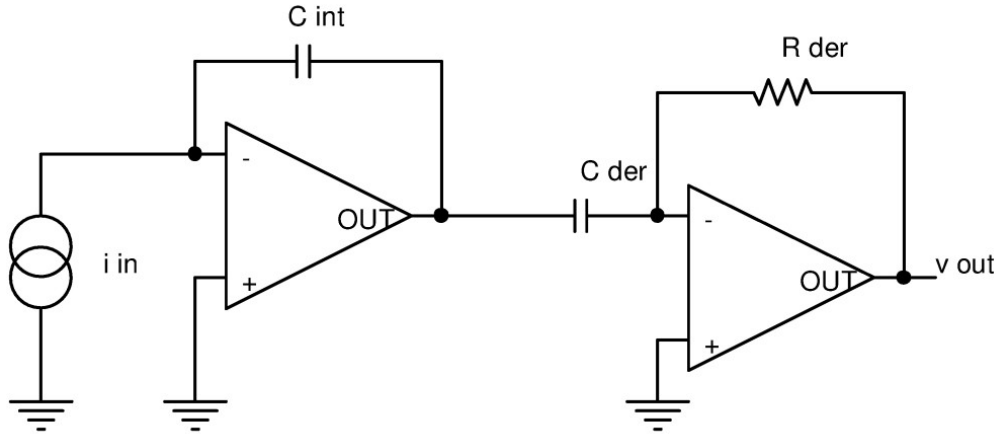


Figure 6.4: Ideal integrator - differentiator cascade transimpedance amplifier

amplifier [18], whose basic structure is shown in figure6.4 It is made by an ideal integrator followed by an ideal differentiator, able to create flat constant gain over frequencies without the use of a feedback resistor connected at the input, therefore eliminates the trade-off between noise and bandwidth. The output voltage can be calculated as follows

$$v_{out} = (-)i_{in} \left[\frac{1}{SC_{int}} \right] \cdot (-) [R_{der}SC_{der}] \quad (6.5)$$

and the gain consequently is

$$Gain = R_{der} \cdot \frac{C_{der}}{C_{int}} \quad (6.6)$$

The noise of the differentiator stage can be made negligible by considering that the contribution of the resistance R_{der} is reduced by the factor $(C_{der}/C_{int})^2$. The consequent possibility to strongly reduce the R_{der} value has the positive effect of extending the bandwidth of the overall transimpedance amplifier to almost the gain-bandwidth product of the used opamp. This ideal circuit is the starting point for the design of the front-end specific for noise measure of ofet devices.

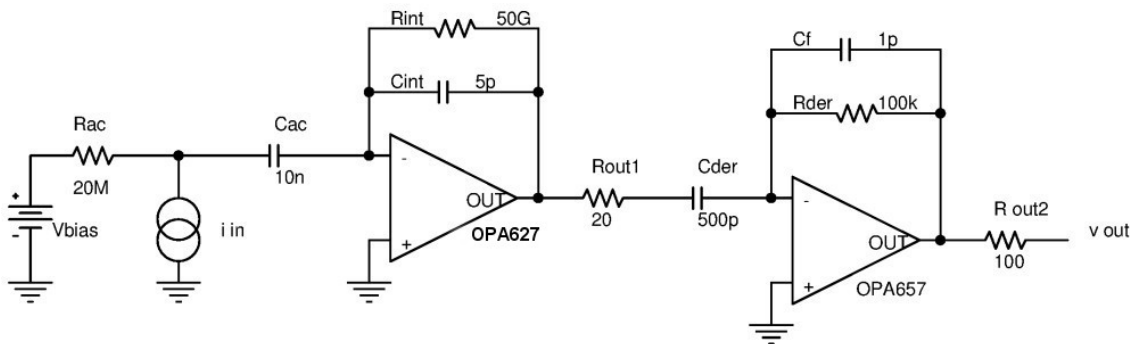


Figure 6.5: Complete structure of integrator-differentiator amplifier used in each channel of the realized front-end

6.3 Design of the front-end for Ofet devices

The integrator stage is made around the OPA627, a fet-input internally compensated operational amplifier, with 16MHz of GBWP and $2.5fA/\sqrt{Hz}$ of input equivalent current noise. To avoid saturation of the integrator a path must be created for the input bias current at the non-inverting input of the opamp used as integrator. There are various possibility to solve this issue using another ideal integrator as additional feedback loop or active devices in sub-threshold region [16][17]; considering the ofet's measurements requirements the most simple and effective solution is to add a resistor R_{int} in parallel to the feedback capacitor C_{int} to create what is commonly called a *real integrator*. The resulting pole at $f_p = \frac{1}{2\pi C_{int} \cdot R_{int}}$ constitutes the lower frequency limit for the overall transimpedance stage, so the R_{int} value must be high enough to meet this requirement and to not add significant noise at the integrator's input. The chosen $R_{int} = 50M\Omega$ and $C_{int} = 5pF$ create a ideal gain pole at $f_p \cong 637mHz$ adding only $0.5fA/\sqrt{Hz}$ of current noise at the input. The high bias voltages required by ofets, up to 50V, prevents a direct connection between them and the amplifier input, and consequently is not possible to bias it directly by applying the bias voltage at the non inverting input of the integrator opamp. Therefore there is a network, consists of $R_{ac} = 20M\Omega$ and $C_{ac} = 10nF$, to ac-couple the device to the transimpedance input. The high voltage generator V_{bias} is schematically represented by a simple battery and it will be explained later in detail. Additional resistor R_{out1} improve the stability of the integrator by adding a zero in the G_{loop} which is affected by the pole generated by the C_{der} capacitor and the open loop output resistance of the OPA627. All the poles and zeros of the G_{loop} are reported in table 6.1

Singularity	Origin	Value
$fp, 1$	$C_{ac}R_i$	$318\mu Hz$
$fz, 1$	C_iR_i	$637mHz$
$fz, 2$	$C_{ac}R_{ac}$	$1.25Hz$
fp_{OA}	OPA627	$15Hz$
$fp, 2$	C_iR_{ac}	$1.6kHz$
fp, out	$C_{der}(R_{out1} + R_0)$	$4.25MHz$
fz, out	$C_{der}R_{out1}$	$15.9MHz$

Table 6.1: Integrator G_{LOOP} poles and zeros

The differentiator is made around the opa657 operational amplifier. The R_{out1} resistor contributes also to the stability of the differentiator stage by adding a zero in its G_{LOOP} . The parasite capacitor of R_{der} is represented by $C_f = 1pF$. The resistor R_{out2} improve the stability of the differentiator acting in the same way of R_{out1} for the integrator stage; for the differentiator the load capacitance comes from the mainboard's input stage and interconnection connector between the two boards; it can be estimated of 15pF. Poles and zeros of the differentiator's G_{loop} are reported in table 6.2

Overall the circuit synthesizes a transimpedance gain from dut's input current i_{in} of $G = v_{out}/i_{in} = 10M\Omega$ flat from 0.6Hz to 1.75MHz. The lower frequency limit is due to the ac coupling created by R_{ac}, C_{ac} while the upper frequency limit is due to the bandwidth limits of the used operational amplifier. The complete amplifier of each acquisition channel is show in figure 6.5.

The complete front-end circuit is shown in figure 6.6 where are evident the two transimpedance channels based on the integrator-differentiator cascade and the high voltage coupling networks made by the two C_{ac} and R_{ac} . The bias network is made by a high voltage generator, connected

Singularity	Origin	Value
$fp, 1$	$C_{der}R_{der}$	$3, 18kHz$
fp_{OA}	$OPA657$	$300kHz$
$fz, 1$	C_fR_{der}	$1.6MHz$
$fz, 2$	$C_{der}R_{out1}$	$15.9MHz$
$fp, 2$	C_fR_{out1}	$7.9GHz$

Table 6.2: Differentiator G_{LOOP} poles and zeros

by an auxiliary bnc connector to the mainboard, and the two R_{ac} resistor which act as current limiters as well as ac coupling network. To reduce the noise from the voltage generator a low-pass RC filter made by R_{bias} and C_{bias} is placed after the generator. To measure the bias current a shunt resistor is placed at the end of the bias network chain; it is read by a simple voltage amplifier in non-inverting configuration. The gate bias comes from an RC network that act as a low-pass filter for the DC voltage generator, preventing its noise from driving the gate. When a relay is possible to disconnect C_{gate} from ground and connect it to the mainboard noise generator, therefore the $R_{gate}C_{gate}$ network act as an high pass filter for the input signal V_{in} and low pass filter for GATE BIAS dc voltage: this makes possible to measure the device's transconductance g_m by calculating the ratio between the input signal at the gate and the device current read by the two main amplifiers. Two additional $1k\Omega$ trimmers are placed just after the external generators input to allow fine tuning or the use of a fixed less noisy voltage generator, such a series of low voltage battery. Typically ofets exhibit a small transconductance g_m and almost equal impedance from both source and drain terminals: this common trait allows to avoid the use of a network to increase the input impedance seen from the source as the one showed in section 4.0.3. All the passive in the overall bias network are discrete through-hole components which are not directly soldered to the pcb but placed on sockets, to allow easy replacement, depending on the device characteristics and bias requirements.

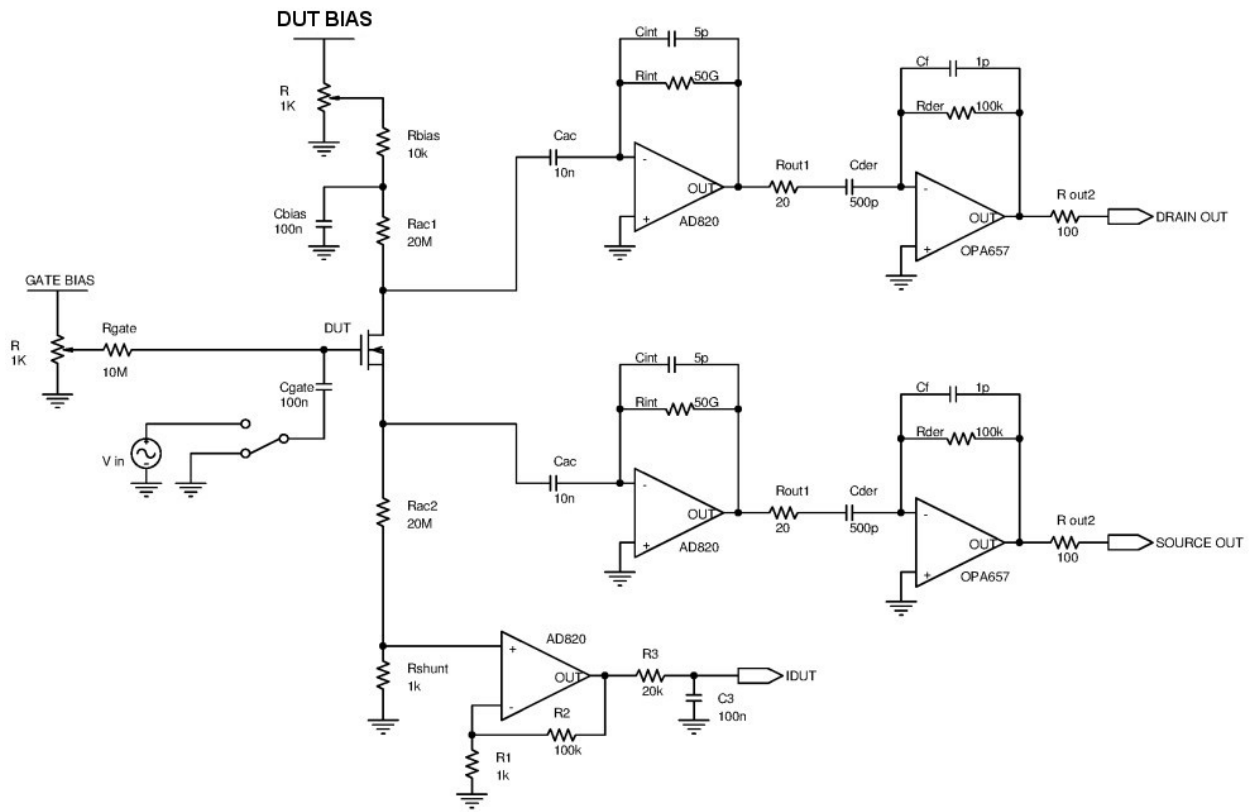


Figure 6.6: Complete circuit of the front-end for OFet devices noise measure

6.4 Ofet with P3HT active fibers above contact pads

The first batch of ofet samples available for measurement are based on P3HT fibers structure placed above the conductive metal pads which act as drain and source contacts. The device is shown in figure 6.7

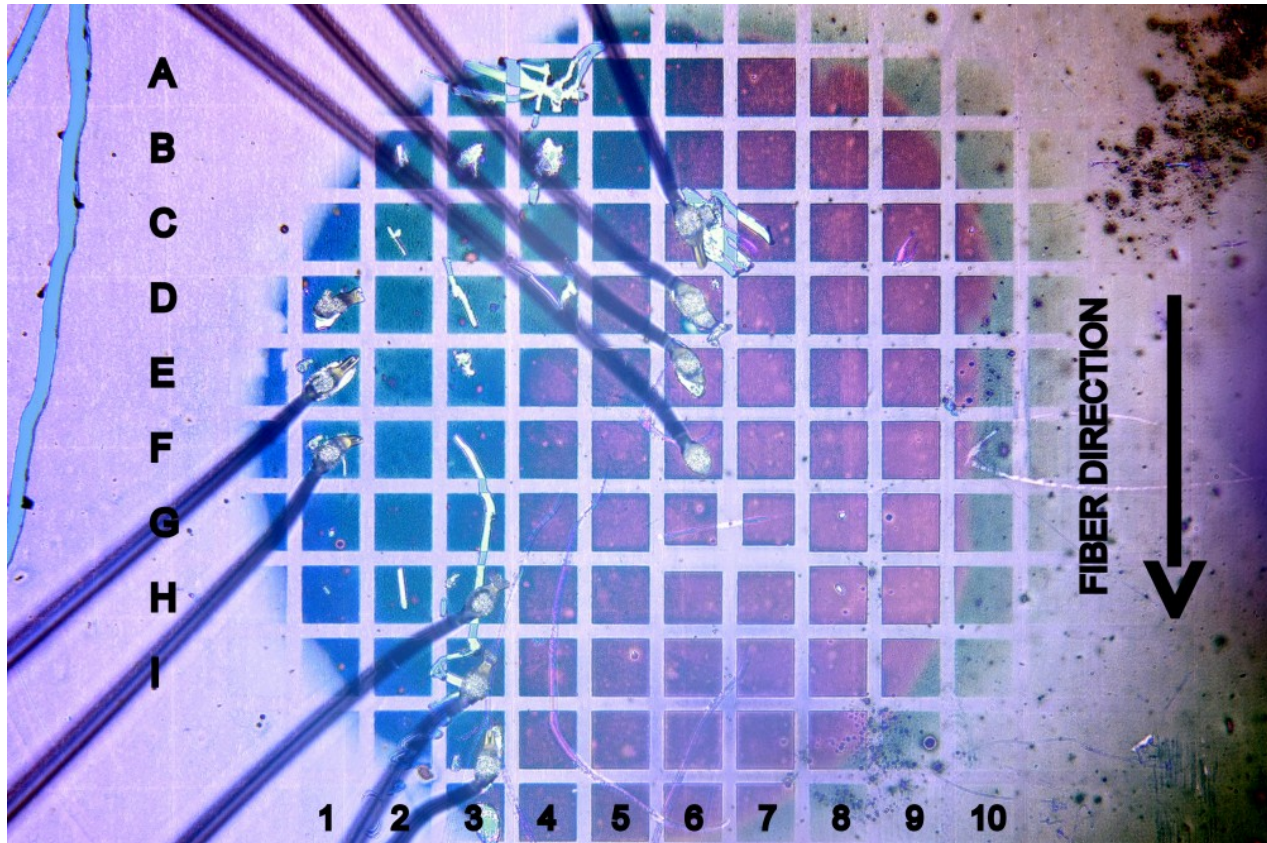


Figure 6.7: Optical microscope photograph of the Ofet with P3HT active fibers above contact pads

The first method to contact this two terminals was the use of a probe station with sharp needles able to pierce the layer of active fibers and reach the buried metal pads. As expected the main drawback of this solution is the high sensitivity to electromagnetic interferences. Furthermore sometimes the electric contact was not stable enough to allow a complete measurement set of around 90 seconds for each bias voltage. Later was decided to try to bond the device on a standard semiconductor chip carrier and place this assembly inside the instrument. This technique has proved very difficult due to the active organic P3HT layer placed on top of the contact metallic pad: the bonding machine head must scratch this layer to being able to join the wire to the contact pad. Often this operation create damages to the pad or to the active layer between them, but a more delicate approach causes bad contact or no contact at all. At the end about half of the attempts seems successful at a visual inspection.

In the following two paragraphs are reported the measures made on two different source-drain couples, the $4AB$ contacted by the probe station and $1EF$ by the bonding wires. Various set of measures are taken, maintaining a fixed nominal gate bias voltage and changing the dut's current acting on the external generator of figure 6.6

All measure are taken with the instrument's internal LPF stages activated. At the end of the measurement session was observed a leakage gate current, with values up to 100nA. Since

the gate is biased by a RC network, this implies a unknown change, up to some volts, in the effective bias voltage at the dut's gate. Since this effect was observed only at the end of the session, all the following measures reports only the nominal gate bias voltage.

Measure with probe station (device 4AB)

Gate nominal bias voltage: 0V

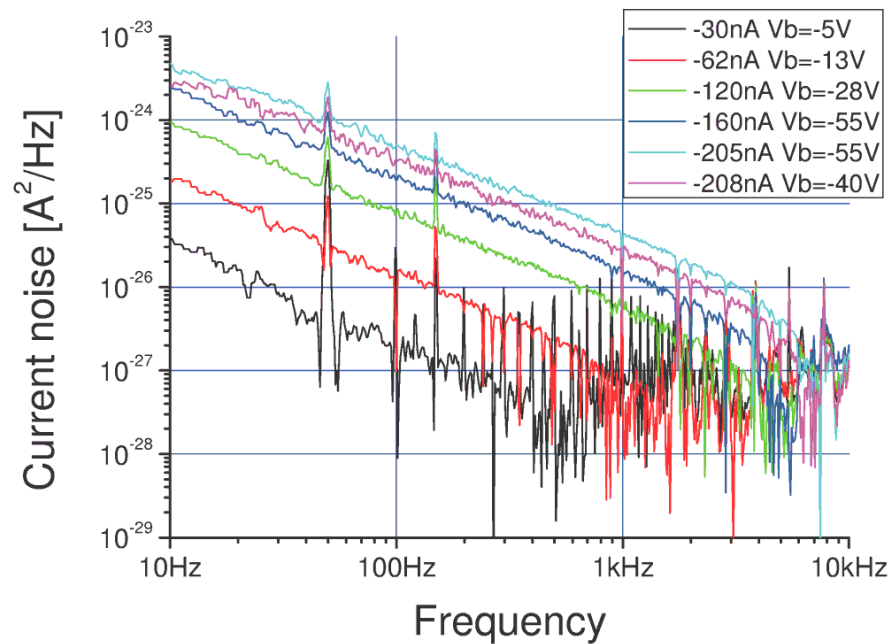


Figure 6.8: Ofet device contacted with the probe station at $V_G = 0V$: measured channel noise current

The device show only $1/f^a$ noise, with $a \cong 1.1$. As the frequency increases the measures converge to a limit value determined by the experimental setup. There are numerous peaked interferences caused by the long probe cables which act as an antenna, expecially evident at low bias current. The device shows a high drift of the bias current (the blue and cyan lines are separated by ten minutes of time delay with the same bias condition applied) and a noticeable hysteresis (the pink and cyan lines show about the same current and noise spectra, despite the 15V change in applied bias voltage); this hysteresis effect is evident in figure 6.9 where the measured source current is plotted against the source-drain bias voltage.

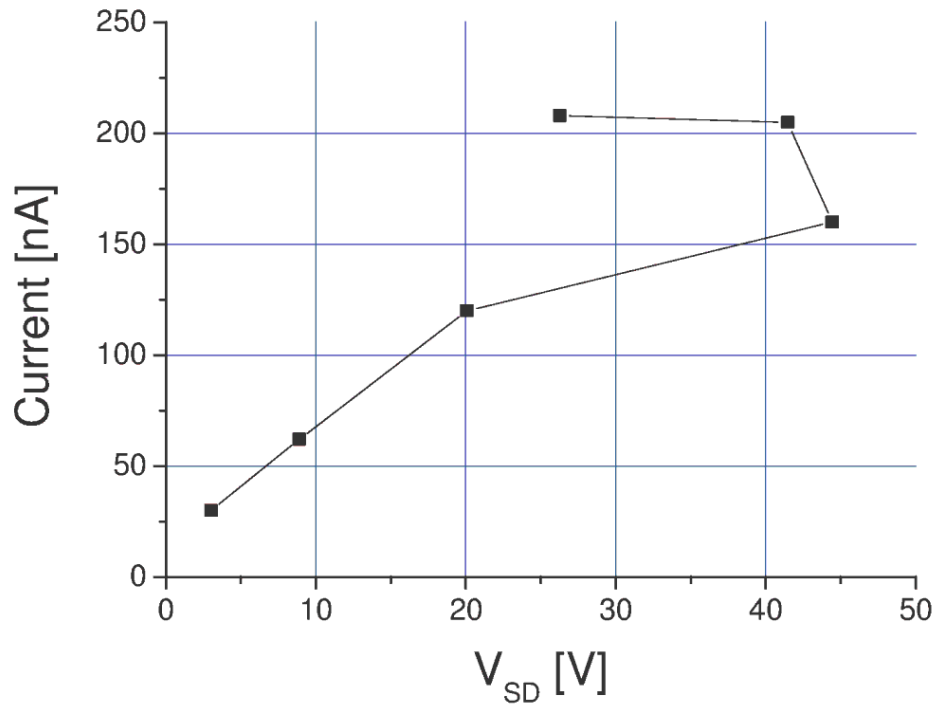


Figure 6.9: Ofet device contacted with the probe station at $V_G = 0V$: measured source current against source-drain bias voltage

Figure 6.10 represent the noise sampled at a fixed frequency (90Hz): there is a cubic dependence on the applied bias current.

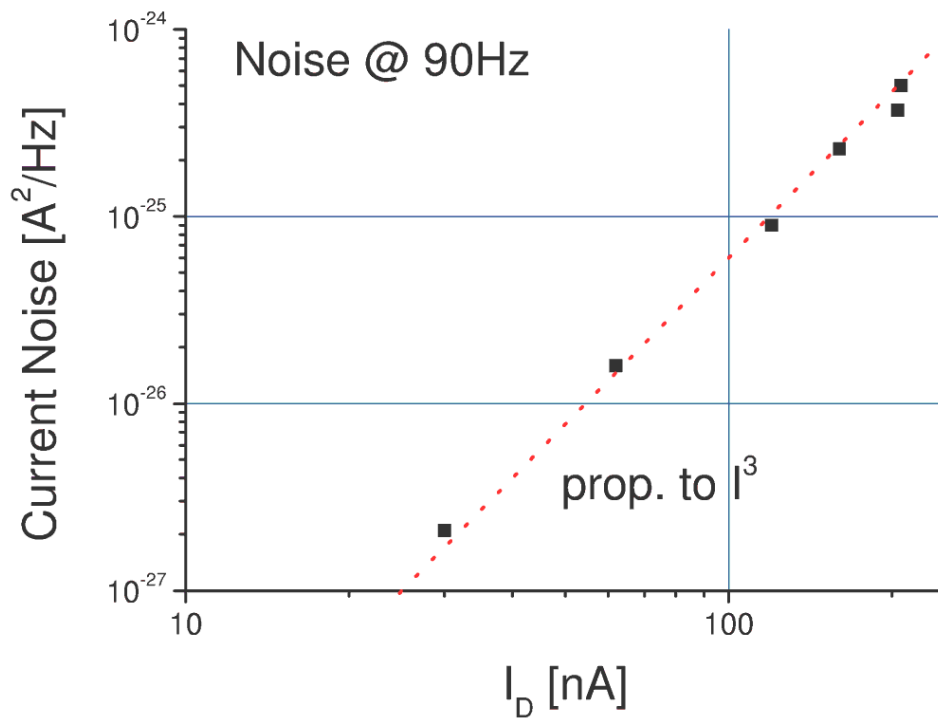


Figure 6.10: Ofet device contacted with the probe station at $V_G = 0V$: noise evaluated at 90Hz (black dots) and the interpolation line (red dots)

Gate nominal bias voltage: $-25V$

To emphasize hysteresis effect the measures at $-25V$ was splitted in two different set: the first one increasing the bias voltage from $0V$ to $-50V$, then the second one returning to zero; the hysteresis is evident in figure 6.13 where the measured bias current is plotted against the applied bias voltage. The two red arrows highlight the increase and decrease of applied bias voltage. Due to the high (up to $100nA$) gate leakage current, divided in two components gate-drain and gate-source, the effective source-drain bias voltage becomes apparently negative. Since the dut's current was measured at the source terminal is not possible to determine the exact drain current; one possible explanation of the effect is that the effective true device's drain current is a sum of the measured source current and the gate-drain leakage current estimated of around $40nA$ at $V_b=0V$; consequently the actual drain bias voltage is lower than predicted due to the voltage drop on R_{ac1} ac coupling resistor of scheme 6.6. This additional voltage drop consequently increases with increasing applied bias voltage V_b .

The acquired noise spectra are shown respectively in figures 6.11 and 6.12; figure 6.14 represent the noise current sampled at the fixed frequency of $90Hz$ where is evident a cubic dependence on the applied current bias level. In these three graphs is evident that the two measures at $V_b = 0V$ and $V_b = -0.8V$ are completely unreliable, due to unexplained contact instability at low bias currents.

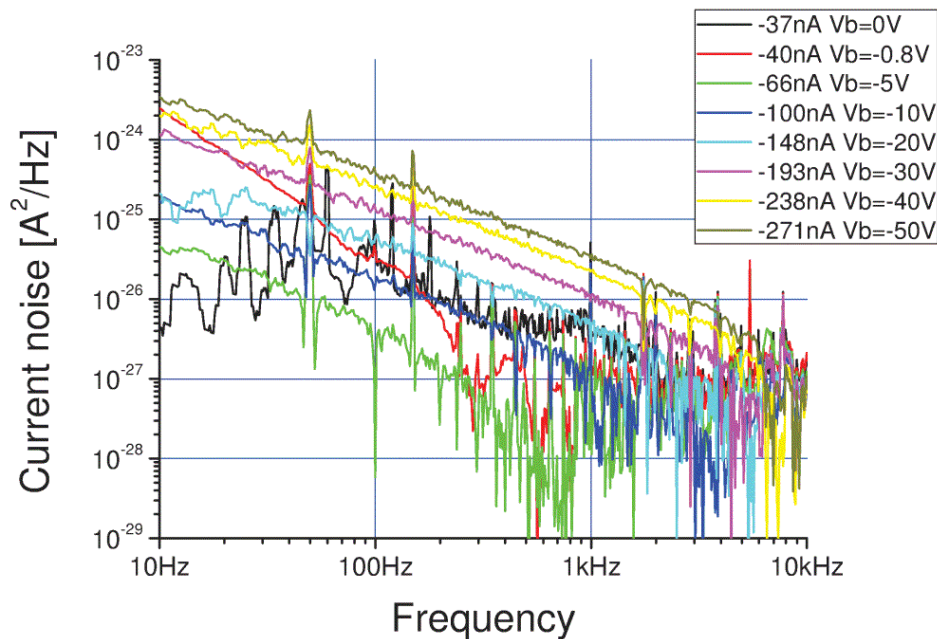


Figure 6.11: Ofet device contacted with the probe station at $V_G = -25V$: measured channel noise current for increasing bias voltage from $0V$ to $-50V$

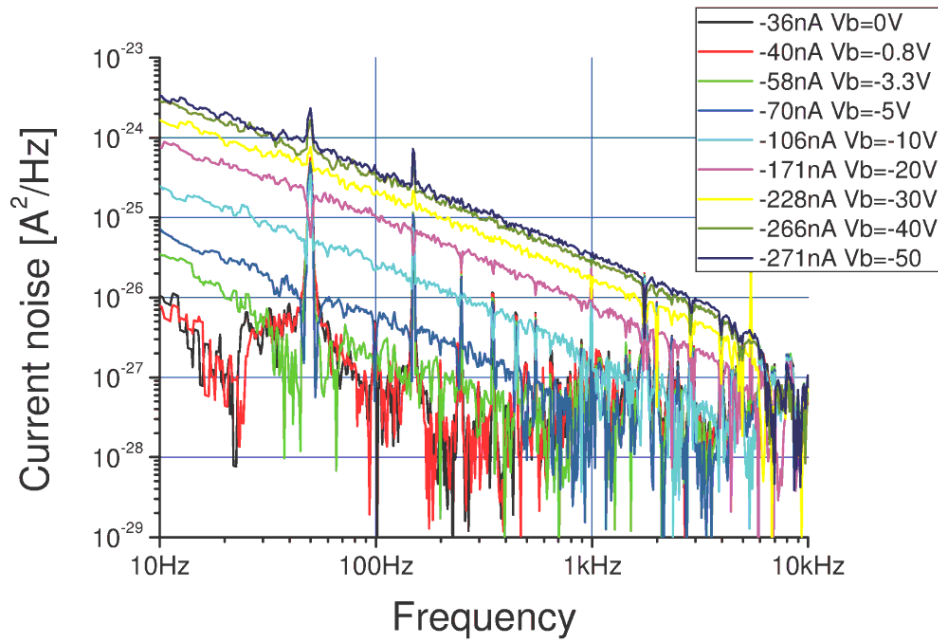


Figure 6.12: Ofet device contacted with the probe station at $V_G = -25V$: measured channel noise current for decreasing bias voltage from $-50V$ to $0V$

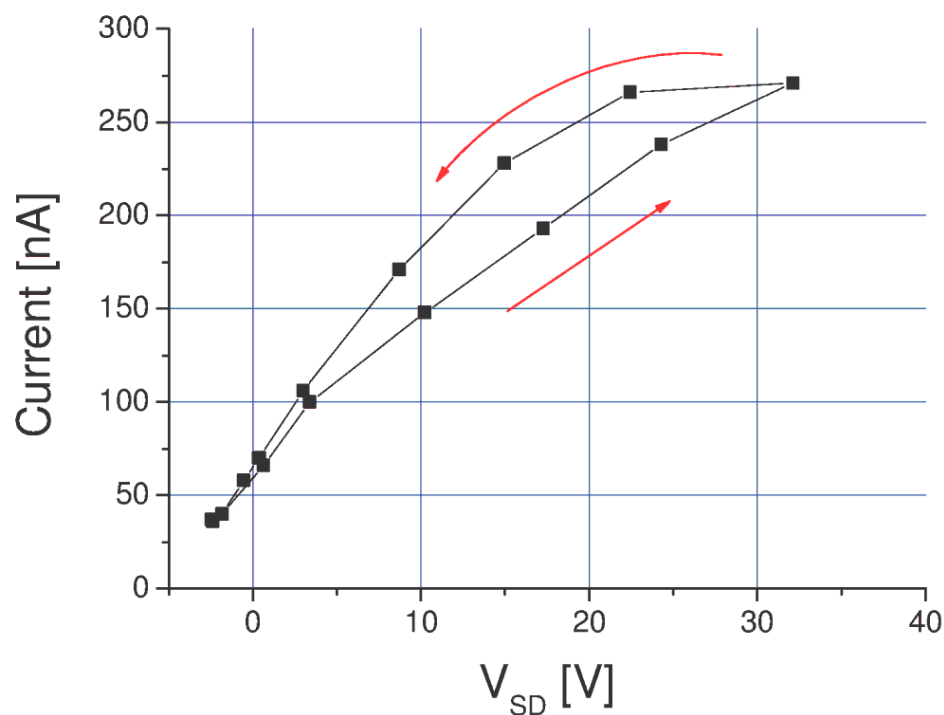


Figure 6.13: Ofet device contacted with the probe station at $V_G = -25V$: measured source current against source-drain bias voltage

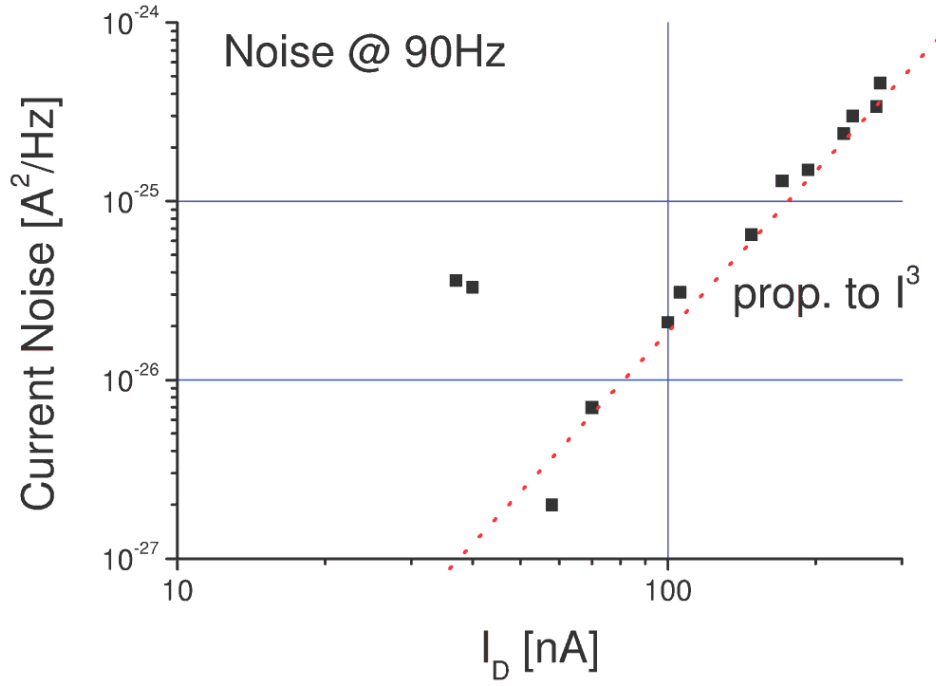


Figure 6.14: Ofet device contacted with the probe station at $V_G = -25V$: noise evaluated at 90Hz (black dots) and the interpolation line (red dots)

Measure with bonding wires (device 1EF)

Gate nominal bias voltage: 0V

To emphasize hysteresis effect the measures, as a result of the experience gained in the previous case, the measures was splitted in two different set: the first one increasing the bias voltage from 0V to -50V collected in figure 6.8, and then the second set of measure in figure 6.16 with bias voltage decreasing from -50V back to zero. The device contacted with bonding wires seems much more stable and reliable; specifically the noise measure at $I_{bias} = 0nA$ is in good agreement with the theoretical value of $10^{-28}A^2/Hz$ expected from a pure resistive $150M\Omega$ conductive channel, although the slight increase starting at 1kHz can not be easily explained. In the two measures at $I_{bias} = 0nA$ and $I_{bias} = 10nA$ there are still some electromagnetic interferences, for example it is clearly recognizable the 50Hz peak from the power network.

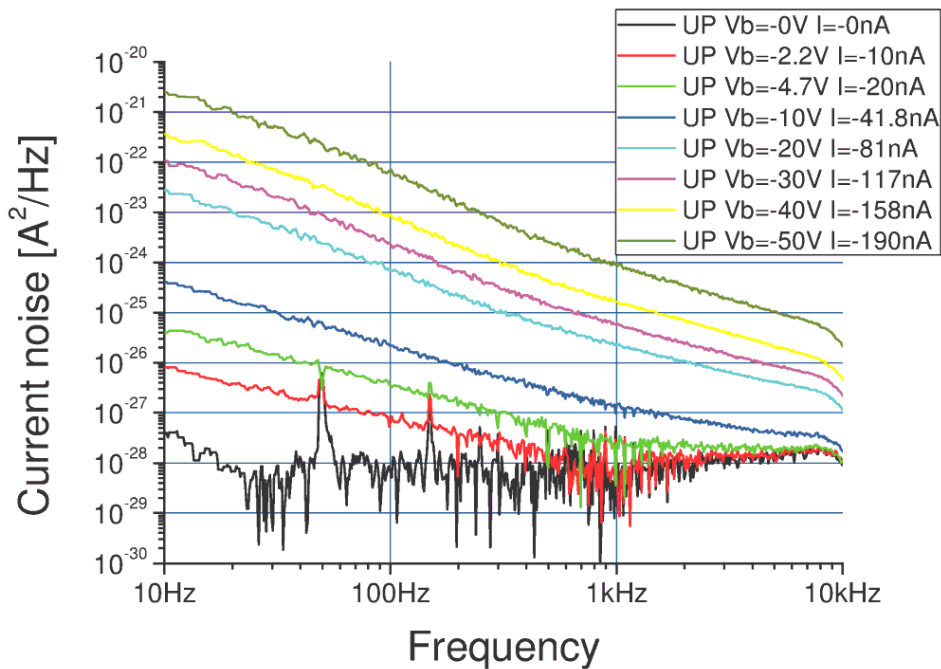


Figure 6.15: Ofet device contacted with bonding wires at $V_G = 0V$: measured channel noise current for increasing bias voltage from 0V to -50V

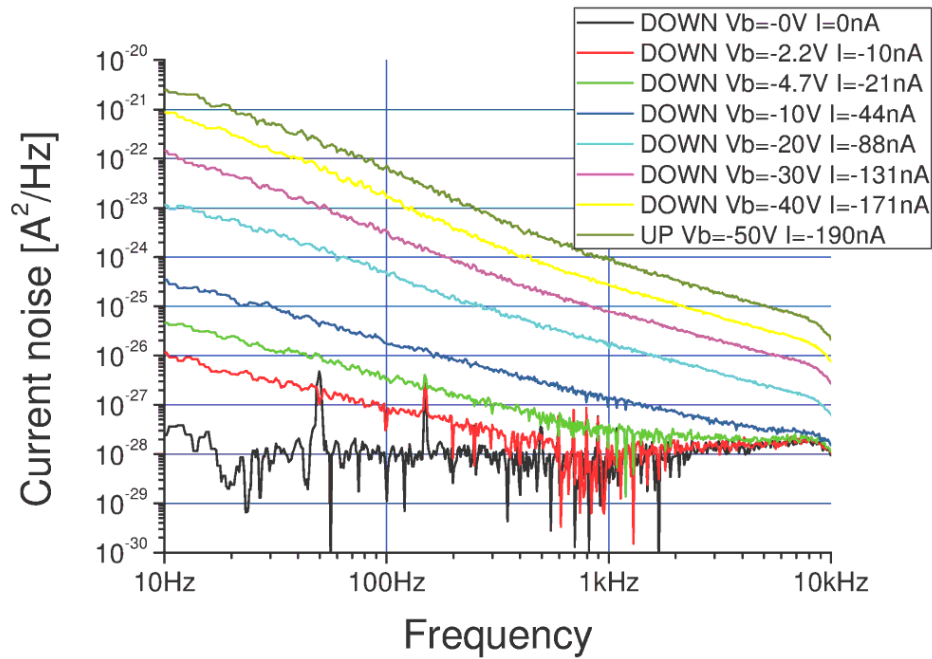


Figure 6.16: Ofet device contacted with bonding wires at $V_G = 0V$: measured channel noise current for decreasing bias voltage from $-50V$ to $0V$

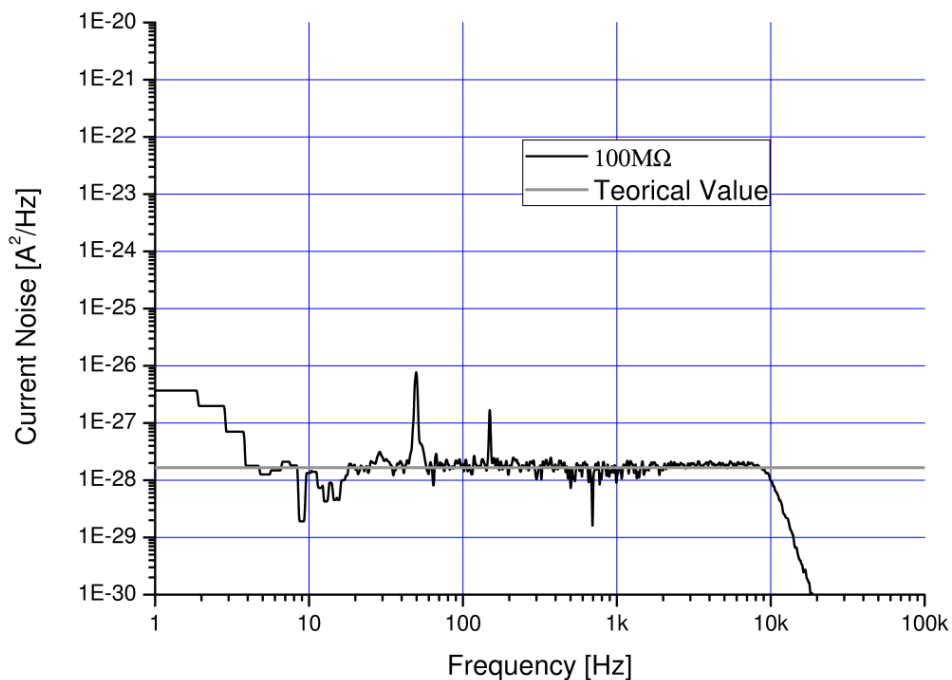


Figure 6.17: Current Noise density of a $100M\Omega$ resistor: measured and theoretical value

The hysteresis is evident in figure 6.18 where the measured bias current is plotted against the applied bias voltage. This device has a very linear $I_{bias} - V_{bias}$ characteristic with small modulation effect of the conductive channel and small hysteresis; in fact it behaves like a simple resistor of $R_{dut} \cong 220M\Omega$.

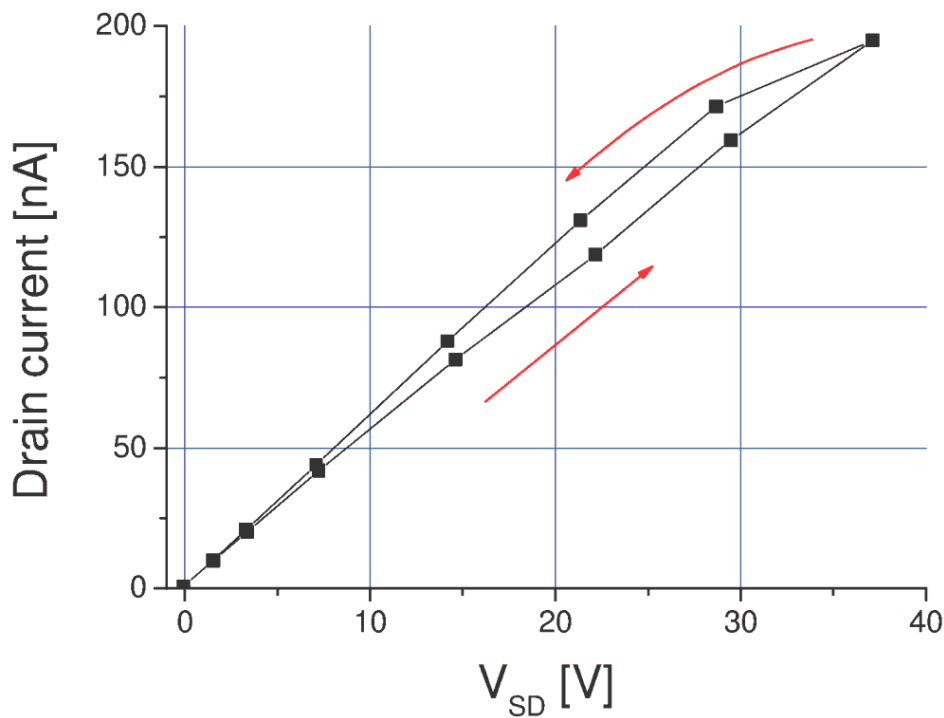


Figure 6.18: Ofet device contacted with the bonding wires: measured bias current is plotted against the applied bias voltage

Figure 6.19 represent the noise current sampled at two fixed frequency of 90Hz and 3kHz. Noise grows very steeply with increasing current, and does not follow a precise simple law.

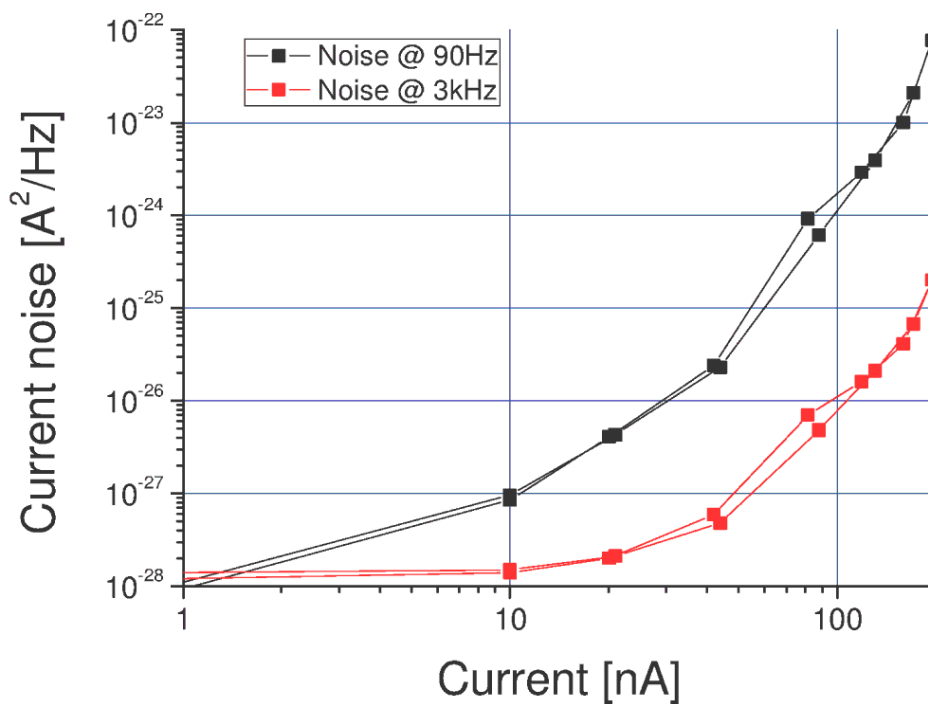


Figure 6.19: Ofet device contacted with the bonding wires at $V_G = 0V$: measured source current against source-drain bias voltage

6.5 Ofet with P3HT active fibers and free contact pads

The results of the first measurements have shown that the main problem were the pads covered by the active fibers layer: this prevents good contacts of bonding wires especially at low bias currents and the probe station has proved unreliable due to high level of electromagnetic interferences. To overcome these problems a new type of devices have been manufactured whit the contact pads free from the active fibers layer. This solution has shown clearly better performance: contacts with bonding wires seems very stable and no relevant leakage currents are observed; consequently the noise is detectable in a wider range of frequencies and all anomalous measurements have disappeared. A large number of different devices with different channel length, ranging from $6\mu\text{m}$ to $12\mu\text{m}$, have been measured. The following figures are relative to a device with $12\mu\text{m}$ channel length, measured at $V_{gs} = 0\text{V}$ and $V_{gs} = 40\text{V}$; the noise spectra were measured at different drain current by changing the drain-source voltage V_{DS} applied to the transistor ranging from 0V to -15V . At the equilibrium condition ($I_{DS} = 0$) the measured noise is in agreement with the calculated thermal noise produced by the drain-source channel resistance. As the drain-source current I_{DS} is increased the spectra show an excess noise that follows a $1/f$ frequency dependence.

In the acquired spectra, figures 6.20 and 6.21, the hatched area at high frequency highlights where the instrument's correlated noise is predominant and therefore the graph is not related to the true noise current of the device.

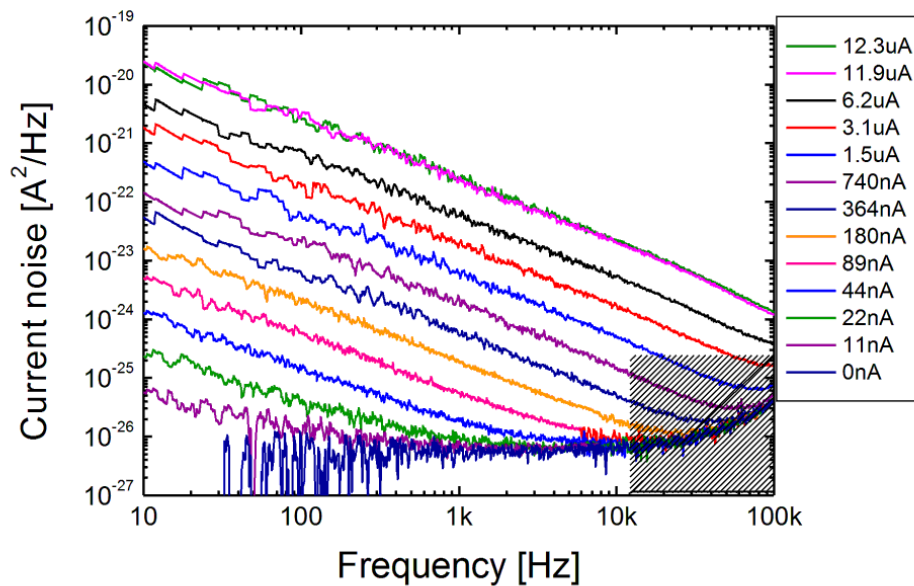


Figure 6.20: Current noise spectral density measured in a fiber FET with a channel length of $6\mu\text{m}$. Gate-source voltage is fixed at 0V and the drain-source voltage is ranged from 0V to -15V .

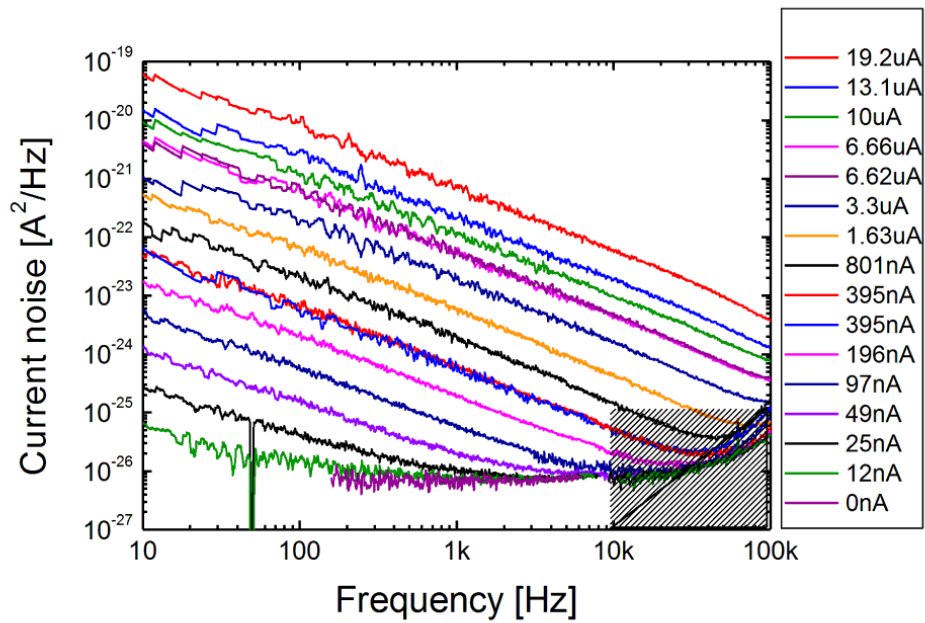


Figure 6.21: Current noise spectral density measured in a fiber FET with a channel length of $6\mu\text{m}$. Gate-source voltage is fixed at 40V and the drain-source voltage is ranged from 0V to -15V.

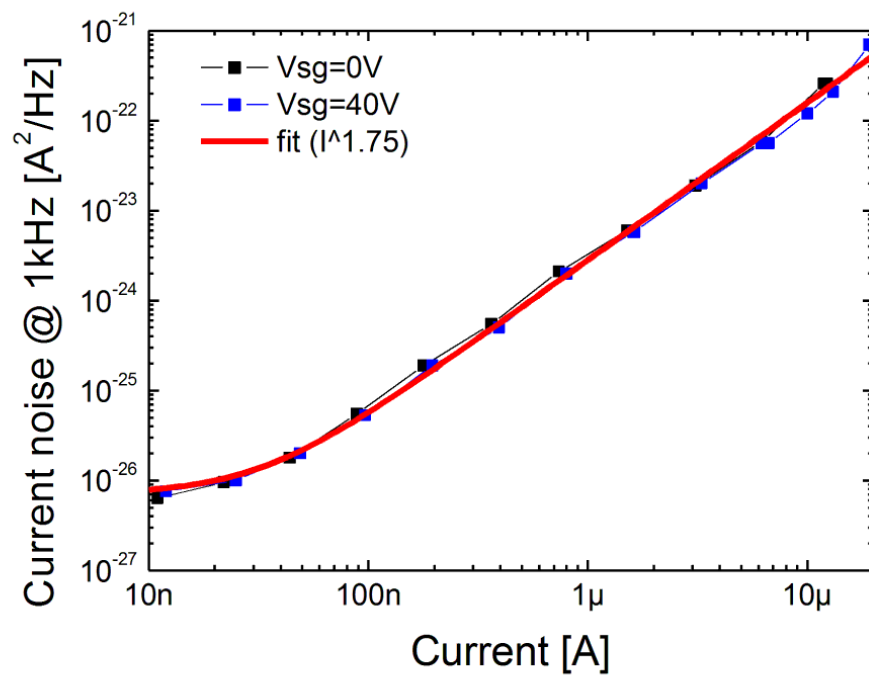


Figure 6.22: Current noise sampled at 1kHz plotted against bias current. Solid red line is the interpolating function

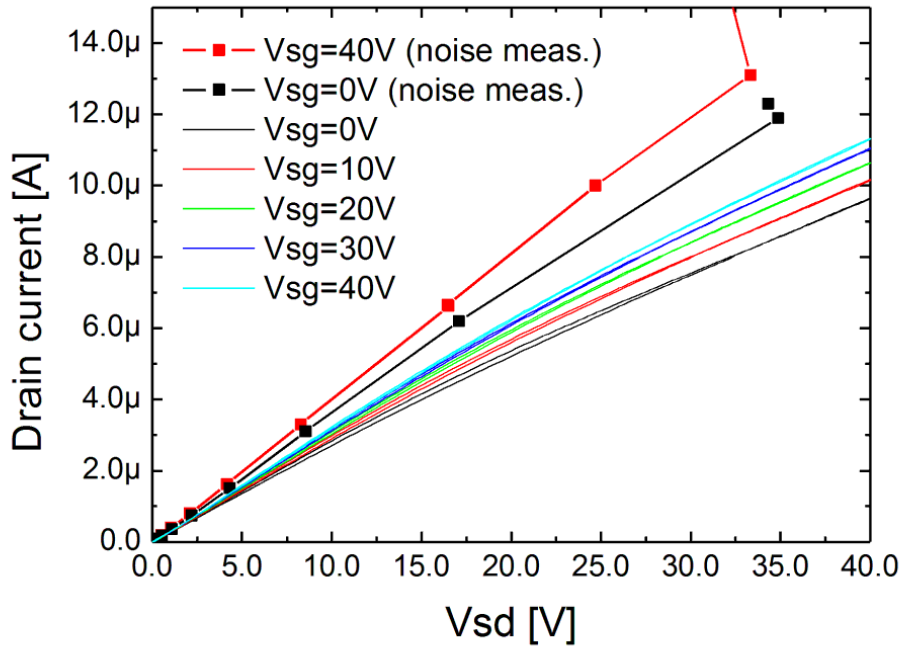


Figure 6.23: Device output characteristic obtained by a Keithley Semiconductor parameter Analyzer in comparison to the same measure obtained by the spectrum analyser during current noise measures

Overall more than 10 nanofiber-OFETs have been measured with this methodology: all of them showed an exponent β of $1/f^\beta$ between 1 and 1.1. For comparison the identical set of measurement was performed on a number of thin-film devices; figure 6.24 shows the results for one of these devices: the two graphs above are the acquired noise spectra, while the two below correspond to the acquired noise at 1kHz.

According to the empirical Hooge formula the $1/f$ noise of homogeneous samples can be expressed as

$$S_I = \frac{\alpha_H}{N \cdot f} \cdot I^2 \quad (6.7)$$

where N is the total number of free charge carriers in the sample, I the bias current and α_H is the Hooge's parameter. For transistors operating in linear regime this equation can be rewritten using quantities readily measurable as

$$S_I = \frac{e\mu\alpha_H}{L^2 \cdot f} \cdot V_{DS} \cdot I_{DS} \quad (6.8)$$

where e indicates the electronic charge. Figure 6.25 reports the nanofiber-ofet measured noise level at 1kHz normalized for the device length as a function of the power $V_{DS} \cdot I_{DS}$. The curves have a slope ranging from 0.87 to 1 for more than five decades in good agreement with the Hooge formula, indicating that the flicker noise is associated to mobility fluctuations. The slope lower than the ideal value of 1 is attributed to mobility dependence on the applied voltage. The value of the Hooge constant for the nanofiber devices extracted by the measurements using equation 6.8 is $\alpha_H = 1.5 \pm 1.27$. It is comparable to values found in other nanoelectronic systems such as single-layer MoS2 [22] or single carbon nanotube [23]

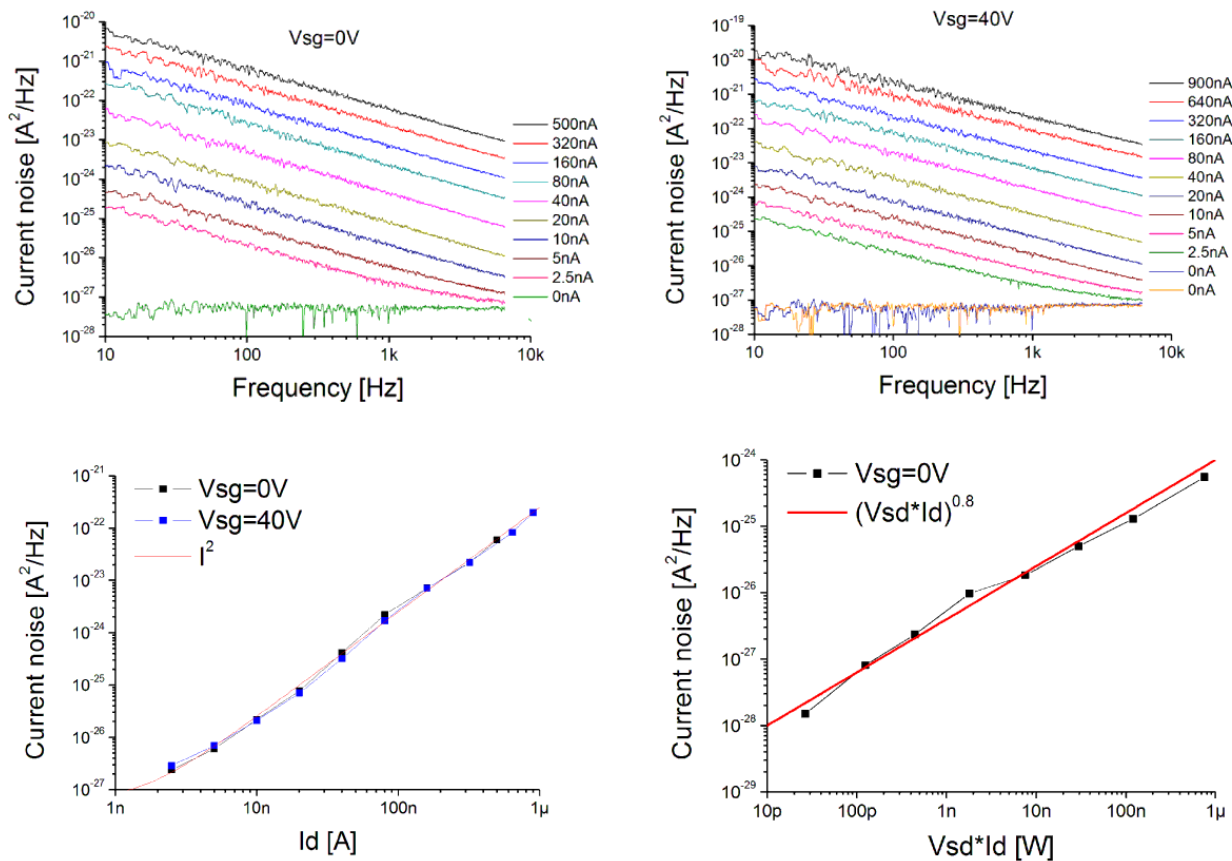


Figure 6.24: Noise measure of thin-film Ofet: graph in the lower right corner is the normalized noise level at 1kHz.

transistors. With the same method the value of the Hooge constant for thin-film P3HT Ofet is $\alpha_H = 70 \pm 65$. The differences between nanofibers and thin-film devices are largely due to the different mobility, as indicated in section 6.1: higher and stable for nanofibers, lower and variable for thin-film devices. Figure 6.26 is a summary of the calculated Hooge constant, for fibers and film devices: a difference between nanofibers and thin-film device is evident, even considering all possible uncertainties in the mobility and noise measures.

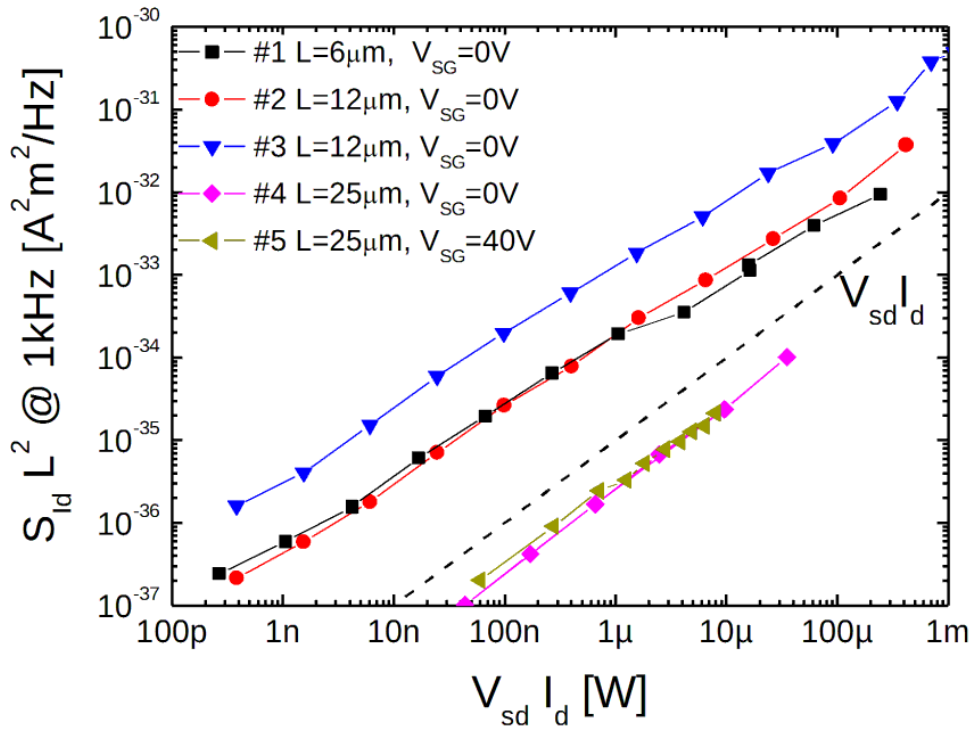


Figure 6.25: Normalized noise level at 1kHz for a set of nanofibers Ofet devices with different channel lengths. The dashed line indicates the slope of $V_{sd} \cdot I_d$ predicted by the Hooge formula

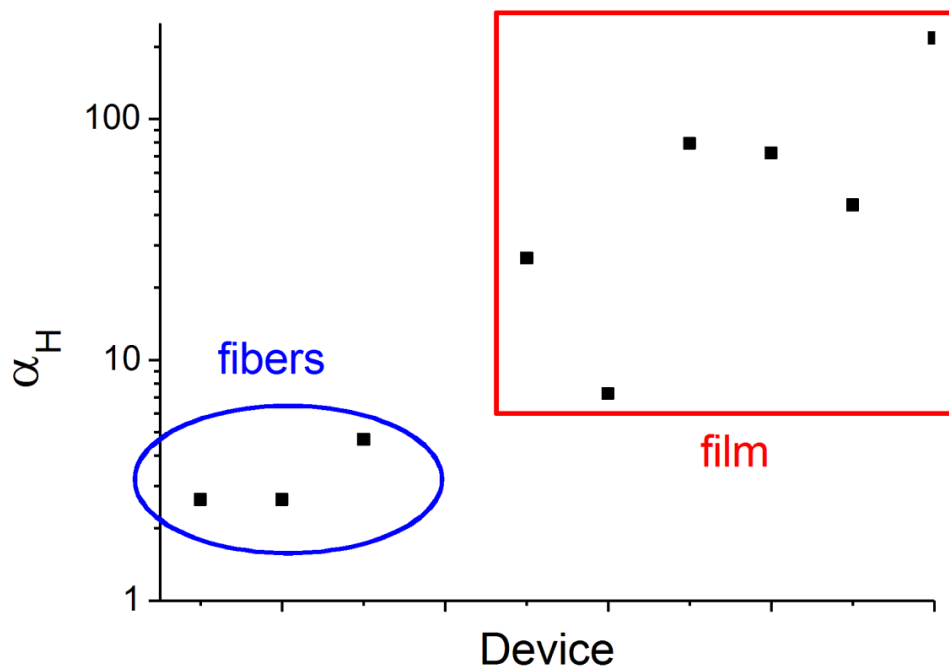


Figure 6.26: Calculated Hooge constant α_H for Ofet devices based on nanometric fibers and thin-film active layer

Conclusioni

L'analizzatore di spettro a cross-correlazione realizzato durante questo lavoro di tesi si è rivelato idoneo alla misura di dispositivi con caratteristiche molto differenti tra loro: la modularità del sistema ha permesso infatti di adattarsi alle differenti esigenze tramite il solo interscambio degli stadi di ingresso specifici per ogni tipo di dispositivo. L'elevata versatilità dell'hardware e del software di controllo ha migliorato e semplificato la realizzazione delle misure rispetto alle vecchie versioni dello strumento. Le misure effettuate sui dispositivi Ofet e MTJ hanno fornito utili indicazioni per meglio interpretarne la fisica e permettere ai rispettivi gruppi di ricerca di migliorarne le caratteristiche.

I risultati ottenuti permettono già di identificare gli aspetti migliorabili su cui concentrarsi negli sviluppi futuri: questi risiedono soprattutto nel continuo lavoro di sviluppo del programma di controllo sia dal punto di vista dell'interfaccia grafica che della flessibilità d'uso generale; in particolare si è sentita la mancanza della possibilità di effettuare un set di misure in maniera completamente automatizzata con il solo intervento iniziale di set-up da parte dell'utente.

Conclusions

The cross-correlation spectrum analyser realized during this thesis work has proven able to measure the noise of different devices with different characteristics: the modularity design of the instrument has allowed to adapt to different needs by changing only the front-end board, specific for each device type. The high versatility of hardware and software has improved and simplified the measures compared to older versions of the instrument. The noise measures taken on Ofet and MTJ devices have provided useful information to better understand their physics and have allowed the respective research groups to improve their characteristics.

The obtained results allow to identify improvable aspects to focus on in future developments: especially a lot of work can be done on the control software to improve its user interface and features; in particular it was felt the lack of an automatic mode, capable to perform a set of measures at different bias points in a completely automated manner, with user intervention only at the initial set-up.

Bibliography

- [1] G. Ferrari, *Analizzatore di spettro digitale a cross-correlazione*, Tesi di Laurea, A.A. 1997-1998, Politecnico di Milano
- [2] S. Pozzi, *Analizzatore di spettro a cross-correlazione per misure a larga banda del rumore di corrente*, Tesi di Laurea, A.A. 2006-2007, Politecnico di Milano
- [3] National Instruments, *Ni 5122 100MS/s 14-bit digitizer*
- [4] M. Carminati, A. Calderoni, *Progetto, realizzazione e caratterizzazione sperimentale di un preamplificatore a larga banda per misure di rumore ad alta sensibilità*, Tesi di Laurea, A.A. 2002-2003, Politecnico di Milano
- [5] L. Fasoli, M. Sampietro, G. Ferrari, *Spectrum analyzer with noise reduction by cross-correlation technique on two channels*, Review Of Scientific Instruments 70 (1999), no. 5, 2520-2525.
- [6] M. Sampietro, G. Ferrari, *Correlation spectrum analyzer for direct measurement of device current noise*, Review Of Scientific Instruments 73 (2002) no.7, 2717-2723.
- [7] P. Manicardi, *Realizzazione di un analizzatore di spettro a cross-correlazione per misure a larga bande del rumore di corrente*, Tesi di Laurea, A.A. 2008-2009, Politecnico di Milano
- [8] A. Oppenheim, R. Schafer, J. Buck, *Discrete-Time Signal Processing*, Prentice-Hall International, 1999.
- [9] A. Block, *Murphy's Law and Other Reasons Why Things Go Wrong*, Paperback, 1978.
- [10] Data Transmission Lines and Their Characteristics, *National Semiconductor Application Note 806 Kenneth M. True*, April 1992
- [11] E. Albisetti, *Spintronic transducers based on magnetic tunnel junctions for biomolecular recognition*, Tesi di Laurea, A.A. 2009-2010, Politecnico di Milano
- [12] P. Jonkers, *Quantum transport in disordered magnetoresistive systems*, 2010, Rijksuniversiteit Groningen
- [13] Z. Q. Lei, G. J. Li, W. F. Egelhoff, P. T. Lai, P. W. T. Pong, *Review of Noise Sources in Magnetic Tunnel Junction Sensors* IEEE TRANSACTIONS ON MAGNETICS, VOL. 47, NO. 3, MARCH 2011

- [14] G. Lecoy and L. Gousskov, *Noise in thin films metal-oxide-metal Al – Al₂O₃ – Al* Phys. Status Solidi B, vol. 30, pp. 917, 1968
- [15] G. Gervasoni, *Progetto e realizzazione di uno strumento a doppio lock-in per la rivelazione in tempo reale di beads magnetiche*, Tesi di Laurea, A.A. 2012-2013, Politecnico di Milano
- [16] G.Ferrari, M. Sampietro, *Wide bandwidth transimpedance amplifier for extremely high sensitivity continuous measurements*, Review of scientific instruments 78, 094703, 2007
- [17] G.Ferrari, F. Gozzini, A. Molari, M. Sampietro, *Transimpedance Amplifier for High Sensitivity Current Measurements on Nanodevices*, IEEE Journal of solid-state circuits, Vol. 44, No. 5, May 2009
- [18] C. Ciofi, F. Crupi, C. Pace, G. Scandurra, M. Patanè *A New Circuit Topology for the Realization of Very Low-Noise Wide-Bandwidth Transimpedance Amplifier*, IEEE TRANSACTIONS ON INSTRUMENTATION AND MEASUREMENT, VOL. 56, NO. 5, OCTOBER 2007
- [19] Saeed V. Vaseghi, *Advanced Digital Signal Processing and Noise Reduction* Wiley, 2000
- [20] Roy M. Howard, *Principles of Random Signal Analysis and Low Noise Design* Wiley & IEEE PRESS , 2002
- [21] T. H. Wilmshurst, *Signal Recovery From Noise in Electronic Instrumentation* Adam Hilger, 1990
- [22] Sangwan, V. K.; Arnold, H. N.; Jariwala, D.; Marks, T. J.; Lauhon, L. J.; Hersam, M. C., *Low-Frequency Electronic Noise in Single-Layer MoS₂ Transistors* Nano Lett. 2013, 13, 4351-4355
- [23] Back, J. H.; Kim, S.; Mohammadi, S.; Shim, M., *Low-Frequency Noise in Ambipolar Carbon Nanotube Transistors* Nano Lett.2008, 8, 1090-1094.

Ringraziamenti

Ringrazio innanzitutto il professor Marco Sampietro per avermi dato la possibilità di svolgere la tesi nel suo laboratorio consentendomi di far parte del suo gruppo di lavoro. Un grazie particolare a Giorgio Ferrari che mi ha seguito costantemente durante tutto lo svolgimento della tesi.